Interferometry for the space mission LISA Pathfinder

Johanna Bogenstahl, Diplom Physikerin

Department of Physics and Astronomy,
University of Glasgow

Presented as a thesis for the degree of Ph.D.
in the University of Glasgow, University Avenue,
Glasgow G12 8QQ

February 26, 2010

Contents

List of Figures

List of Tables

Acknowledgements

"I know I played every note" (Itzhak Perlman)

This thesis is the product of around four years of work during which I have been accompanied and supported by many people. It is now my great pleasure to take the opportunity to thank them.

In particular, I wish to express my gratitude to my supervisors, Henry Ward and Sheila Rowan for giving me the opportunity to work in this group and for their important advice, helpful suggestions, and constant encouragement. I would also like to thank Jim Hough for offering me the opportunity to come to Scotland - I enjoyed it so much.

I am grateful to David Robertson for supervising my project. His excellent guidance, valuable suggestions and enthusiasm always helped me to stay on track throughout this research project. Furthermore I would like to thank the great LISA group: It was a pleasure to spend my time with you guys and not only as office mates also as friends: Christian Killow, Ewan Fitzsimons, Michael Perreur-Lloyd, Russell Jones, and Harry and Dave. Special thanks go to Alastair Grant, his never-ending support with grammar and spelling was a great help and led to many interesting conversations about Scotland's history.

This research was supported and funded by STFC (formerly PPARC). As the recipient of a SUPA (Scotish Universities Physics Alliance) Prize scholarship I had the opportunity to stay in close contact with my former institute, the Albert-Einstein Institut (AEI) Hannover. I would like to thank the following for their collaboration and support: Karsten Danzmann, Gerhald Heinzel, Antonio Garcia Marin, Felipe Guzman Cervantes, Frank Steier, Gudrun Wanner and Philipp Schauzu. I am very grateful of the support from Stefan Günster, Laser Zentrum Hannover, during my time working on the spectrophotometer. To Yufei Song from the Department of Chemistry go my thanks for supervising and assisting during fibre stripping experiments using hot sulphuric acid. Special thanks go to all the staff in the Department of Physics for providing ideas, comments, solutions and practical help. In particular I would like to thank Stevie Craig and Colin Craig from the workshop and Neil Robertson from the electronic workshop.

I am very grateful to my friends for their support and for making these years so enjoyable. Particular thanks go to Anne, Bryan, Chris, Dima, Frank, Gail, Geppo, Imke, Jochen, Judith, Kathrin, Marielle, Marco, Mark, Morag, Siong, Uta, and so many others.

A special thought is devoted to my family and Dan for their never-ending support, endless patience and encouragement when it was most required.

"Are we human because we gaze at the stars, or do we gaze at them because we are human?"

Stardust (2007 film) based on Neil Gaiman's novel.

Acronyms

Acronym	Definition
AEI	Albert Einstein Institute, Hannover
AOM	Acousto-Optic Modulator
AR	Anti Reflection (coating)
BS	Beamsplitter
CAD	Computer Aided Design
CMM	Coordinate Measurement Machine
CQP	Calibrated Quadrant Photodiode pair
DC	Direct Current component
DRS	Disturbance Reduction System
DUT	Device Under Test
EM	Engineering Model
EOL	End Of Life
ESA	European Space Agency
FIOS	Fibre Injector Optical Subassembly
FMA	Fibre Mounting Assembly
FS	Flight Spare
GRT	General Relativity Theory
HR	High Reflecting (coating)

Acronym	Definition
IGR	Institute for Gravitational Research
ITO	Indium Tin oxide (coating)
LCA	LTP Core Assembly
LIGO	Laser Interferometer Gravitational Wave Observatory
LISA	Laser Interferometer Space Antenna
LPF	LISA Pathfinder
LTP	LISA Technology Package
LZH	Laser Zentrum Hannover
Nd:YAG	Neodymium-doped Yttrium Aluminium Garnet
OB	Optical Bench
OBI	Optical Bench Interferometry
OBF	Optical Bench Frame
OMS	Optical Metrology Subsystem
PBS	Polarising Beamsplitter Cube
PD	Photodiode
PEEK	PolyarylEtherEtherKetone
PFM	Proto-Flight Model
PPARC	Particle Physics and Astronomy Research Council
QM	Qualification Model
QPD	Quadrant Photodiode
OPT	Optical Performance Tests
R	Reflection
STFC	Science and Technology Facilities Council
SUPA	Scotish Universities Physics Alliance
T	Transmission
TM	Test Mass
WIN	Window

Preface

This thesis is an account of work carried out between August 2005 and September 2009 towards the space mission LISA Pathfinder and in particular for the optical bench construction for the LISA Technology Package (LTP).

Chapter 1 gives a brief overview summarised from literature of the nature of gravitational waves and of present and future detectors, as well as of LISA and LISA Pathfinder and the associated work presented in this thesis.

Chapter 2 and chapter 3 describe the characterisation of optical components. The components were irradiated at ESA/ESTEC under the supervision of Z. Sodnik. The tests were carried out by the author supervised and approved by the Glasgow LISA team. The spectrophotometer measurements were carried out by the author at the Laser Zentrum, Hannover with assistance from S. Günster.

Chapter 4 presents the optical bench design of LISA Technology Package. The original optical bench layout model was designed by the LISA team of the Albert Einstein Institute. The design was finalised in 2006 by the Hannover LISA team and the Glasgow LISA team. The author used the final design to further develop lens design throughout the fibre injector (FIOS) design his-

tory. The high precision alignment tools were designed and constructed by the Glasgow LISA team.

Chapter 5 and chapter 6 report on the LTP fibre injectors. The fibre injector was designed by the entire Glasgow LISA team and constructed by C. J. Killow. The author was responsible for metrology measurement and investigation of fibre stripping and assisted during construction. The fibre injector placement of the FIOS qualification model was done by the LISA team Glasgow. The vibration and shock tests and thermal vacuum tests were carried out at SELEX-Galileo, Edinburgh, overviewed by M. Perreur-Lloyd and the author. The optical performance tests were carried out by E. Fitzsimons and the author. The FIOS qualification tests were supervised and approved by the Glasgow LISA team.

Chapter 6 presents the optical performance tests performed on the LTP proto – flight and flight – spare fibre injectors by the author.

Chapter 7 gives a summary of the work presented in this thesis and gives an outlook of forthcoming work related to LTP and LISA, which will be performed by the LISA group Glasgow.

Appendix A is a short report of capillary cleaning carried out by the author. The author could not find any documentation on this subject and found it useful to report on this as part of this thesis.

Appendix B describes the theory of silicate bonding. The theory is obtained from literature and from the patent application of silicate bonding. Furthermore the author presents further experiments carried out by the author supervised by S. Rowan.

Summary

In 1916 Albert Einstein published the Theory of General Relativity (GRT). One of its predictions is the existence of gravitational waves, that is accelerated matter could emit energy in the form of gravitational waves, similar to the emission of electromagnetic waves by an accelerated charge. However, compared with electromagnetic waves, where the lowest order is a dipole, in the case of gravitational waves the lowest order is a quadrupole, because mass does not exhibit the positive/negative signs like electric charge. General Relativity Theory says that gravitational waves should propagate with the speed of light [6].

The first indirect proof of the existence of gravitational waves was provided by Russell Hulse and Joseph Taylor [7] [8]. They tracked a double star system over several years and detected a decrease of the revolution time of the Pulsar PSR 1913+16 arround its neighbour star. The energy emission corresponding to this agrees within 0.5 % with the GRT prediction for the energy lost through gravitational waves. For this observation Hulse and Taylor were awarded the Nobel prize for physics in 1993.

A gravitational wave would stretch and compress space perpendicular to its direction of propagation. However, the elongations occurring would be so tiny that a direct measurement has not yet been done. It is conceivable though,

that in the near future it should be possible to measure gravitational waves caused by violent astronomic events such as the explosion of a supernova or the inspiral of a double star system. The advanced detectors on ground and in space will open a new field of astronomy.

Since the early 1960s there are huge efforts dedicated to detecting gravitational waves. There are different experimental setups. On the one hand, there are resonant detectors with a resonance frequency range of a few 100 Hz up to a few kHz, which can be excited by a gravitational wave. However those detectors only cover a small range of frequencies.

On the other hand, there are experiments to measure gravitational waves with laser interferometry between separated masses. In total there are at this time six interferometrical gravitational earth-based detectors [9], working in a world wide collaboration: TAMA300 (Japan) [10], GEO600 (Germany) [11], VIRGO (Italy/France) [12] and LIGO [13], three detectors, (USA). All these detectors are based on Michelson interferometry [14] and are limited in sensitivity below 10 Hz due to the natural seismic and gravity gradient noise.

A new experiment, LISA, a NASA and ESA joint mission, is planned as an interferometric detector in space. **L**aser **I**nterferometer **S**pace **A**ntenna (LISA)

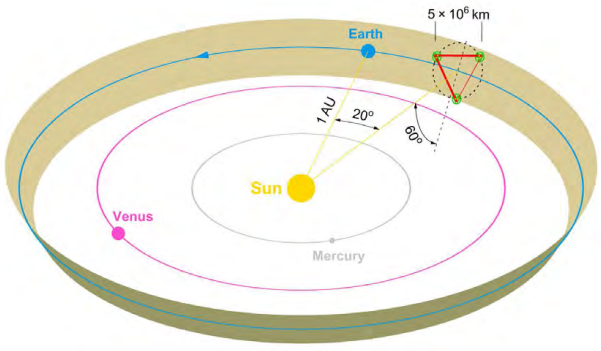

Figure 1: Assembly of LISA satellites in a heliocentric orbit [1].

is an ensemble of three identical satellites moving in a heliocentric orbit. In doing so they would form an equilateral triangle with a five million km side length and with an offset of 20° behind the Earth's orbit. This structure rotates around itself once per year. The triangular plane is tilted by 60^o with respect to the ecliptic. The mission is planned to be launched in 2018.

LISA Pathfinder (LPF) is planned as a test mission of LISA consisting of only one satellite and expected to launch in 2011. The aim of LPF is not to detect gravitational waves, but rather to prove and test key components for LISA. There will be two experiments on board, the American Disturbance Reduction System (DRS) [15] and the European LISA Technology Package (LTP). One of the key tasks of LTP is to measure the relative displacement between two drag-free falling test masses with a noise level of $10\,\mathrm{pm}/\sqrt{\mathrm{Hz}}$ in the frequency range of $3-30$ mHz [16]. Figure 2 shows the engineering model of the optical bench for LTP.

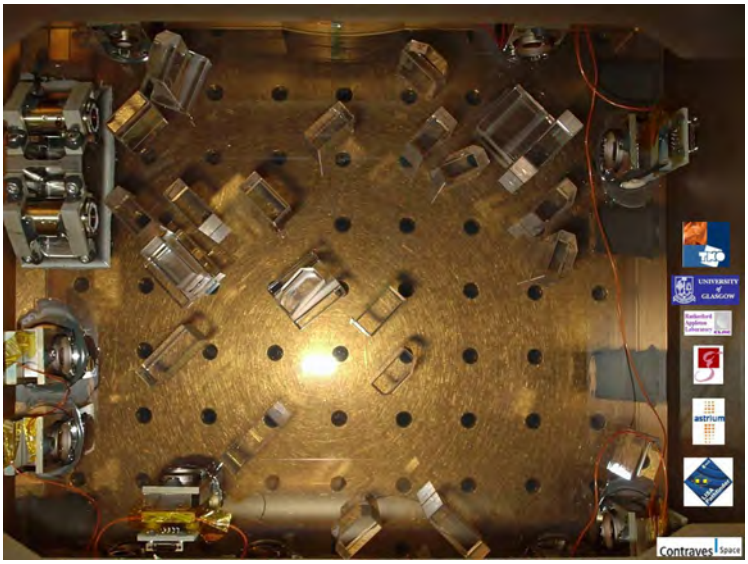

Figure 2: Optical bench of the engineering model of LTP.

Chapter 1

Introduction

1.1 Introduction to gravitational waves

In 1993 The Royal Swedish Academy of Sciences decided to award the Nobel Prize Physics jointly to Russell A. Hulse and Joseph H. Taylor for *the discovery of a new type of pulsar, a discovery that has opened up new possibilities for the study of gravitation* [7] [8]. Hulse und Taylor discovered in 1974 the first binary pulsar, called PSR 1913+16. They made a very important observation when they followed the binary system for some years. It was found that the orbit period is declining, meaning that the two astronomical bodies are rotating faster and faster about each other in an increasingly tight orbit. This effect can be explained as the emission of energy in the form of gravitational waves. The theoretical calculation agrees with the observed value to within about one half of a percent. This can be seen as an indirect proof of the existence of the gravitational waves predicted by Albert Einstein's general theory of relativity.

Albert Einstein presented his general theory of relativity in 1915 [6]. It describes gravity as a property of the geometry of space and time - so called "space-time". The special theory of relativity describes the interval between two neighbouring points in flat space-time as $ds^2 = -c^2\,dt^2 + dx^2 + dy^2 + dz^2 = \eta_{\mu\nu}\,dx^\mu\,dx^\nu$, where $\eta_{\mu\nu}$ is known as the Minkowski metric tensor and c is the speed of light. General Relativity predicts that the space-time is curved by the presence of a mass. This can be described as $ds^2 = g_{\mu\nu}\,dx^\mu\,dx^\nu$ with $g_{\mu\nu} = \eta_{\mu\nu} + h_{\mu\nu}$, where $h_{\mu\nu}$ represents a small perturbation of the metric away from that for flat space-time. Gravitational waves are propagating tiny ripples in the curvature of space-time. The nature of these ripples is a quadrupole wave with two orthogonal polarisations along the direction of propagation. This can be written as the sum of two components: $h = a\,h_+ + b\,h_\times$ where h_+ represents the so-called + polarisation and $h_\times$ the × polarisation. This can be illustrated as a ring of particles which are placed around the display of a clock face. If a gravitational wave would pass through this ring of free-falling particles the ring would transform as shown in figure 1.1.

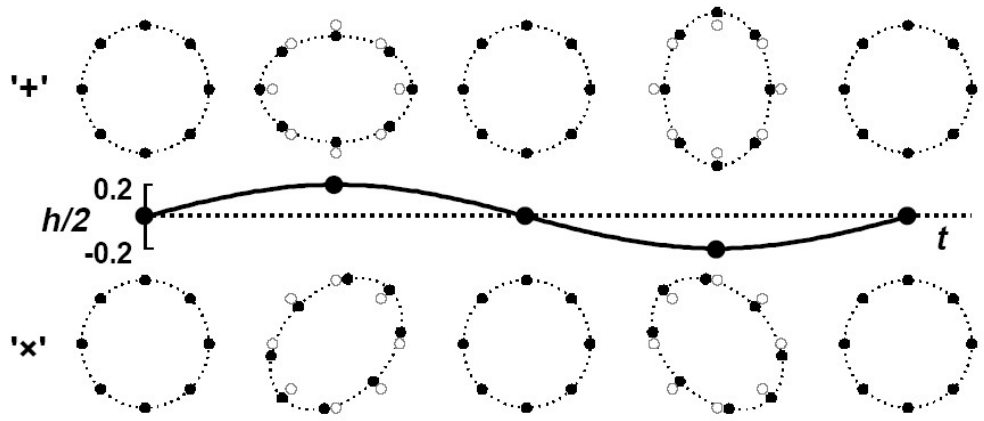

Figure 1.1: Illustration of the polarisation of a gravitational wave [2]. Shown are the distortions in the original circle that the wave produces if it carries the + polarisation (above) and the × polarisation (below).

The maximum change, ΔL, in separation of two oppositely located particles in such a ring with a diameter L is given by: $\Delta L/L = h/2$ where h is the gravitational wave amplitude. The gravitational wave amplitude h is usually described as a physical strain in space. The effect of stretching and squeezing the space-time will be used for the detection of a gravitational wave. Typical amplitudes of expected gravitational waves are in the range of 10^{-18} - 10^{-24}. For two particles separated by 1 km this would result in changes in their separation of $10^{-15} - 10^{-21}$ m. For the ~150 million kilometer distance from the Sun to the Earth the change would be only the diameter of an atom!

Two different approaches to measure gravitational waves are in use. One approach is to detect gravitational waves by using Michelson type interferometers. A laser beam is split into two beams, and each beam travels the same distance but in a different direction to the other (ideally orthogonal to the other). The beam is reflected from a pendulum-suspended mirror back to the beamsplitter, which combines both beams again. The interference of the beams is observed and a gravitational wave which creates a path length difference between the arms would cause a phaseshift of the interference.

The other method is a descendant of the first ever approach to measuring gravitational waves. It is based on bar-detectors, first operated by Joseph Weber in the late 1960s [17]. They consist of an aluminium bar of large mass suspended in a vacuum tank with anti-vibration mounts with piezoelectric transducers bonded around its centre line. These detect the change of the resonance frequency of the bar caused by the change of dimensions due to a gravitational wave. Resonant gravitational wave detectors have evolved from the room temperature bars of J. Weber to the sub-Kelvin bars, further information can be obtained from [18].

Both types of gravitational wave detectors are constantly being improved to reduce their noise and therefore increase the sensitivity of the detector to a gravitational wave signal. Figure 1.2 shows the sensitivity of a few gravitational wave detectors of both types. The sensitivity of the interferometric detectors (illustrated in yellow) and of bar-detector type (illustrated in green) has shown improvements over the years. Intrinsic to the design of bar detectors is their narrow bandwidth. The next generation of bar-detectors will use spherical dual-acoustic masses [19] which will allow a broader frequency detection range.

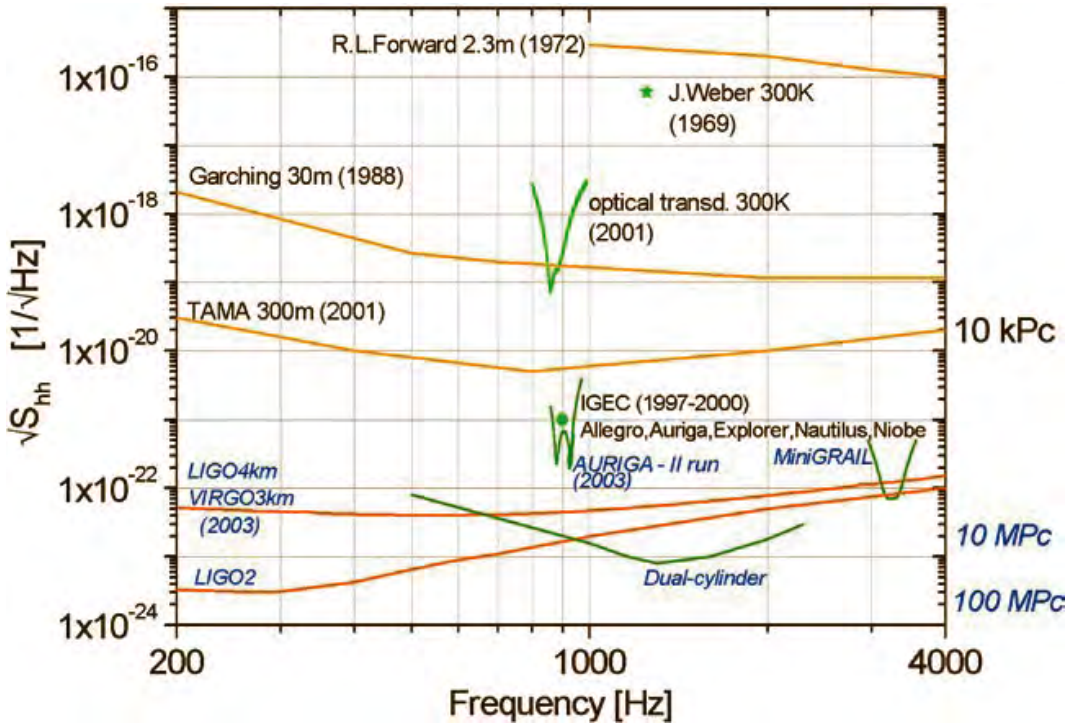

Figure 1.2: Sensitivity curve of different detectors since 1969 until 2003 [3].

The thermal noise limitation of bar detectors is being addressed by operating the detectors in the range from a few kelvin to millikelvin. A report on the latest progress of resonant-mass gravitational wave detectors can be found in [20].

Accelerated masses produce gravitational waves. But the weakness of this signal means that there are limits to the detection of gravitational waves; only gravitational waves created by great cosmological events are likely to be detected. Potential events are expected to be: black hole interactions and coalescences, neutron star coalescences, low-mass X-ray binaries, supernova explosions, rotating asymmetric neutron stars and processes in the early Universe. The expected gravitational wave frequency ranges from 10^{-17} Hz in the case of ripples in the cosmological background to 10^{3} Hz when neutron stars are born in a supernova explosions. All ground-based detectors are limited in the low frequency range of a gravitational wave due to seismic and gravity gradient noise. To measure low frequencies a space-based interferometrical detector is planned called LISA: Laser Interferometer Space Antenna [21].

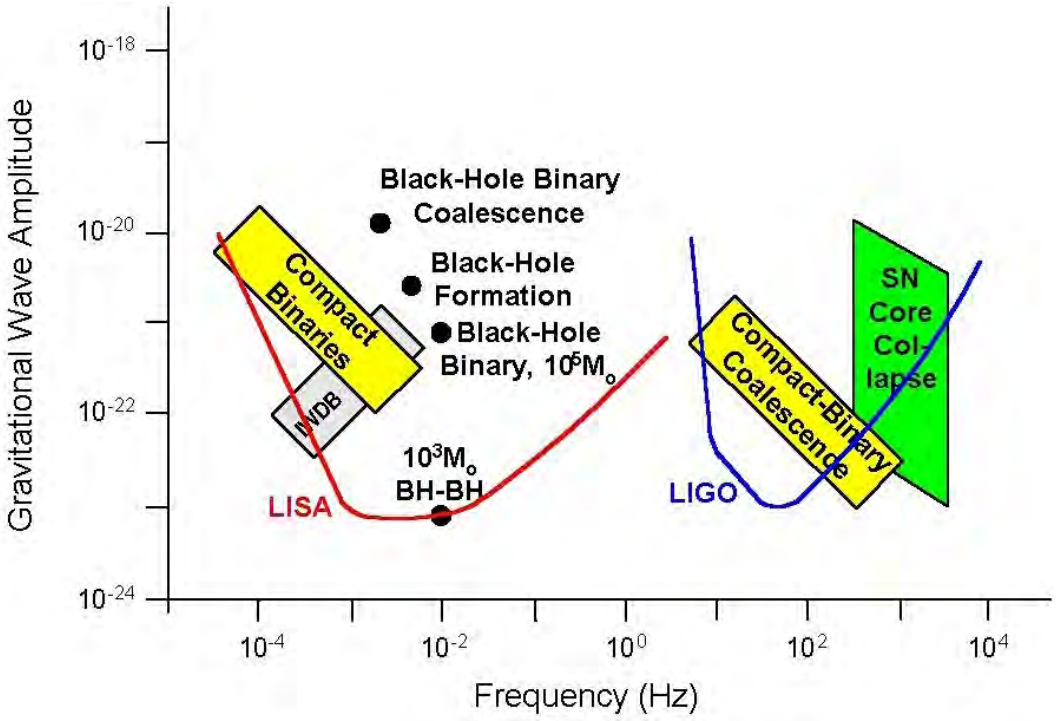

Figure 1.3: Frequency spectrum of gravitational waves.

Six ground based interferometric gravitational wave detectors are in operation: a 300 m detector at Japan (TAMA), three LIGO detectors in USA (one 2 km and two 4 km long armlengths), a 3 km long detector in Italy (VIRGO) and a 1200 m (folded 600 m) long detector (GEO600) in Germany. They form a science community in which a number of detectors at different locations can be synchronised in order to avoid spurious detection and to obtain information about the direction and nature of sources. The last science run "S6" finished in 2009 (without TAMA). Currently the detectors are being upgraded to improve their sensitivity. LIGO gets updated to Advanced LIGO: the basic optical configuration is a power-recycled and signal-recycled Michelson interferometer with Fabry – Perot resonance in the arms [22]. The goal of the GEO – HF program is to improve the sensitivity of the GEO detector in the high-frequency mode by reducing the effect of two limiting noise sources, namely shot noise and coating thermal noise [23]. In 2013 it is expected that all upgraded detectors will be running. LISA will join in 2018 to complement the gravitational wave telescopes in the low frequency range. As well as proving the existence of gravitational waves a new field of astrophysics will be opened up.

1.2 Introduction to LISA

LISA is a joint ESA/NASA mission. LISA will consist of three spacecraft forming an equilateral triangle with five million kilometer side length trailing Earth in its heliocentric orbit by about 20°. The triangular plane revolves over a year, while its normal remains tilted at 30° to the plane of the ecliptic and pointed towards the sun. The nominal LISA mission duration is 6.5 years where 1.5 years is needed for orbit transfer and commissioning. LISA is planned to be launched in 2018, seven years after its precursor mission LISA Pathfinder (LTP).

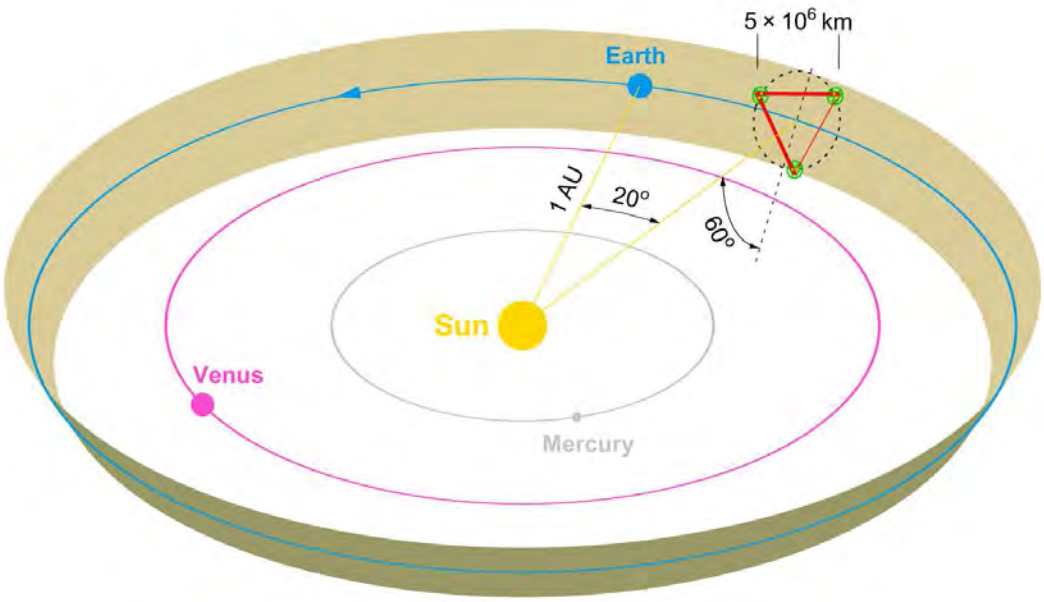

Figure 1.4: Schematic diagram of the orbit of LISA [1].

In LISA laser interferometry will be used to measure the relative displacement of inertial proof masses shielded inside the spacecraft. Each spacecraft houses two optical benches including an inertial proof mass. The proof masses act as mirrors in an interferometric metrology system. This is split in to three parts: each spacecraft is linked to the others with a "long-arm" measuring beam (five million kilometer side length) from one optical bench to the other optical bench inside the spacecrafts and there are two "short-arm" links inside each spacecraft, between the proof mass and the optical bench. The precision of the interferometric metrology system to measure the proof mass relative motion has an accuracy of $10\,\mathrm{pm}/\sqrt{\mathrm{Hz}}$. The specific goal of LISA is that the relative acceleration between two proof masses is less about $3{\times}10^{-15}\mathrm{ms}^{-2}/\sqrt{\mathrm{Hz}}$ in order to measure in the low frequency range of 3×10^{-5} - 10^{-1} Hz.

There are five types of gravitational wave sources that are expected to be detectable with LISA: Inspiralling and merging massive black holes (10^3 to 10^7 solar masses), stellar-mass compact objects spiralling into supermassive black holes in galactic nuclei, close binaries of compact objects, and possibly backgrounds and bursts from cosmological and/or astrophysical sources. The observation of these sources will provide information about galaxies and the sources themselves as well as further information about the Universe and the behaviour of spacetime. New physics can be discovered looking back to the early Universe as well as the physics of dense matter. In the low frequency band the sensitivity limit is expected to be dominated by background noise of binary system of dwarf stars. Above 10 mHz the instrument noise is expected to be the dominating noise source.

1.3 Introduction to LISA Pathfinder

LISA Pathfinder (LPF) is managed by ESA and carries ESA and NASA test packages. The aim of LPF is not to detect gravitational waves, but rather to prove and test key technologies to be used in LISA. LISA uses never-before built technology, much of which can only be properly verified in space. These technologies include a laser metrology system, a drag-free control system for the onboard test masses, an ultra-precise micro-propulsion system and attitude control. LPF consists of one spacecraft which houses two drag-free free-falling test masses. These test masses and the initial sensors are placed inside two vacuum tanks. Between the vacuum tanks, a laser interferometry bench is located which monitors the movement of the test masses with a noise level of $10\,\mathrm{pm}/\sqrt{\mathrm{Hz}}$. The spacecraft itself will be located at the first Sun-Earth Lagrange point "L_1". The position of the test masses with their housing are monitored by capacitive sensors. If the test masses move from their nominated

positions a control loop sends a feedback signal to the micro-propulsion system to correct the position of the spacecraft itself around the free-falling test masses. This technology cannot be proved on the ground. LPF has two payloads on board: The LISA Technology Package (LTP) and The Disturbance Reduction System (DRS) [15] which also includes a set of micro-propulsion systems. The DRS experiment will use the LTP signal of the location of the test masses for its data-analysis and control systems. The specific goal

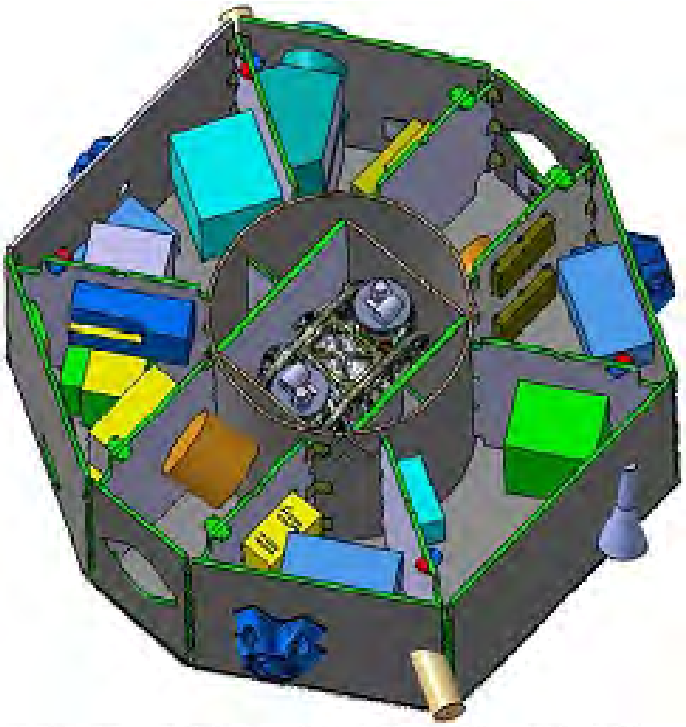

CAD view of LISA Pathfinder satellite with LTP core assembly in the centre. © EADS Astrium

Figure 1.5: CAD rendering of the LPF satellite.

of the LPF mission is to demonstrate that the relative acceleration between two proof masses is less than $3 \times 10^{-14}\,\mathrm{ms}^{-2}/\sqrt{\mathrm{Hz}}$ in the frequency range of 1 - 9 mHz. This a factor of ten higher than the LISA requirements.

1.4 Introduction to the LTP interferometer

The LTP optical bench interferometer (OBI) is being built at the University of Glasgow, Institute of Gravitational Research (IGR). Figure 1.6 shows the OptoCAD [24] simulation. The OBI consists of four heterodyne interferometers, see section 4.4. The movements of the test masses, which are reflective optics of two of the interferometers, can be observed by measuring the heterodyne signals of the interferometers, see chapter 4. For this an ultra-stable optical bench is required [25]. Therefore the optical bench consists of an ultra-low expansion glass-ceramic, Zerodur, with the optical components silicate bonded [26] to it. As part of the LTP OBI, two customised ultra-stable fibre injectors (section 5.1) are attached to the bench by monolithic joints. These fibre injectors have been developed, qualified, and built at IGR, see chapter 5 and 6. The fibre injector consists of glass components which are either glued or silicate bonded together and an optical fibre including strain relief cladding. The design and building process of the fibre injector are subject to "space qualification", see section 5.3.

1.5 Introduction of optical components for LTP interferometry

The optical components of the optical bench are mirrors and beamsplitters, these components are made of fused silica with optical coatings applied to their surfaces. The optical coatings were subjected to irradiation testing, see chapter 2 and 3. The lenses of the fibre injectors could not be made of fused silica, so that lens material was tested separately, see chapter 2.
Optical windows are located in the wall of the vacuum tanks, which house the test masses. The beam passes through those on its way from the optical bench

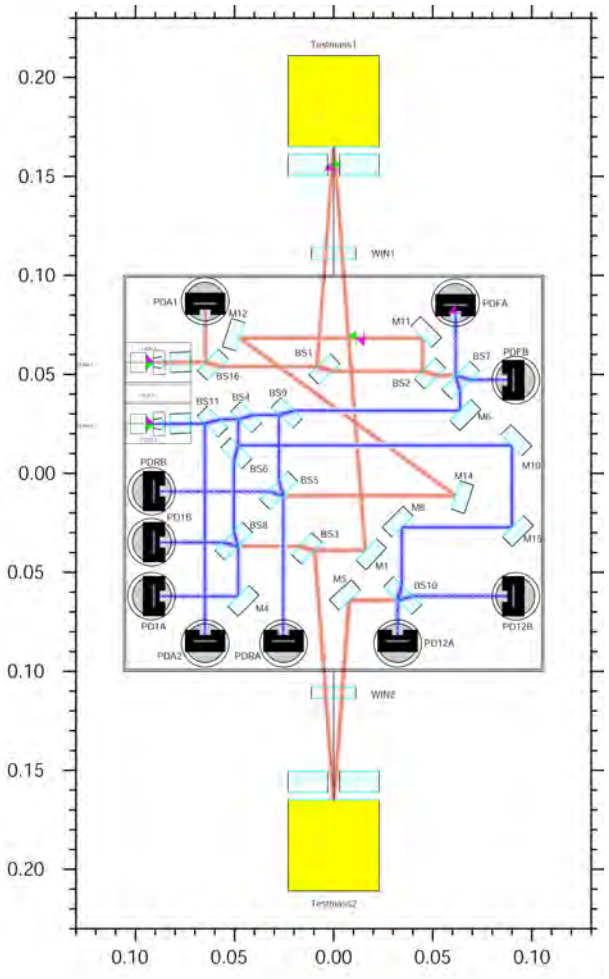

Figure 1.6: OptoCAD simulation of the optical bench interferometer of LTP. The axes are labelled in meters.

to the test masses and again after reflection. The optical windows were also investigated in terms of irradiation damage, see section 2.4.

1.6 Introduction to the optical prototype bench

The aim of building an LTP OBI optical prototype bench is primarily to use it as a reference bench for the fibre injector space qualification process (section 5.3). The fibre injectors are built to the same design and placed at the same

location onto a representative optical bench of the same dimensions as for the LTP OBI bench. Afterwards the prototype bench can be used further to build up an exact optical copy of the flight model, including the same design of fibre injectors and therefore will have similar optical performance. Thus the optical prototype bench will be the replacement of the engineering model [27] and will allow ground-based readout experiments. It can also be used as a dummy bench for flight model OBI performance procedure set-ups. Furthermore the construction of the optical prototype bench provides practice for the assembly stages of the flight model (section 5.2) and will provide feedback to prove the optical bench alignment tools (section 4.5) and each construction step.

Chapter 2

Characterisation of radiation hardness of optical components

This chapter describes the experimental procedure and results of testing the optical performance of various components before and after irradiation. These tests are required due to the radiation environment in space. The cosmic rays and Van Allen belts are carrying energetic charged particles, all of these forms of radiation can cause damage to optical components [28]. Radiation causes the formation of colour centers in optical materials as well as changes in refractive index and mechanical properties [29]. Therefore the following optical flight model components considered here are: mirror, beamsplitter, polarising beamsplitter (PBS) and lens. The end of life (EOL) specification of the optical components and their coating is that their optical properties resists radiation doses up to 20 krad. Furthermore the components, with the exception of PBS, were tested up to 100 krad with other space missions like LISA in mind. The requirement is led by the orbit, by the life-time of the mission in space and the construction of the spacecraft; due to the location of the LTP OBI in the spacecraft shielding reduces the exposure to electrons and low energy pro-

tons. The components have been irradiated using a ^{60}Co γ-source at ESTEC (Netherlands). This is a standard procedure for irradiation tests of inner core parts/devices of a space load. For tests the coatings for mirror and beamsplitter are applied on one inch fused silica discs. The optical components were measured before and after irradiation. For measuring the reflectivity of mirrors and beamsplitters a Nd:YAG laser at 1064 nm was used as well as for the transmission of a lens and the deviation of a 50 % beamsplitter. Furthermore a spectrophotometer based at the Laser Zentrum Hannover (LZH), Germany, was used for measuring a wavelength spectrum of the transmission for mirror, beamsplitter, PBS, lens, and windows.

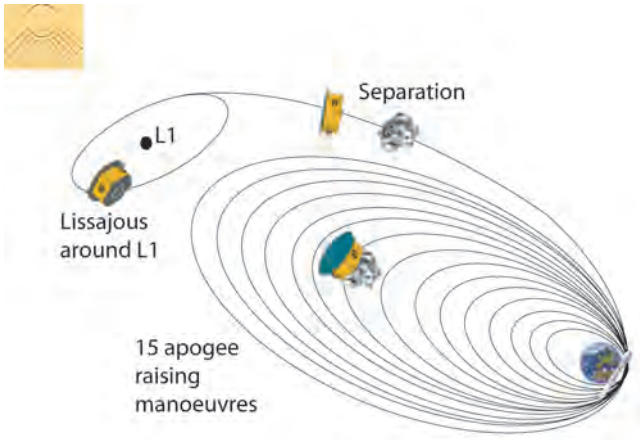

Figure 2.1: Drawing of LTP orbiting around the earth until reaching L1.

The EOL specifications are taken from the OBI Requirements Specification (S2-UGL-RS-3001 OBI Requirements Specification) [30].

coating	EOL specification
mirror HR	R $\geqq$ 99 %
beamsplitter HR	R = 50 $\pm$ 2 %
beamsplitter AR	R $\leqq$ 1 %

Table 2.1: Specifications for mirror and beamsplitter for the OBI.

2.1 Characterisation of mirror and beamsplitter in reflection using a Nd:YAG laser

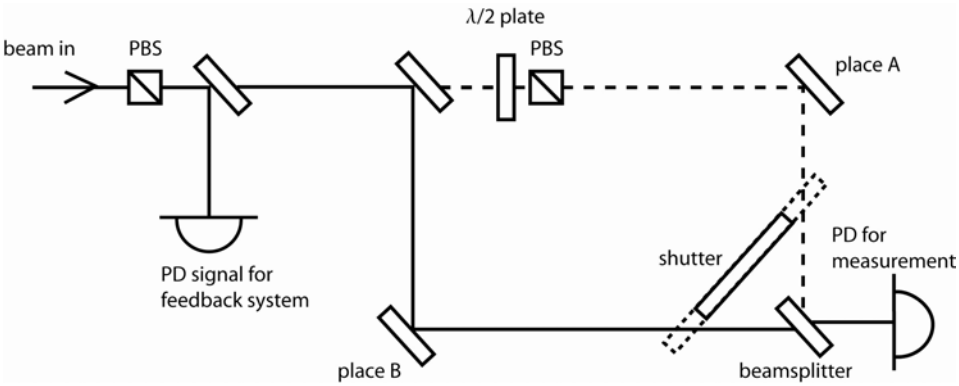

Figure 2.2: Schematic layout of experimental set-up.

Figure 2.2 shows the schematic layout of the experiment to measure the optical characteristics of mirrors and beamsplitters in reflection. The laser light passes through a polarising beamsplitter (PBS) to provide s-polarisation. 10 % of the laser beam is split off and measured by a photodiode (PD). The signal from this photodiode drives a feedback system to stabilise the power of the laser. The laser beam was stabilised within 0.5 % while the measurement was taking place. Then the laser beam is split into two arms; these are indicated with a solid line and a dashed line. The power in the dashed path can be adjusted by rotating a $\lambda/2$ plate such that the following s-polarised aligned PBS rejects light. In this manner the power of the arms can be equalised. A beamsplitter assures that both beams are hitting the photodiode at the same spot for measuring the power of the beams. The beams are aligned to superpose on an IR card. Using a shutter it is possible to swap quickly between the beams, so that both beams can be measured independently but nearly simultaneously. The dashed-line beam is the so-called test beam or test path, the other beam is the reference beam or reference path. All optics are

aligned for s-polarisation, maintained by the polarising beamsplitters. Two commercial mirrors and beamsplitters are used as reference mirrors and beamsplitters for setting up the experiment. Non-irradiated and irradiated mirrors and beamsplitters were measured in this way by measuring the reflection of the component at position A (U_{TP1}) and having a reference component at position B (U_{RP1}). The measurement was repeated by swapping the positions of the components (U_{TP2} and U_{RP2}). Comparison of these measurements provides the reflectivity of the component under test compared to the reference sample. By swapping the components back to their original position the variation of the laser power over the total time can be found.

The measurement of the reflection of the AR coated side of the beamsplitter uses the same set up as the mirror/beamsplitter reflection measurement. The laser and feedback system set up is the same too. But instead of swapping the position of the device under test, the side of the beamsplitter is turned over from the 50 % reflecting surface to the AR coating.

2.1.1 Analysis of measurements

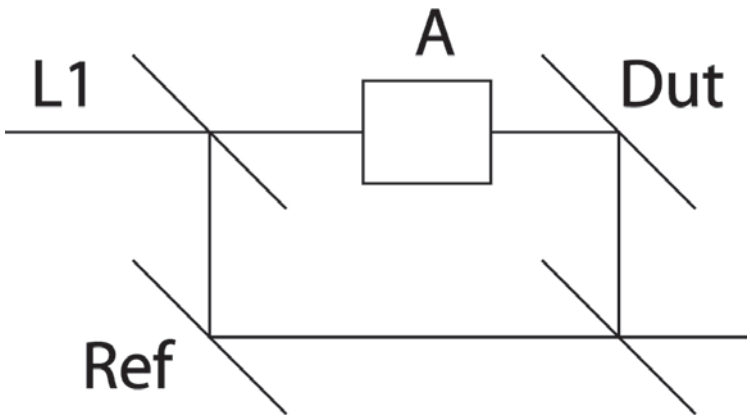

Figure 2.3: Schematic diagram of the experiment for analysis.

It is assumed that the total power of the laser is constant during the period of a measurement pair (i.e. two measurements separated only by the repositioning of the shutter between the two arms), but that the laser power may vary between other pairs of measurements. This possible variation in laser power is taken into account in the following analysis. Attenuator A includes half wave plate and PBS unit.

U_{RP1}	Measurement of the reference path with reference device in mount
U_{RP}	Measurement of the reference path with DUT in mount
U_{TP1}	Measurement of the test path with DUT in mount
U_{TP2}	Measurement of the test path with reference device in mount
A	Attenuator
L	Input Laser beam of measurement
M	Measurement number
D_{ut}/R_{ef}	Ratio of beam reflection of DUT compare to reference sample

Table 2.2: Explanation of acronyms used in text 2.1 and analysis.

Measurement 1: DUT (device under test) is in test path, the reference sample is in reference path

$$U_{\mathrm{RP1}} \triangleq L_1 R_{\mathrm{ef}} \tag{2.1a}$$

$$U_{\mathrm{TP1}} \triangleq L_1 A D_{\mathrm{ut}} \tag{2.1b}$$

$$\Rightarrow M_1 = U_{\mathrm{RP1}}/U_{\mathrm{TP1}} = R_{\mathrm{ef}}/AD_{\mathrm{ut}} \tag{2.1c}$$

Measurement 2: DUT is in reference path, the reference sample is in test path

$$U_{\mathrm{RP2}} \triangleq L_2 D_{\mathrm{ut}} \tag{2.2a}$$

$$U_{\mathrm{TP2}} \triangleq L_2 A R_{\mathrm{ef}} \tag{2.2b}$$

$$\Rightarrow M_2 = U_{\mathrm{RP2}}/U_{\mathrm{TP2}} = D_{\mathrm{ut}}/AR_{\mathrm{ef}} \tag{2.2c}$$

From this it follows that:

$$\text{From 2.1} \Rightarrow AM_1 = R_{\text{ef}}/D_{\text{ut}} \tag{2.3a}$$

$$\text{From 2.2} \Rightarrow AM_2 = D_{\text{ut}}/R_{\text{ef}} \tag{2.3b}$$

$$\Rightarrow A = R_{\text{ef}}/D_{\text{ut}}M_1 \tag{2.3c}$$

$$\Rightarrow D_{\text{ut}}/R_{\text{ef}} = M_2R_{\text{ef}}/(D_{\text{ut}}M_1) \tag{2.3d}$$

$$\Leftrightarrow M_2/M_1 = (D_{\text{ut}}/R_{\text{ef}})^2 \tag{2.3e}$$

Therefore the equation for the analysis of the total reflection can be found as:

$$D_{\text{ut}}/R_{\text{ef}} = \sqrt{((U_{\text{RP2}}U_{\text{TP1}})/(U_{\text{TP2}}U_{\text{RP1}}))} \tag{2.4}$$

In the case of the measurement of the AR coated side, the measurement is compared to the reference path. The reflectivity, R_{efl}, is the following:

$$R_{\text{efl}} = ((U_{\text{TP2}}U_{\text{RP1}})/(U_{\text{RP2}}U_{\text{TP1}})) \tag{2.5}$$

2.1.2 Characterisation of PBS in transmission

The experimental set up is the same as before. The PBS under test is housed in a suitable mount in the test path as shown in Figure 2.4. The beams of both arms are balanced and measured (U_{test} and U_{refl}). The PBS is placed in the mount in such a way that s-polarised light passes through and p-polarised light is reflected upwards. This is the measurement of the first maximum of the PBS ($U_{1\text{max}}$ and U_{refM1}) . To measure the second maximum transmission the PBS is rotated by 180° degrees ($U_{2\text{max}}$ and U_{refM2}). The analysis of the measurement for a PBS in transmission is similar to the mirror and beamsplitter analysis.

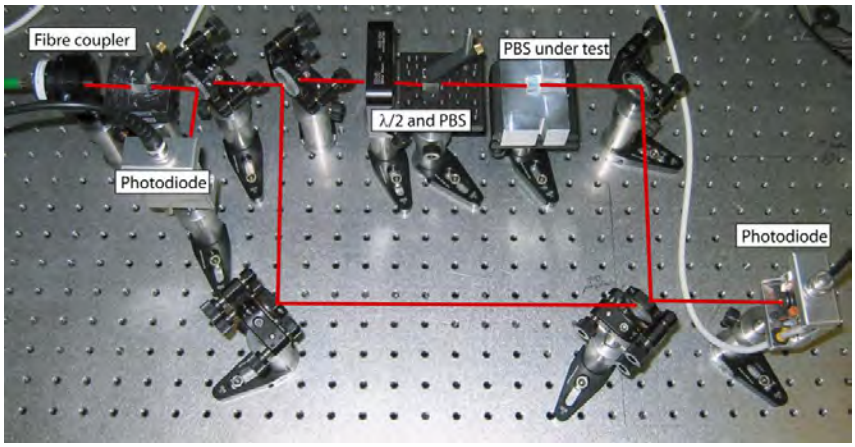

Figure 2.4: Picture of experimental set up for measuring the transmission of polarising beamsplitters.

2.1.3 Characterisation of lens in transmission

In total 30 lenses were obtained from the company Thorlabs with a butch certification for the test campaign and fibre injector construction. The material of the lens is ECO - 550. The measurement of a lens is done in a different set up from that for the mirror and beamsplitter. It is shown in Figure 2.5.

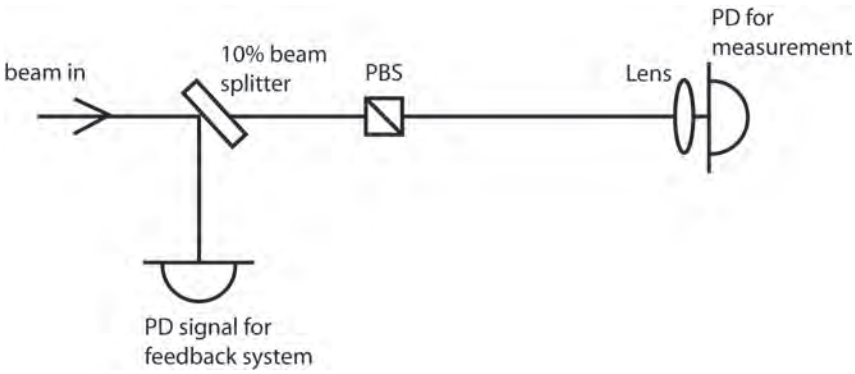

Figure 2.5: Experiment schematic diagram for measuring the transmission of a lens.

As previously, 10 % of the laser beam is split off and measured by a photodiode

(PD in Figure 2.5). The signal from this photodiode drives the laser feedback system to stabilise the power of the laser. The transmitted light passes through a polarising beamsplitter before it goes through the lens onto a photodiode for taking the measurement. The lens under test will be placed inside the lens mount, which is specially designed for this lens and provides for each lens a reproducible position. The photodiode is placed as close as possible to the lens ($\sim 12\,\mathrm{mm}$). The beam was measured with (beam diameter $\sim 1\,\mathrm{mm}$) and without (beam diameter $\sim 2\,\mathrm{mm}$) a lens in the beam path. The analysis of irradiated lenses was made by comparing the measurement with non-radiated lenses in the same measurement run. When the lens is in position, the spot size and position is different than with the lens absent. Hence the ratio of transmission ($U_w/U_{w/o}$) is not unity. Therefore the irradiated lenses have to be comparing with non-irradiated lenses of the same batch in the same measurement run.

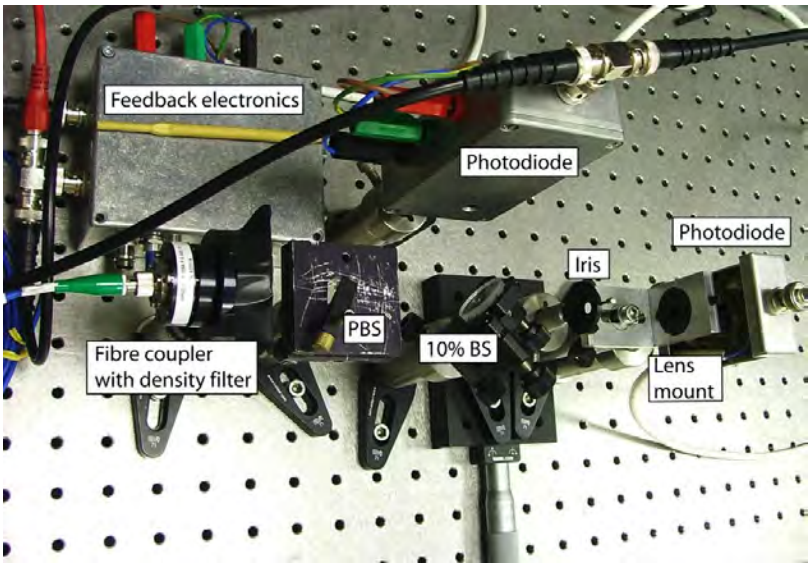

Figure 2.6: Picture of the experimental set up.

Five lenses of the same batch were compared to each other, three of them have been irradiated with 20 krad the other ones not irradiated. The experiment was repeated including two lenses of the same kind, but not of the same batch, which have been irradiated with 100 krad.

2.1.4 Results of measurements

coating or material	0 krad	20 krad	100 krad
mirror HR	$99.78 \pm 0.24\,\%$	$99.87 \pm 0.44\,\%$	$101.08 \pm 0.44\,\%$
beamsplitter HR	$50.57 \pm 0.49\,\%$	$50.28 \pm 0.35\,\%$	$50.05 \pm 0.35\,\%$
beamsplitter AR	$0.62 \pm 0.01\,\%$	$0.60 \pm 0.01\,\%$	$0.61 \pm 0.01\,\%$
PBS transmission	1.Max: 100 % 2.Max: 100 %	1.Max: $99.8 \pm 0.1\,\%$ 2.Max: $99.6 \pm 0.1\,\%$	— —
lens transmission	100 % (normalised)	$100.44 \pm 1.0\,\%$	—
lens transmission repeated measurement	100 % (normalised)	$99.76 \pm 0.47\,\%$	$100.13 \pm 0.18\,\%$

Table 2.3: Measurement results.

The conclusions of the measurements are summarised in Table 2.3. The reflectivity of irradiated mirrors and beamsplitters has been compared to earlier measurements of the same samples before irradiation. The error is the standard deviation of the measurement stability during the measurement. In the case of the AR measurements of the beamsplitter, and the measurements of the transmission of the lens and PBS, the irradiated samples were compared to other non-irradiated samples from the same batch. In the case of the AR coating the error of the measurement is the standard deviation of a repeated measurement of a non-irradiated sample six times. In the case of the transmission of the lens and the PBS, the measurement has been normalised in comparison to the non-irradiated sample. The PBS cube was measured twice by turning it around of 180° (both maxima throughput for s-polarised light).

In conclusion it can be said that no significant difference can be detected between irradiated and non-irradiated components and that all are within the requirements for LISA Pathfinder using a 1064 nm light source. Furthermore

they would be suitable for missions where a higher radiation dose up to 100 krad is expected. Due to a larger beam diameter on the optical bench interferometer of LISA in comparison to LISA Pathfinder interferometer it is not to be expected that the same lens will be used, but the material ECO - 550 is a commonly used material for moulded lenses and therefore the experiment shows that this material is also suitable for other space applications with expected irradiation doses of up to 100 krad.

2.1.5 Beamsplitter characteristic depending on polarisation

The aim of these experiments was to see how the behaviour of the beamsplitter changed with changing polarisation of the input light. Figure 2.7 shows the experimental set up. The beamsplitter under test (DUT) is placed in a mount in such a way that it splits the beam with an angle of incidence of 45°. By rotating the $\lambda/2$ plate the polarisation can be controlled. The transmitted and reflected beams are measured simultaneously with photodiodes. Due to the use of two different photodiodes, which have slightly different gains, the measurements of the photodiodes are not providing equally scaled readouts. Nevertheless the shape of the curves of non-irradiated and irradiated beamsplitters can be compared with each other using the same set-up for all PBSs under test.

To compare the curves more easily, the difference in gain of both photodiodes was characterised. The PD01 for reflection was taken as the reference photodiode, its gain was set to 1. The gain of PD02 for the transmission is compared to the other PD01 and is 1.093. This means that the gain of the PD02 is ~10 % higher than the gain of PD01. The factor of 1.093 was calculated by taking the ratio of reflection and transmission by BS05 at s-polarisation. To

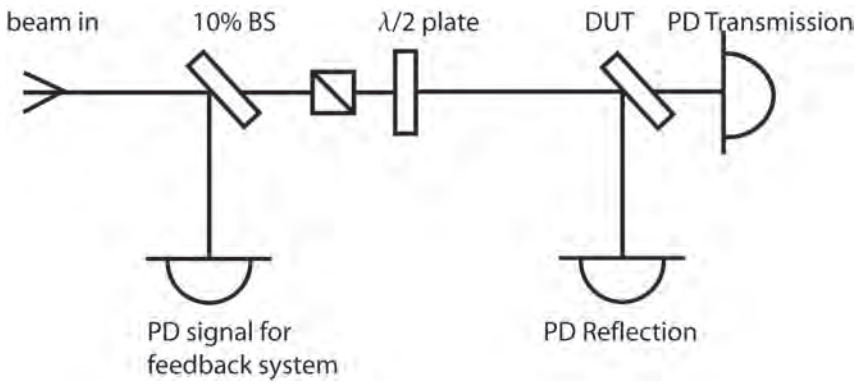

Figure 2.7: Schematic diagram of set up.

compare the curves with each other, the measured transmission value was multiplied by the ratio factor of 1.093. The curves are shown in figure 2.8. The continuous curves show the transmission percent and the dotted curves show the reflection percent of the beamsplitters. Two non-irradiated beamsplitters were measured. Their curves are indicated with crosses as well as two curves of 100 krad irradiated beamsplitters, which are indicated with stars. The shapes of the curves of non-irradiated and irradiated beamsplitters are similar. Due to using two different photodiodes and assuming a ratio factor to compare them, the percentage magnitudes of transmission and reflection cannot be taken to account. It can only be said that there is no trend showing a difference between non-irradiated and irradiated beamsplitters

The measurements were repeated using the same photodiode for measuring the transmission and reflection. This was done by aligning the photodiode at the same point in the paths using reference points, so that the risk of not hitting the photodiode sensor always at the same spot is minimised. The measurement errors are within an absolute number of 0.5 % for the curves for transmission and reflection. Taking the laser fluctuation into account, a total absolute error 1 % is obtained. Figure 2.9 shows the transmission and reflection curve of a non-irradiated beamsplitter.

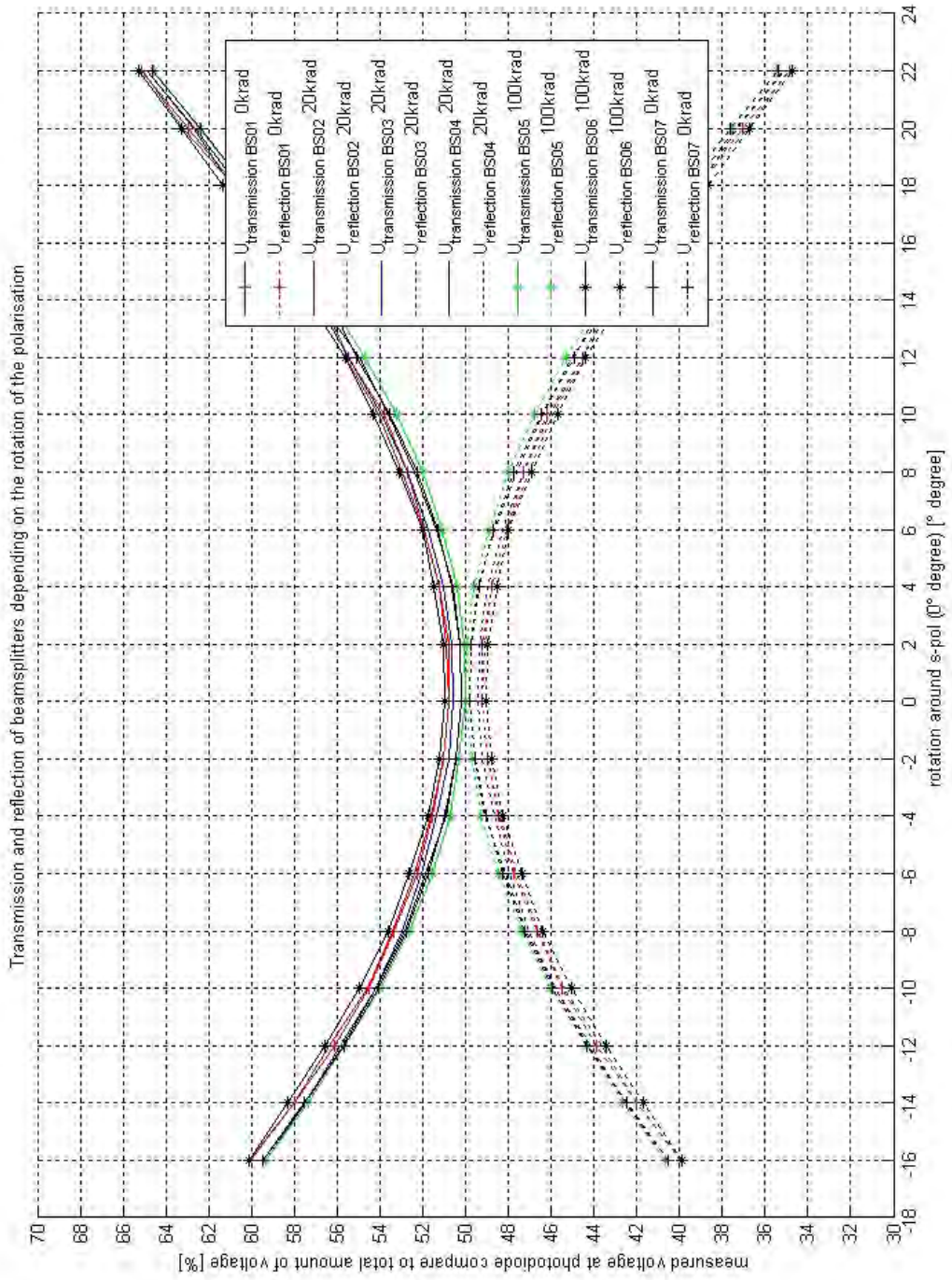

Figure 2.8: Deviation of the input beam at a beamsplitter depending on polarisation and irradiation.

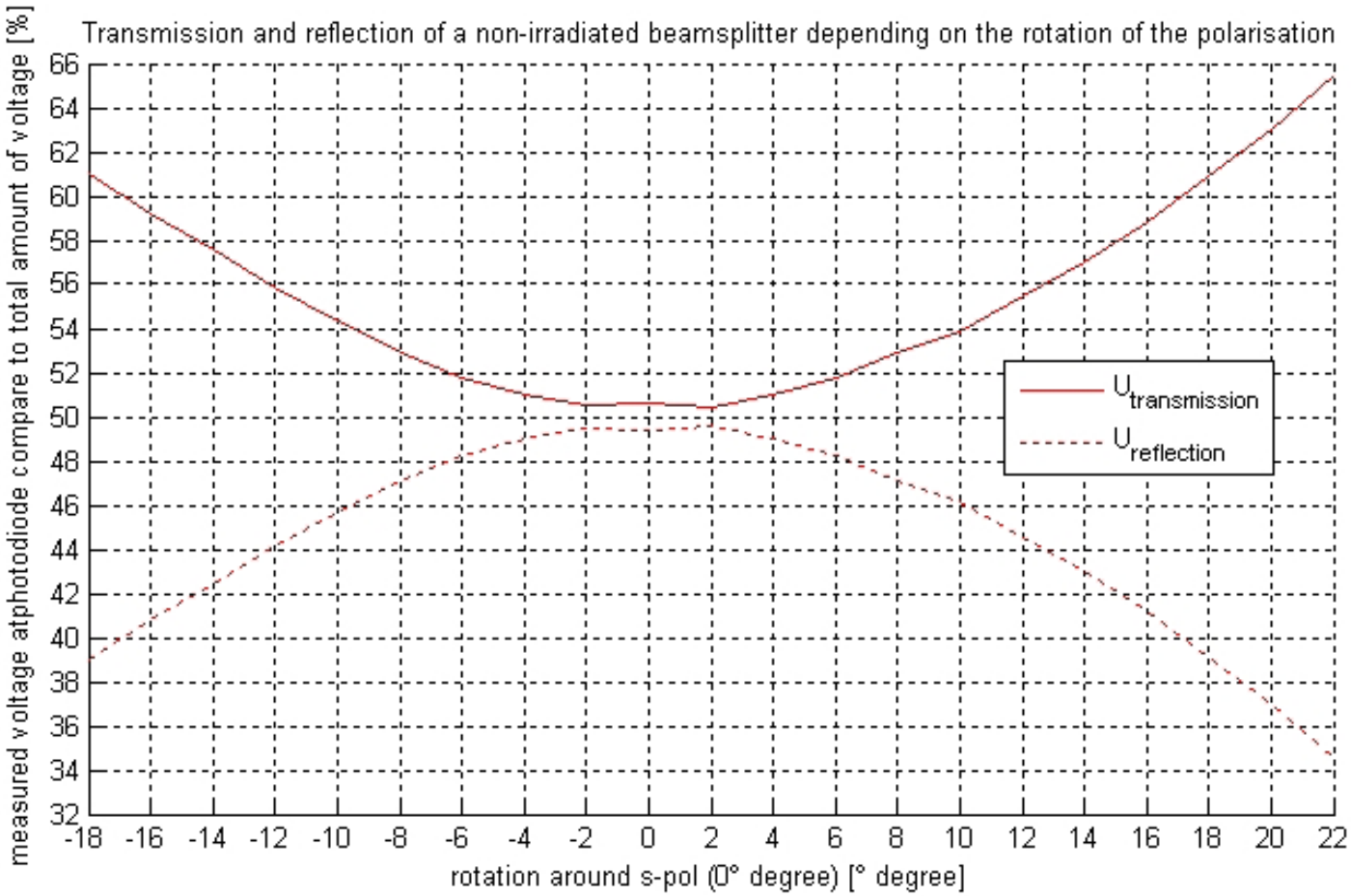

Figure 2.9: Measurement of the deviation of a non-irradiated 50 % beamsplitter depending on the polarisation using one photodiode for measurement.

2.2 Characterisation of flight model optical coated components in transmission using a spectrophotometer

The basic set up for measuring with a spectrophotometer uses unknown polarised light and measures the transmission at zero incidence. As a result it becomes necessary to fit these measurements to a simulated curve for s-polarisation and a 45° angle of incidence as in our case. To fit a curve it is important to have further information about the coating material and the number of layers. This proprietary information was not given in detail by the coating company. Therefore our optical components were directly measured under 45° incidence in a mount. The components are all specified for s-polarised light. However the spectrophotometer uses unpolarised light, therefore the performance of the components, particularly the beamsplitters, is different than it would be for their designed polarisation. Despite these limitations, a valid comparison of non-irradiated and irradiated samples can be made. The repeatability of the spectrophotometer was measured using the same sample with the same set-up six times. The standard deviation of these measurements is shown in figure 2.10; the blue curve showes the standard deviation for mirror measurements and the red curve for beamsplitter measurements. In the case of a beamsplitter the standard deviation is 0.2 % in the range from 180 - 850 nm and in the range of 851 - 2000 nm 0.1 %. This guarantees a satisfactory repeatability of the measurements. A peak at 850 nm is seen in the measurement, this is due to an instrument artifact. The curve for a mirror shows peaks. These occur where the transmission curve has a steep gradient, therefore small wavelength changes in the spectrophotometer cause large standard deviation values of up to 4.5 %. Measurements with 45° angle of incidence

show that these significant jumps are at different wavelengths in comparison to zero incidence. The standard deviation around 1064 nm is ~ 0.014 %. The components have been tested by the author using a Perkin Elmer lambda 900 spectrophotometer at the Laser Zentrum hannover (LZH).

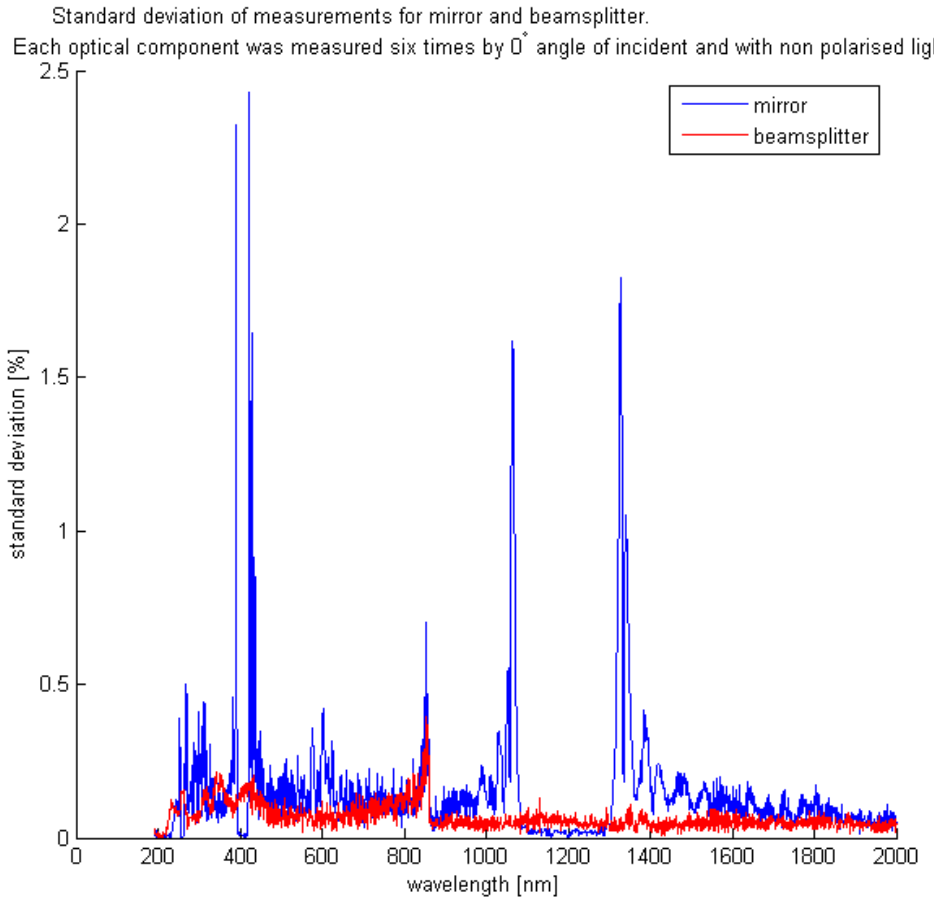

Figure 2.10: Standard deviation of a spectrophotometer measuring a flight model coated mirror (blue curve) and a beamsplitter (red curve).

2.2.1 Measurement of 45° degree angled components

Figure 2.11 shows the set up for the mirror, beamsplitter and AR coated side of beamsplitter measurements. The sample is clamped into a mount, which can

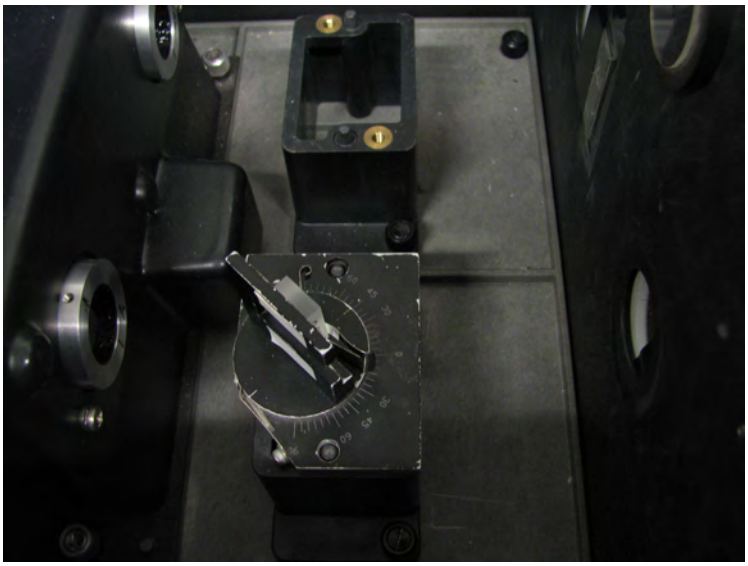

Figure 2.11: Mount for measurements with 45° degree angle of incidence.

be adjusted to 45° angle of incidence. Using the same mount and orientation for all measurements, a comparison between these measurements can be made. Figures 2.12, 2.13 and 2.14 show the wavelength spectrum of the transmission through a mirror, beamsplitter and the AR coated beamsplitter which is under investigation. The following three pages show the graphs of the spectrums: The first graph is the wavelength spectrum over the whole wavelength range of 300 - 2000 nm, the second graph is a zoom in around 1064 nm, which is the wavelength on which the LISA Pathfinder interferometer is running. In the case of the beamsplitters a transmission of 50 % was not observed, this is due to the wrong polarisation of the measurement beam.

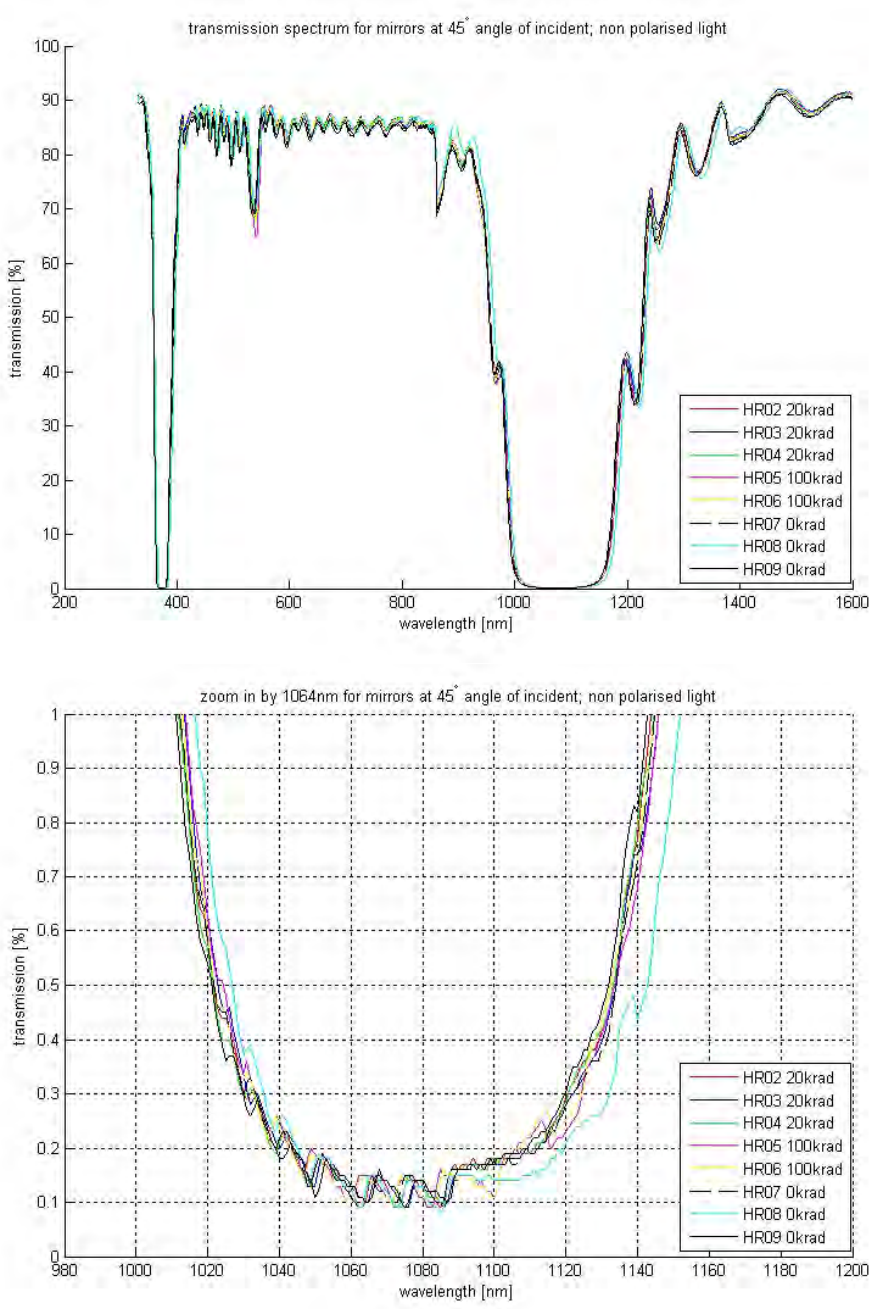

Figure 2.12: Wavelength spectrum and zoom for 1064 nm for irradiated and non-irradiated mirrors.

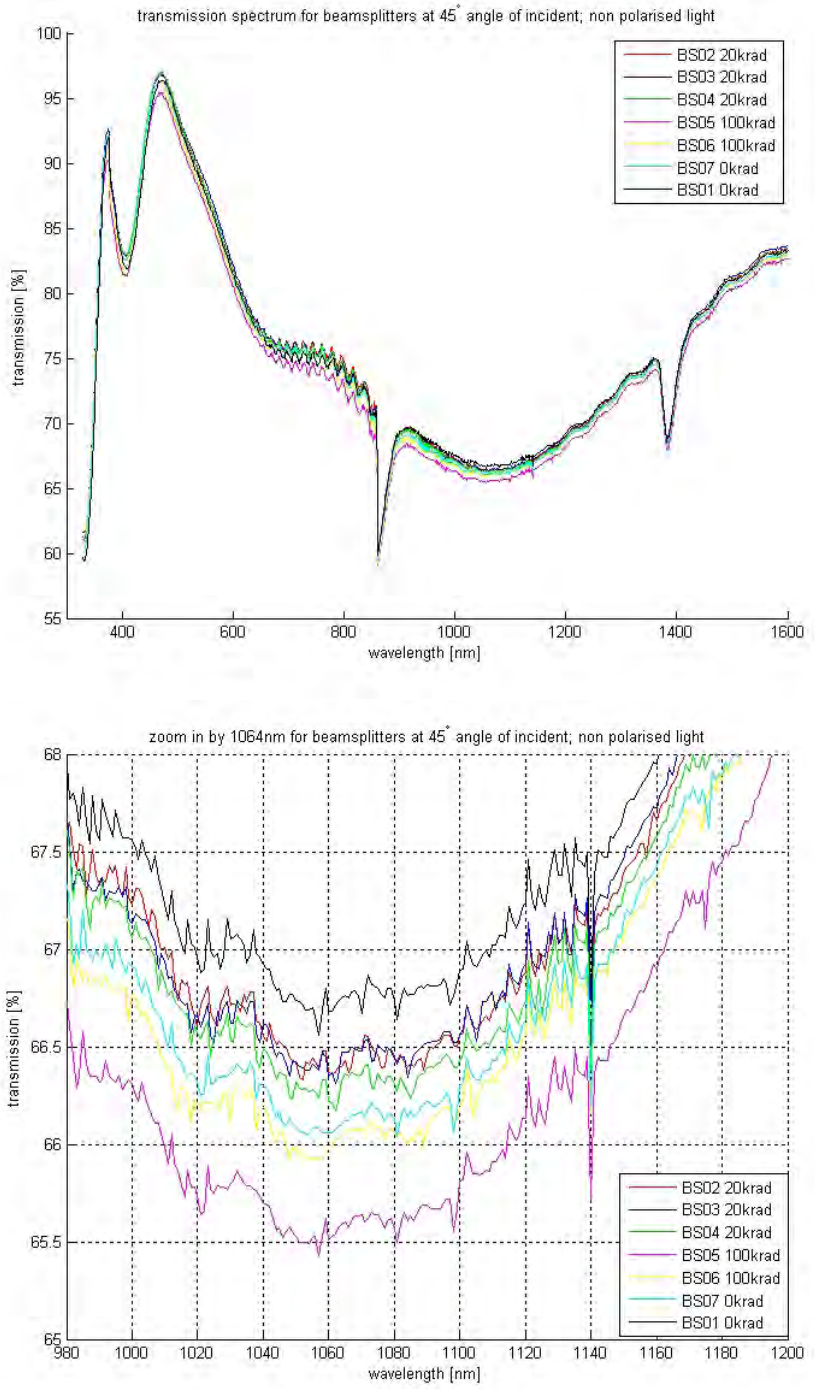

Figure 2.13: Wavelength spectrum and zoom for 1064 nm for irradiated and non-irradiated beamsplitter.

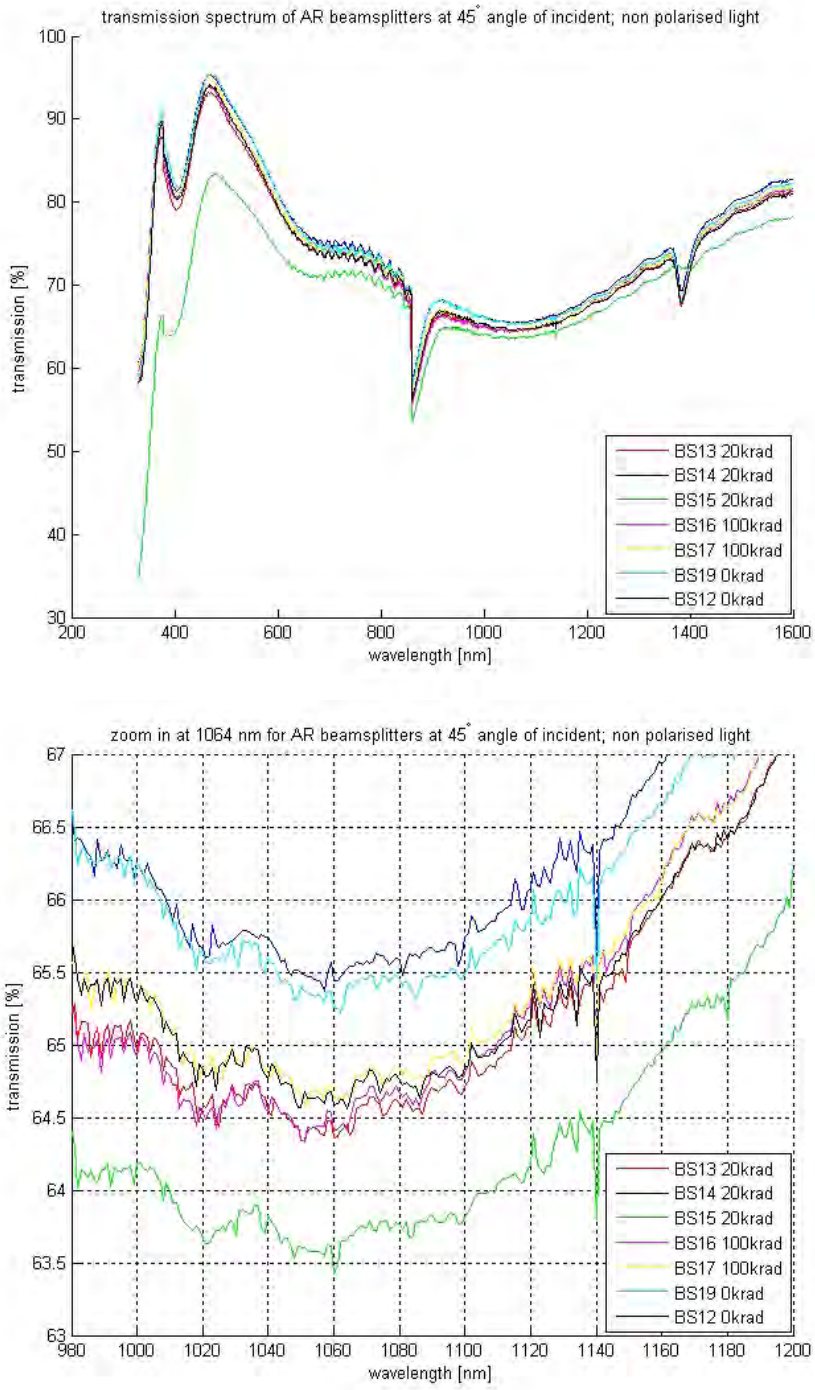

Figure 2.14: Wavelength spectrum and zoom for 1064 nm for irradiated and non-irradiated AR coating of beamsplitter.

In figure 2.12 it can be seen that there is nearly no transmission in the wavelength range from 1040 - 1120 nm. Fused silica does not absorb the light and there is nearly no absorption of the light inside the coating, therefore it can be assumed that ~ 99.9 % of the light is getting reflected. This confirms previous Nd:YAG measurements.

In figure 2.13 the three curves of the beamsplitters which have been irradiated with 20 krad (red, dark blue and green) are very close to each other. Both curves of non-irradiated beamsplitter (light blue and black) and irradiated with 100 krad beamsplitter (violet and yellow) show greater differences (< 1 %). But in general it can be said that the average over the samples does not show any change due to irradiation.

In figure 2.14 it is easy to see that the curve of BS15 (green curve) is different from the other curves. This is due to the fact that the coating was not applied onto a fused silica substrate, instead it was applied onto BK7, a well-known non irradiation-hard material, particularly in the visible light spectrum. This can also be identified by the change of the colour of the material. The disc changes colour from transparent clear to yellowish after irradiation with 20 krad. The shapes of all the graphs are similar to the BS spectrum (figure 2.13).

2.2.2 Measurement of 0° degree angled components

Figure 2.15 shows the mount which is used to measure PBSs. It is the same mount as previously used during the Nd:YAG laser measurements. A PBS was aligned to the top and right edge having a corner of the PBS cube in the notch. Each of the four orientations of the PBS was measured three times and an average was taken of these. Two PBSs were irradiated with 20 krad.

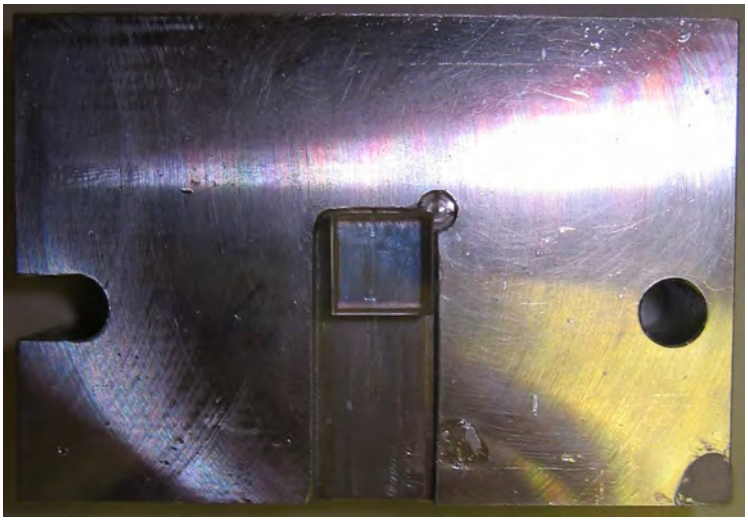

Figure 2.15: PBS mount used in spectrophotometer.

These two were measured by comparison with one non-irradiated PBS. Each PBS was measured in the same four orientations; these are indicated with different colours in figure 2.16. Each colour is split into three measurements for each PBS, a solid curve for PBS01, a dash-dotted curve for PBS02 and a dotted curve for PBS04. The difference of the PBSs is between 2.18 % (PBS01 and PBS2, back reflection) and 0.41 % (PBS02 and PBS04, front reflection). This difference is likely to be caused mainly by difficulties in accurately and repeatably positioning the PBS in the mount and due to the slight difference in the shape of each PBS as discovered, see section 5.1.3.

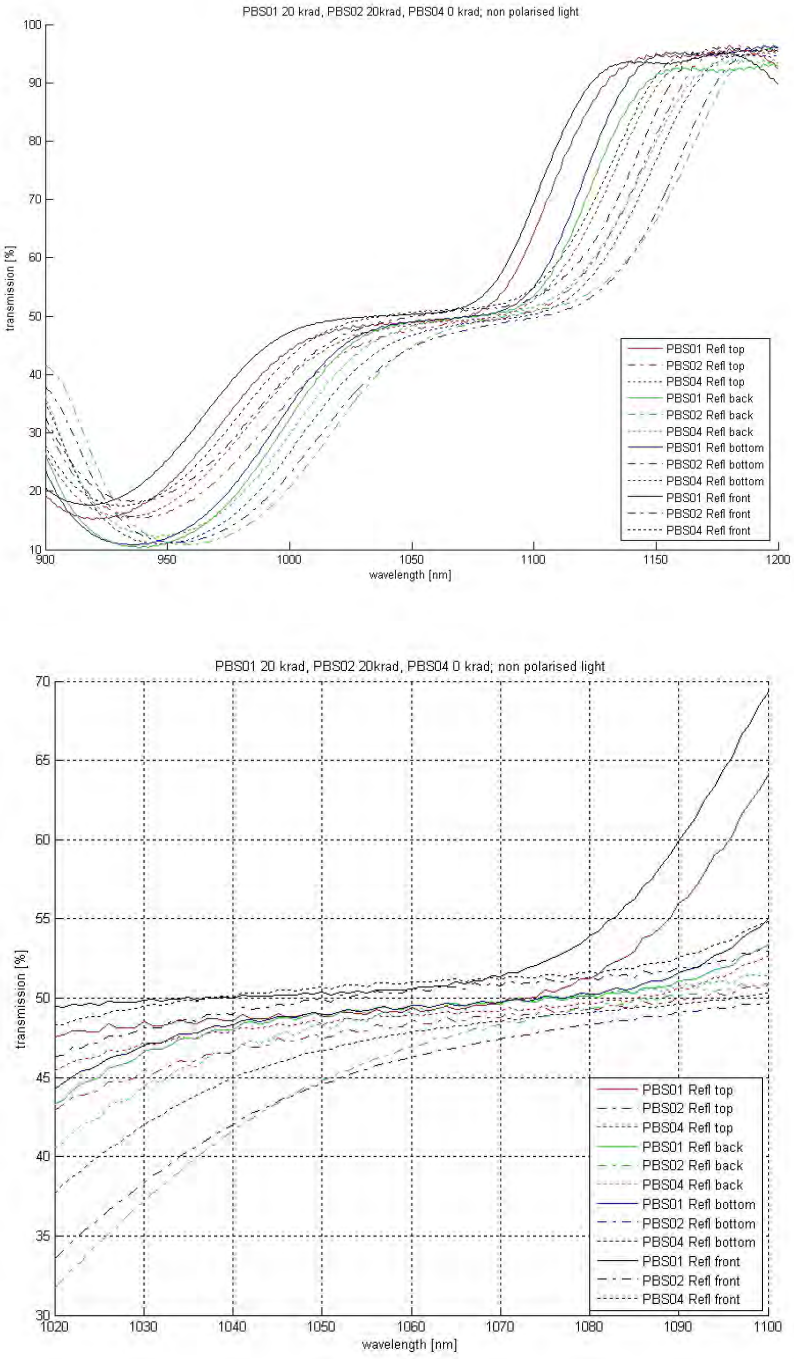

Figure 2.16: Wavelength spectrum and zoom for 1064 nm for irradiated and non-irradiated polarising beamsplitter.

In the case of measuring the transmission of a lens, a different customised mount was developed and is shown in figure 2.17. Due to the focussing effect of a lens a second lens is used to re-collimate the beam. The lenses are of the same kind. The first lens is a non-irradiated lens and stays the same for all measurements; the second lens is the one under test. The mount is adjustable and the lenses are aligned with a distance of $\sim 12\,\mathrm{mm}$ to each other, producing a high transmission of around $70\,\%$ through the lens system of two non-irradiated lenses. The mount can be secured and reproducible measurements are possible afterwards. Thus it is possible to compare irradiated and non-irradiated lenses with each other using a spectrophotometer. Each lens was measured three times, so that an average could be taken for these three measurement and the standard deviation was taken as the uncertainty of the results.

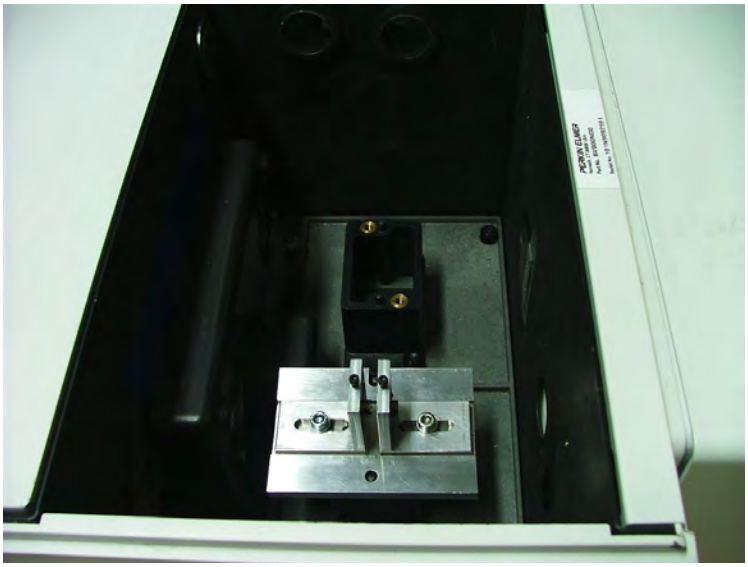

Figure 2.17: Lens mount system inside the spectrophotometer.

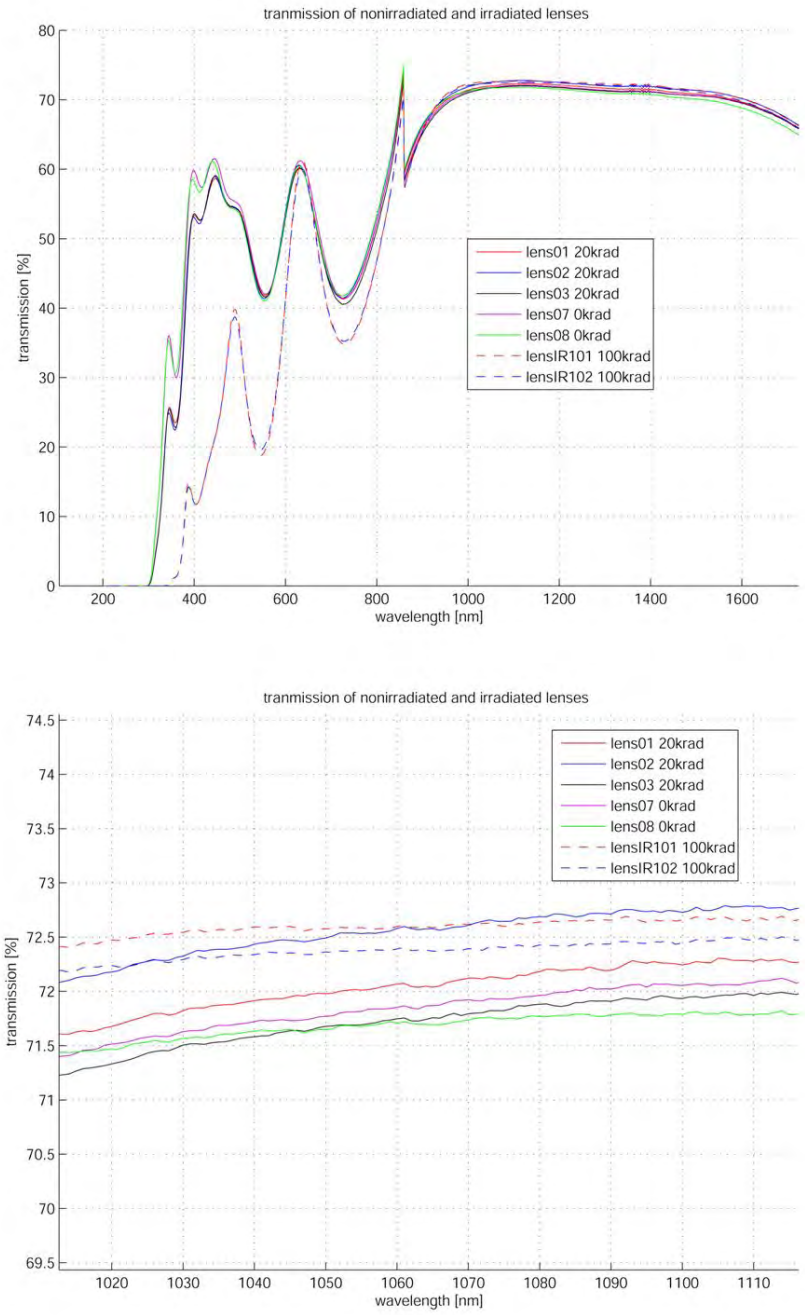

Figure 2.18: Wavelength spectrum and zoom for 1064 nm for irradiated and non-irradiated lenses.

Figure 2.18 shows the wavelength spectrum of irradiated and non-irradiated lenses. It is easy to observe that the irradiation changes the lens performance in the visible light spectrum with a loss of ~50 %. In the wavelength range of around 1060 nm no difference can be detected.

2.2.3 Conclusion of spectrophotometer measurements

The measurement results are concluded in following table 2.4. There is no significant detectable difference between irradiated and non-irradiated samples.

coating or material	0 krad	20 krad	100 krad
mirror HR	99.89 ± 0.014 %	99.89 ± 0.014 %	99.86 ± 0.014 %
beamsplitter HR	50 %	49.98 ± 0.13 %	49.54 ± 0.13 %
beamsplitter AR	50 %	49.66 ± 0.13 %	49.66 ± 0.13 %
PBS transmission	s-pol: 48.65 % p-pol: 50.34 %	s-pol: 48.69 % p-pol: 49.66 %	— —
lens transmission	100 %	100.47 ± 0.58 %	100.99 ± 0.21 %

Table 2.4: Measurement results of spectrophotometer measurements.

The transmission measurements of the mirrors are converted to reflectivity (R = 100 % - T in %) assuming no loss due to absorption. The beamsplitter HR and AR measurements are normalised, so that a direct comparison can be made between the irradiated and the non-irradiated components from the same batch. Also the lens measurement has been normalised.

2.3 Characterisation of optical non-flight model components

For the construction of the optical prototype bench (OPB) a supplier of optical components has been chosen that differs from the supplier of LTP flight optics. A few optical components from this alternative supplier have also been irradiated with 20 krad and 100 krad. These components were tested using a spectrophotometer in the same way as the flight model components. The analysis of the results shows that these coatings have also not been affected by the irradiation. This research was carried out to investigate other coating qualities from an other supplier also in the interest of forthcoming projects like LISA.

The following three pages compare the flight model coatings (above) with the coatings of the OPB (below). Figure 2.19 shows the wavelength spectrum of the mirrors. The difference between the two coating is easy to observe. Instead of one bandwidth (minimum) the OPB shows two bandwidth (minima) around 800 nm and 1100 nm. Figures 2.20 and figure 2.25 compare the beamsplitter coatings with each other. These curves are quite similar.

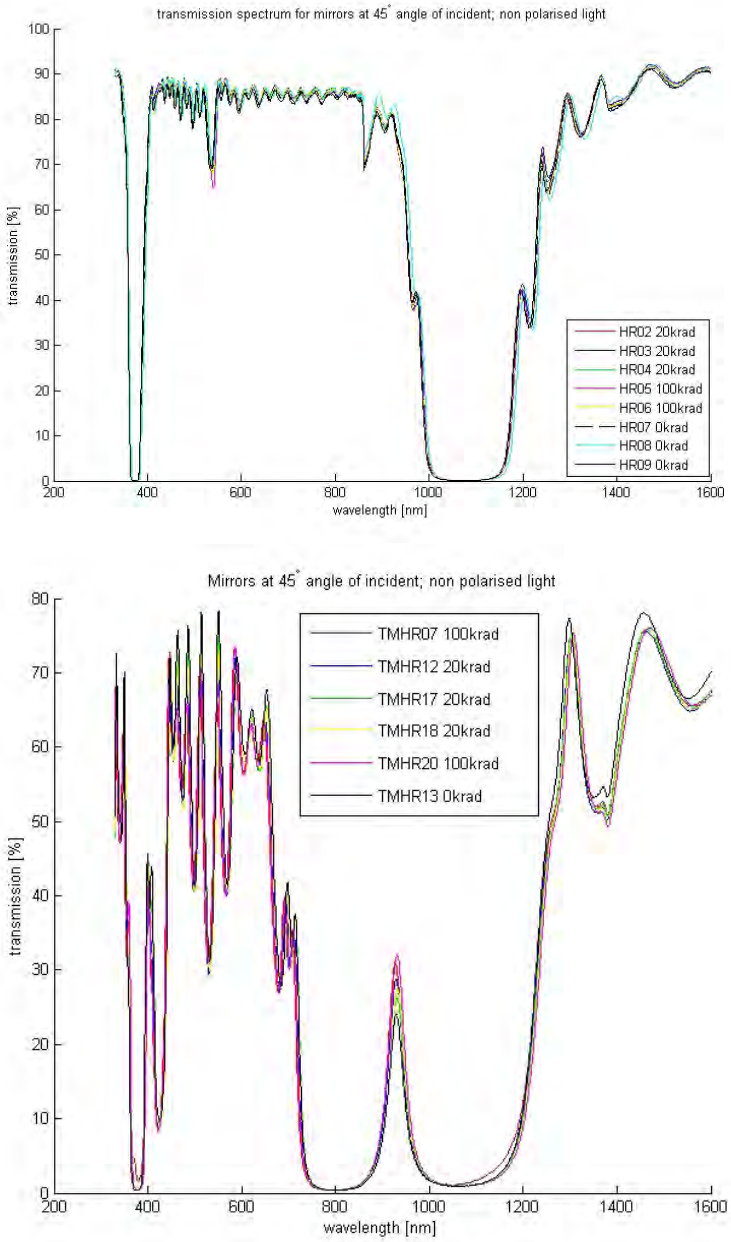

Figure 2.19: Wavelength spectrum of flight model coating compare to another coating for irradiated and non-irradiated mirrors.

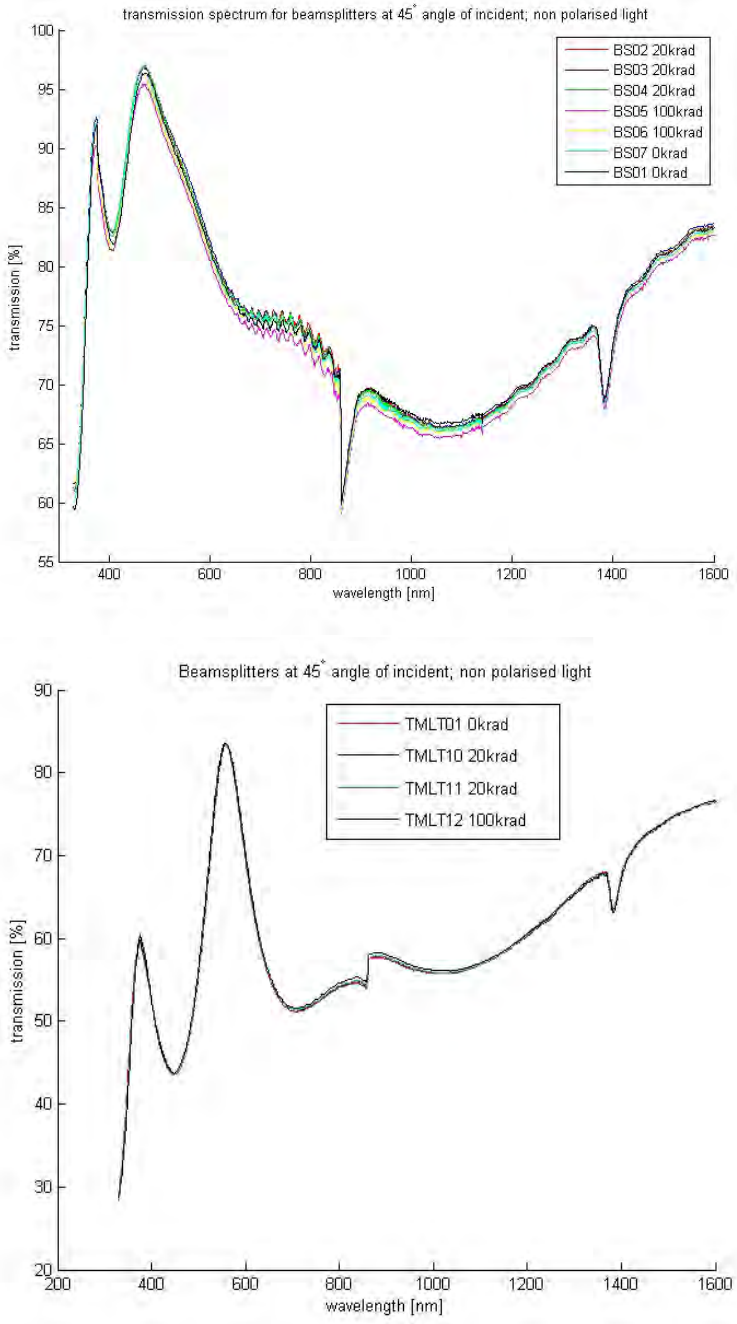

Figure 2.20: Wavelength spectrum of flight model coating compare to another coating for irradiated and non-irradiated beamsplitter.

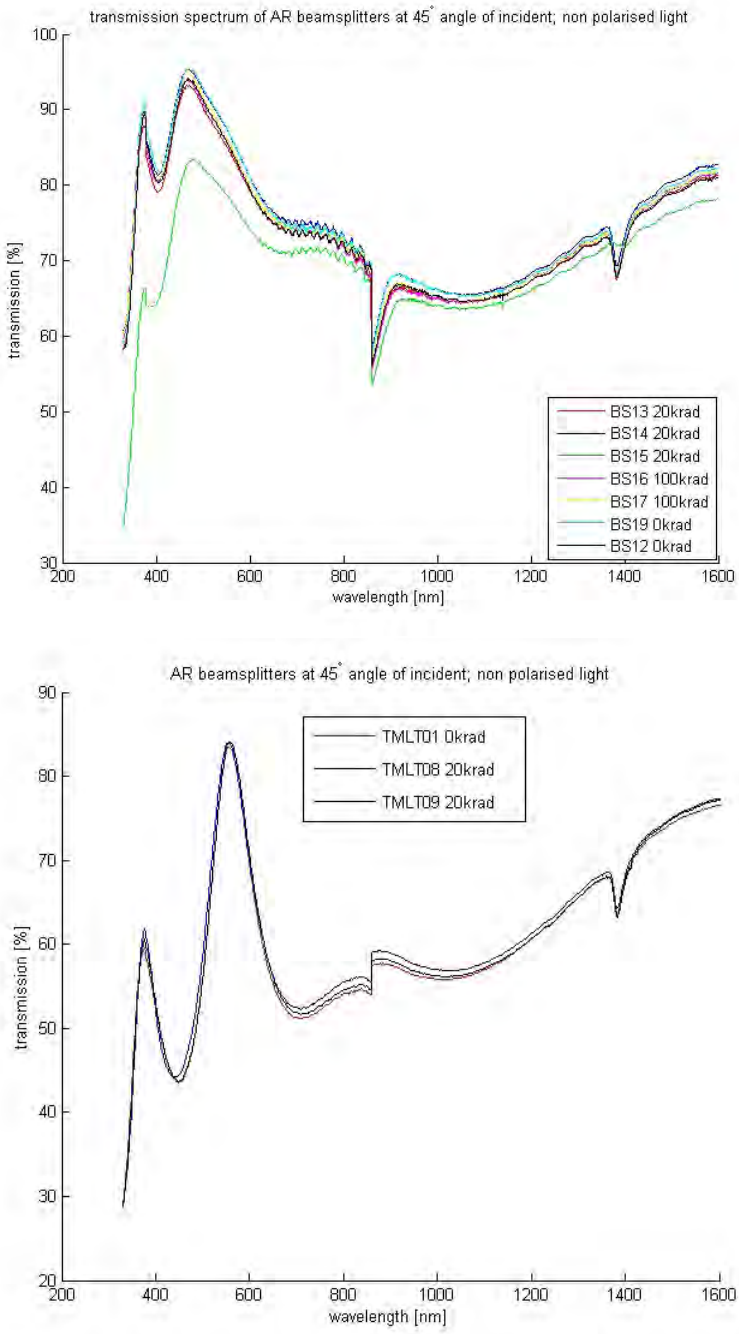

Figure 2.21: Wavelength spectrum of flight model coating compare to another coating for irradiated and non-irradiated AR coating of beamsplitter.

2.4 Investigation of optical windows

Optical windows are mounted in the walls of the vacuum tanks, which are housing the two test masses. As transmitted optics they form a part of the interferometer. The beam of the X1 interferometer passes through an optical window twice during its path from the optical bench to the test mass and back. In the case of the X1 - X2 interferometer the beam passes through two optical windows and will have in total four transits. Therefore an investigation of the windows is very necessary. The substrate material of the optical window is an Ohara glass [31]. The optical windows are coated on one side with a common AR (anti-reflection) coating and on the other side an indium tin oxide (ITO) coating. ITO coating is a conductive high transmission coating for visual and near infra-red. AR coatings are non-conductive, but inside the vacuum tank, due to the discharging properties required, it is necessary that the inner window's surface is a conductor.
This section describes the experiment and results of the transmission of a 1064 nm beam through Ohara glass windows with ITO - AR coating compared with non-coated Ohara glass windows before and after irradiation with doses of 30 krad. Two Ohara glasses have been measured without coating, and two windows with coating. Furthermore, spectrophotometer measurements of irradiated and non-irradiated windows are presented and compared to common AR - AR coated windows.

2.4.1 Transmission investigation at 1064 nm of optical windows

Figure 2.22 shows the set-up for measuring the transmission through an optical window. In front of the fibre coupler is an absorptive neutral density filter to

ensure that the photodiodes are not saturating. Then the beam passes through a polarisation beamsplitter to maintain s-polarisation. To stabilise the laser beam intensity, a 10 % beamsplitter reflects light to a photodiode, which provides the signal for the feedback system. The beam transmits through the optical window at zero incidence. To avoid back reflection the window was tilted slightly downwards. To reduce stray light an iris is placed in the beam before the transmitted beam is measured using a photodiode. The transmission of each optical window was measured in both directions. Nine measurement pairs ($U_{w/o}$; U_{with}) were taken; each pair consists of a first measurement without the window ($U_{w/o}$) and second measurement with the window (U_{with}) in place.

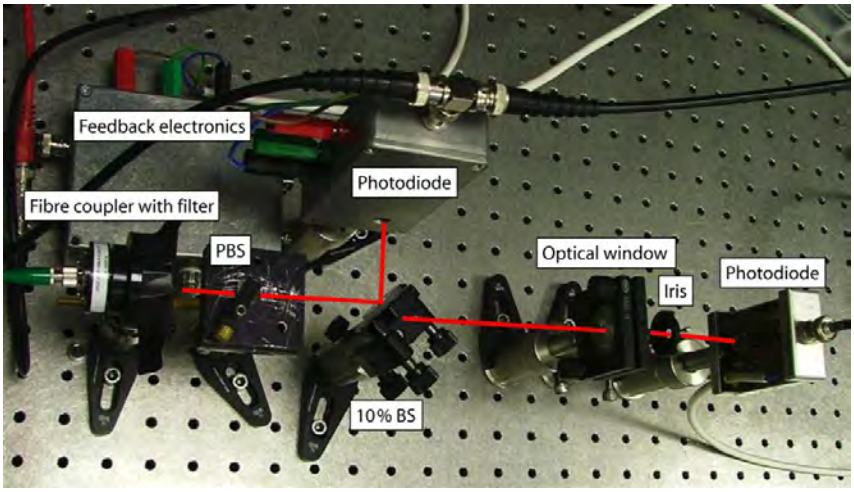

Figure 2.22: Picture of the experimental set up.

The transmission (T) of the beam through an optical window is defined by:

$$T_{1,...,9} = (U_{with}/U_{w/o}) \times 100\,\%$$

To get a reliable transmission factor of each optical window and its orientation towards the beam, the average of the nine measurements were taken and the standard deviation gives the uncertainty:

$$T = 1/9\,\Sigma\,(T_1 + ... + T)_9) \pm \mathrm{stdev}\,(T_1, ..., T_9)\,\%$$

In the case of non-coated optical windows a definite conclusion cannot be made due to the high uncertainty of the measurements. This is due to the fact that a non-coated optical window will have multiple reflections, which may interfere with the measurement and influence the beam position, size and intensity on the photodiode. For the coated optical window this is not the case and the uncertainty is of a factor of 5 - 10 times smaller than for non-coated surfaces. It can be said that the coated optical windows experience a loss of $\sim 1\,\%$ of transmission after irradiation. Each window was measured twice; once from each side. The windows are labelled and one side is indicated with the symbol "<". In the case that the windows has an ITO coating the symbol is pointing to that side. The transmission measurements of optical windows before and after irradiation are concluded in table 2.5; "<" means that the ITO side is pointing towards the incoming beam and ">" the opposite.

component	transmission in % before irradiation	transmission in % after irradiation
01 non-coated <	92.9 ± 3.8	88.4 ± 4.5
01 non-coated >	90.3 ± 3.6	87.5 ± 1.9
02 non-coated <	88.4 ± 3.0	89.0 ± 2.1
02 non-coated >	83.8 ± 2.5	88.6 ± 1.9
03 ITO – AR <	98.3 ± 0.1	97.3 ± 0.3
03 ITO – AR >	98.1 ± 0.4	97.3 ± 0.2
04 ITO – AR <	97.7 ± 0.4	96.4 ± 0.6
04 ITO – AR >	97.7 ± 0.3	96.7 ± 0.6

Table 2.5: Transmission measurements of optical windows before and after irradiation; "<" indicated the side of the component towards the incoming beam.

2.4.2 Transmission and reflection measurements using a spectrophotometer

The transmission and reflection of optical windows were measured using a spectrophotometer. A double-sided AR - AR coated window was investigated. The properties of the AR coating are well known and were used for comparison with the ITO - AR coated optical window. This section will compare irradiated and non irradiated ITO - AR coated optical windows with each other and with a non-irradiated AR - AR window.

Figure 2.23 shows the optical window placed inside the spectrophotometer. It shows an irradiated window that has been exposed to a dose of 30 krad. It is easy to see that the window has changed from transparent clear to yellowish after irradiation. The window was measured with unpolarised light at zero incidence.

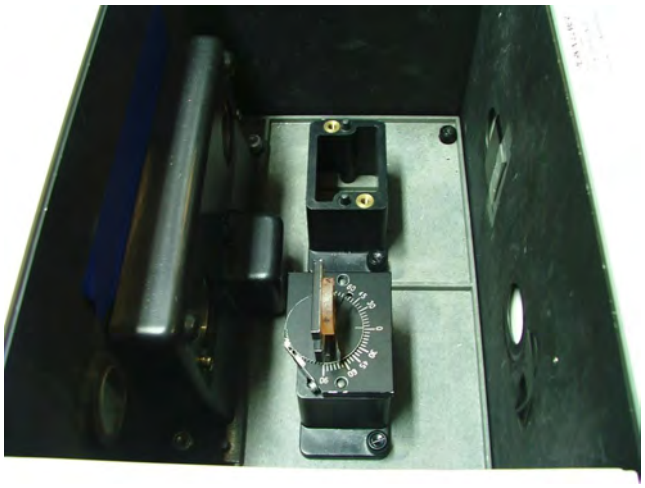

Figure 2.23: Optical window mounted for transmission measurement.

Figure 2.24 shows the set-up for measuring directly the reflection of an optical surface. For this purpose two identical reflective elements are placed one in

the reference path and one in the measurement path. The path of the beam is indicated in figure 2.24. The schematic drawing illustrates the red-dotted beam path in the picture: the beam is reflected onto the surface under test and back-reflected to its previously path. Due to the reflective element the angle of incidence is 6°. Since the back-reflection from an AR coating is negligible, it can be assumed that the measured reflection is only caused by the ITO coating.

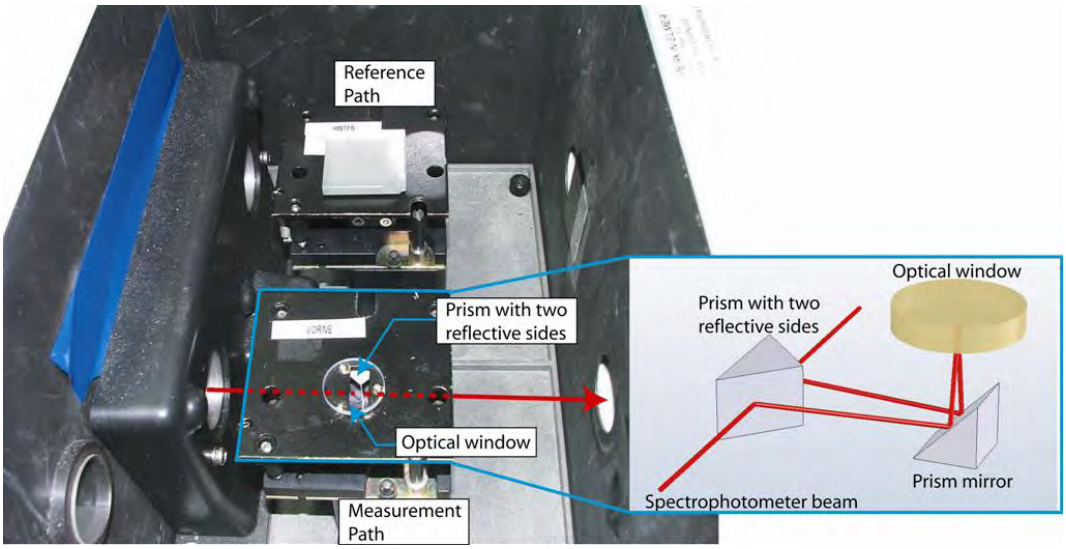

Figure 2.24: Optical window mounted for reflection measurement; the beam path is indicated in red. A schematic drawing explains the beam path inside the mount.

The wavelength spectrum in transmission and reflection including a zoom-in around 1060 nm is shown in figure 2.25 and in figure 2.26. The AR - AR coated optical window has, as expected, a very high transmission of 99.9 % at 1064 nm and negligible reflection. Comparing it to the average of the three non-irradiated and irradiated ITO - AR coated windows shows that they have a much lower transmission of approximately 97.60 % at 1064 nm. Therefore 2.4 % of the light is getting lost in absorption and reflection. Investigation

of the reflection shows that 0.56 % is getting reflected from the ITO surface. That would imply ~ 2 % absorption of the ITO coating. Furthermore it is easy to see that the Ohara glass substrate shows significant radiation damage for transmission of UV-visible light. Comparison of non-irradiated and irradiated windows with each other at 1064 nm show a loss in the transmission of 0.56 % and 0.26 %, which is much smaller than previous measurements with a Nd:YAG set-up (see table 2.5).

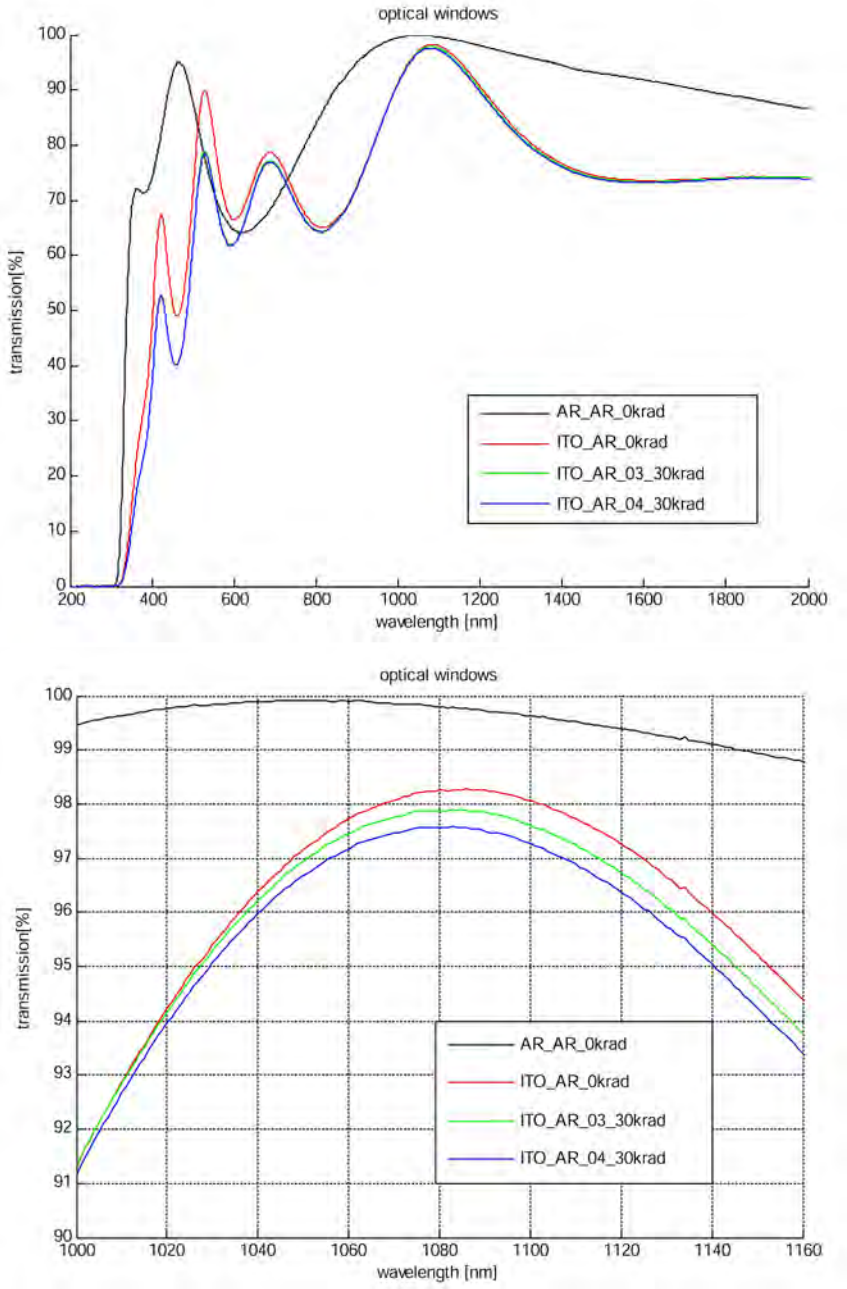

Figure 2.25: Wavelength spectrum of irradiated and non-irradiated optical windows in transmission.

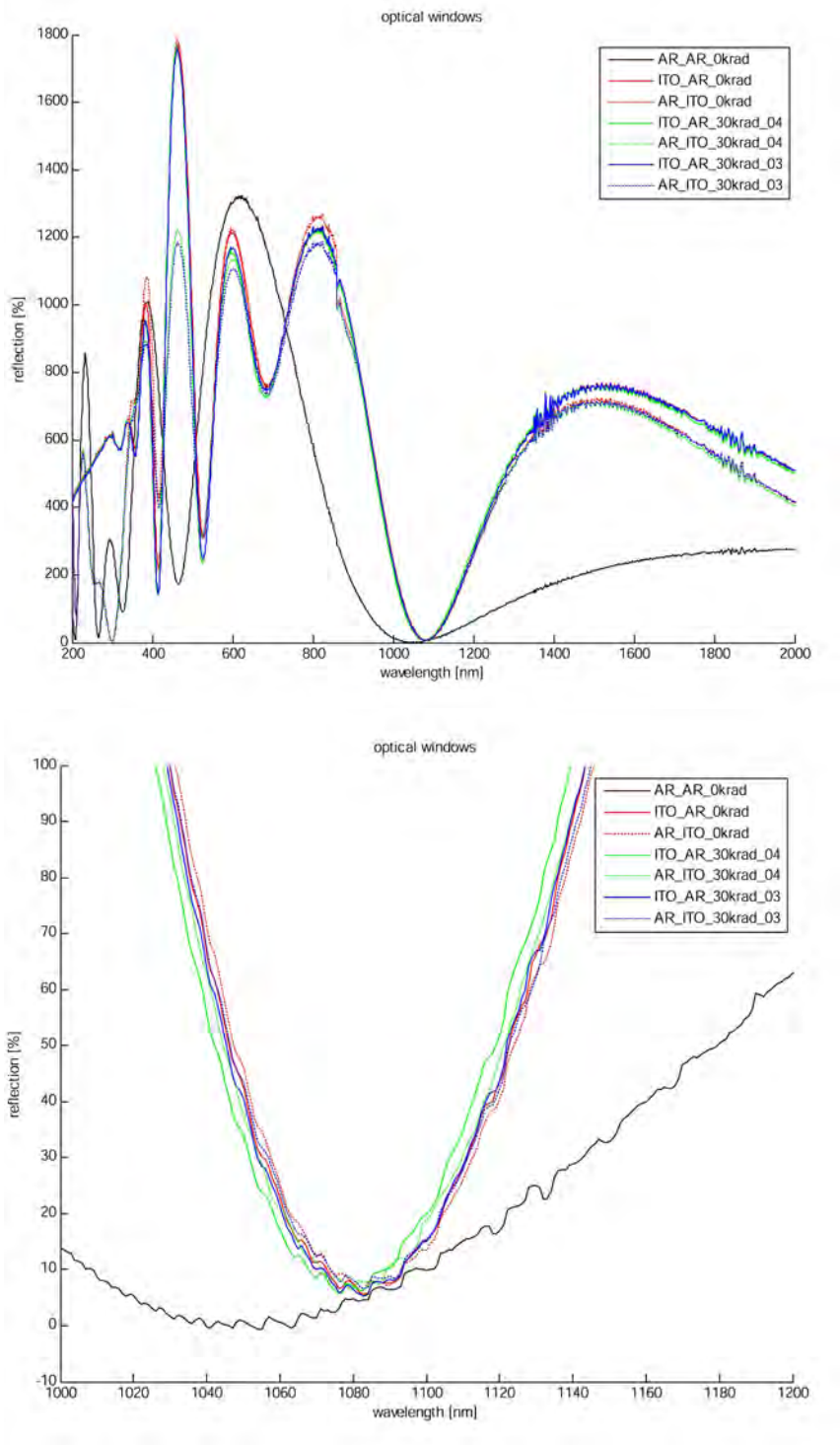

Figure 2.26: Wavelength spectrum of irradiated and non-irradiated optical windows in reflection.

Chapter 3

Characterisation of LTP OBI flight model components

This section describes the measurement of the optical coatings of the beamsplitters and mirrors for the optical bench of the LTP project. Each one optical component of the three types of beamsplitters of the flight model components batches were chosen. The optical properties of the beamsplitting coating and the anti-reflection (AR) coating were measured. The reflection from the AR coating is higher than expected, and it is significantly different from earlier qualification test samples (see chapter 2), and more importantly it is out of specification. This could be a problem for the LTP interferometer performance. This section presents the experimental set-up and results of measuring the reflection of both optical surfaces of the beamsplitter. The author also presents a metrology measurement of the thickness of the AR coating on the flight component and compares it with the same coating on the qualification test sample. Furthermore, spectrophotometer measurements of the mirrors are presented. The mirror coating is similar to the qualification test samples and fulfills the requirements.

3.1 Characterisation of flight model beamsplitters

The optical components and their specifications are listed in table 3.1. One example of each flight model component has been chosen and tested.

component label	component description	coating properties of surface 1	coating properties of surface 2
S2-UGL-DRW-3014-06	beamsplitter	R = 0.50 ± 0.01, T = 0.50 ± 0.01, λ = 1064 nm, s-pol, AoI 45° ± 2°	R ≤0.002 (at nominal angle), λ = 1064 nm, s-pol, AoI 45° ± 2°
S2-UGL-DRW-3015-06	input beamsplitter	uncoated	R ≤0.002 (at nominal angle), λ = 1064 nm, s-pol, AoI 45° ± 2°
S2-UGL-DRW-3016-06	beamsplitter combiner	R = 0.50 ± 0.01, T = 0.50 ± 0.01, λ = 1064 nm, s-pol, AoI 45° ± 2°	R ≤0.002 (at nominal angle), λ = 1064 nm, s-pol, AoI 45° ± 2°

Table 3.1: List of components under investigation (R ≡ reflection; T ≡ transmission); AoI ≡ angle of incidence.

3.1.1 Experiment set-up

The experimental set-up is shown in figure 3.1. The light source is a Nd:YAG laser operating at λ = 1064 nm. The laser operates in a single spatial mode

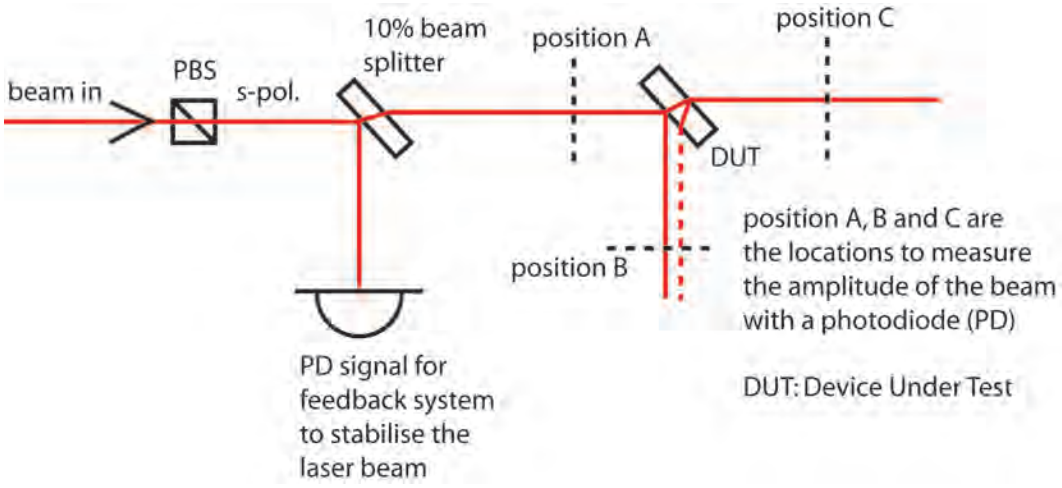

Figure 3.1: Optical window mounted for reflection measurement.

and single frequency. The light is filtered through a polarisation preserving single mode optical fibre before being coupled in to this experiment. The incoming beam passes through a polarising beamsplitter (PBS) to maintain s-polarisation (s-pol). The laser beam power is stabilised by a feedback system, which monitors the beam power close to the actual experiment and feeds back to the laser current. The device under test (DUT) in this case are flight coated beamsplitters, see table 3.1. They are mounted such that the incoming beam hits the DUT with a $45 \pm 1\,^{\circ}$ degree angle of incidence (AoI). The beam power is measured using a photodiode (PD) at the position A, which gives the total input beam amplitude, and at position B and position C. At position B there are two beams to measure, first the beam reflected from the front surface of the DUT and second the beam reflected of the back surface of the DUT. These beams have a separation of 5.5 mm and a radius of ~ 0.6 mm so it is relatively easy to block one without affecting the other beam. During measurement at position B the other beam is blocked using an iris (not shown in figure 3.1). The transmitted beam is measured at position C.

3.1.2 Measurement analysis

Measurements of both the division ratio of the beamsplitter coating and the reflection of the AR coating were investigated. Two cases have to be considered: the "incoming beam" hits surface "x" in the figure 3.2 and "y" in figure 3.3, where part of the beam is reflected (reflection A) at an angle of 45 ° degrees. The other part of the beam passes through the component. The beam inside the material is labelled "A". When "A" hits the back surface – "y" in the figure 3.2 and "x" in figure 3.3 – part of it will be reflected and the other part transmitted (transmitted beam). The reflected beam labelled "B" inside the material hits the front surface again where part of it will be reflected (not shown in figure) and part of it will be transmitted (reflected B). Throughout the analysis we will assume that there is no significant absorption of the light in either the coating or the bulk material of the components. Table 3.2 shows the labelling used in the analysis and figures.

Incoming beam	BI	measured directly
Transmitted beam	BT	measured directly
Reflection A	RA	measured directly
Reflection B	RB	measured directly
internal transmission beam	A	inside material
internal reflection beam	B	inside material

Table 3.2: Used acronyms in analysis and drawings.

The incoming beam hits the beamsplitter coated side first with an angle of incidence of 45 ° degree:

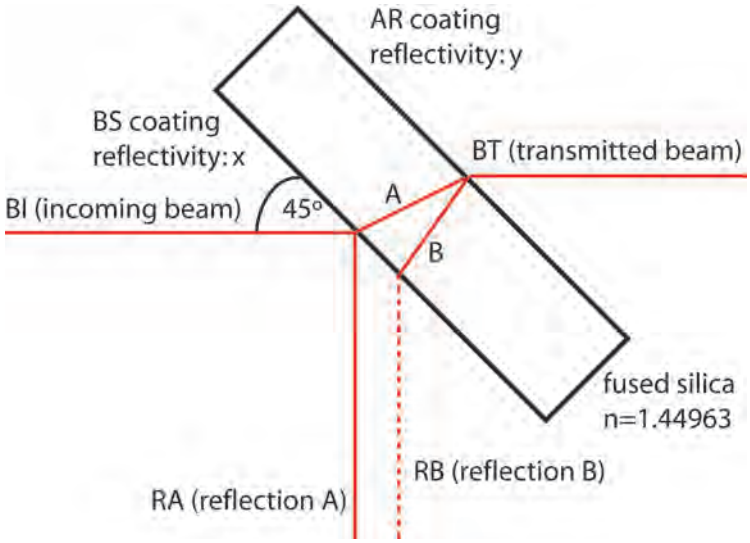

Figure 3.2: Schematic drawing of the beamsplitter with the beamsplitter coated side facing towards the incoming beam.

Calculation of beamsplitter coating reflectivity x:

$$x = \frac{RA}{BI} \tag{3.1}$$

Calculation of AR coating reflectivity y:

$$y = \frac{B}{A} \tag{3.2}$$

$$\text{with } A = BI - RA$$

$$\text{and with } B = \frac{RB}{(1-x)}$$

$$\Rightarrow y = \frac{RB}{((1-x)(BI-RA)} \tag{3.3}$$

The incoming beam hits the anti reflection (AR) coated side first with an angle of incidence of 45 ° degree:

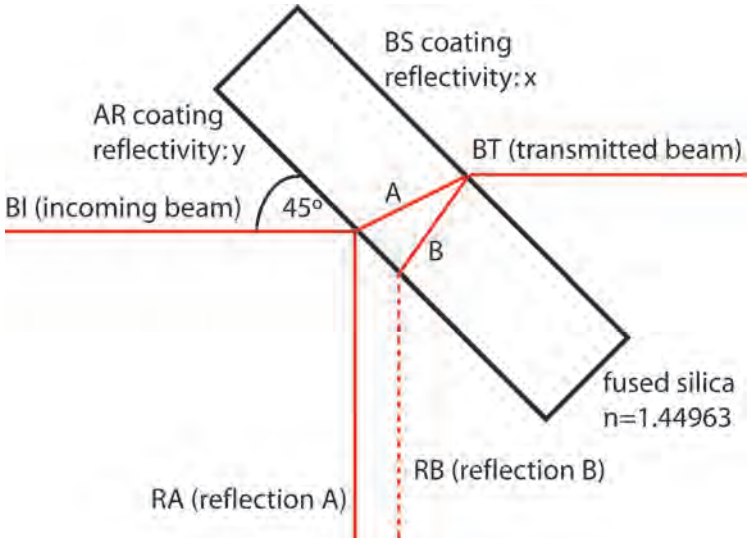

Figure 3.3: Schematic drawing of the beamsplitter with the anti-reflection (AR) coated side facing towards the incoming beam.

Calculation of beamsplitter coating reflectivity x:

$$x = \frac{B}{A} \tag{3.4}$$

$$\text{with } B = \frac{RB}{(1-y)}$$

$$\text{and with } A = BI - RA$$

$$\Rightarrow x = \frac{RB}{((1-y)(BI-RA))} \tag{3.5}$$

or

$$x = 1 - \frac{BT}{A} \tag{3.6}$$

$$\Rightarrow x = 1 - \frac{BT}{(BI-RA)} \tag{3.7}$$

Calculation of AR coating reflectivity y:

$$y = \frac{RA}{BI} \tag{3.8}$$

3.1.3 Measurement results

The reflectivity of the beamsplitter coating is within specification and requirement with a reflectivity of $49.4 \pm 0.5\,\%$.
The measurements show that the reflectivity of the AR coating is $1.3 \pm 0.1\,\%$. This is significantly above the requirement of $1\,\%$ [30] and the specification in table 3.1. Furthermore there is an inconsistency with the pre-tests of the flight model optical coating applied to qualification test samples, see chapter 2, where the measurements have shown a AR reflectivity of $0.6\,\%$. Therefore further investigation were carried out to distinguish a possible difference between coating runs. As a summary it can be said that no reason was found either in the measuring set-up or in the actual coating. There was no information given by the coating company of a differences in the coating procedure. These coating runs were claimed to be carried out to the same ISO standard.

The correlation between polarisation of the beam and coating behaviour was investigated. The coatings are specified for s-polarisation. The set-up was the same as in figure 3.1, but with the addition of a polarising beamsplitter (PBS) in the beam between the $10\,\%$ beamsplitter and position A. The PBS was mounted in a rotation stage and aligned perpendicular to the incoming beam. To calibrate the rotation of the PBS inside the mount, the maximum and minimum throughput of the beam was used; this was done with an uncertainty of $\pm 2\,^\circ$ degrees. The maximum throughput was measured at $60\,^\circ$ degrees on the rotation stage display and the minimum throughput at $330\,^\circ$ degrees. Thus $60\,^\circ$ degrees corresponds to s-polarisation. To vary the input polarisation the rotation stage was rotated by $\pm 10\,^\circ$ degrees in $2\,^\circ$ degree steps and the reflected beam from the beamsplitter coating and of the AR coating was measured. The analysis is similar to the previous calculation.

Figure 3.4 shows the reflectivity of the beamsplitter coating depending on polarisation. The reflectivity is in the range of 0.497 and 0.481 in a rotation of $\pm 10\,^{\circ}$ degrees. Therefore it can be said that the coating performance is not significantly dependent on the polarisation of the incoming beam in the range of $\pm 6\,^{\circ}$ degree ($R = 0.5 \pm 0.1$).

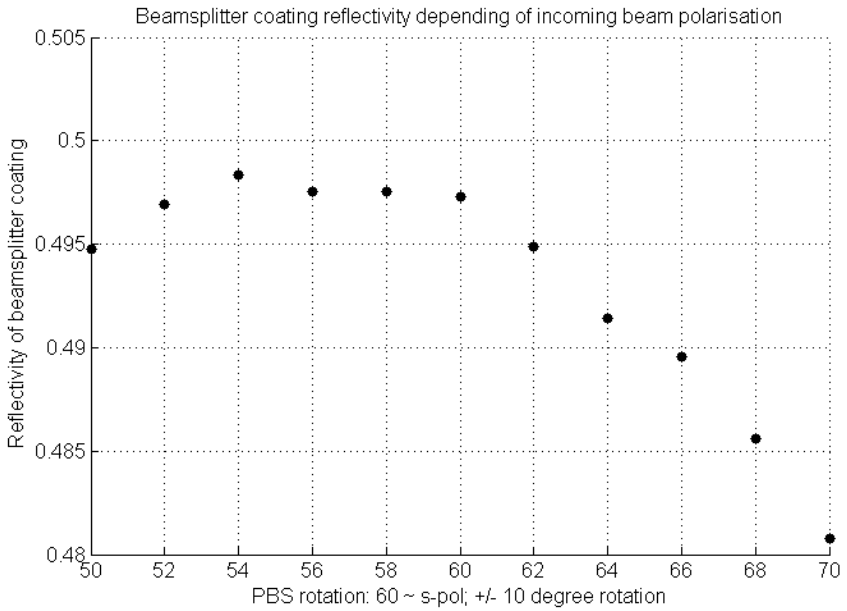

Figure 3.4: Beamsplitter coating reflectivity depending of polarisation.

Figure 3.5 shows the reflectivity of the AR coating dependence on the incoming beam polarisation. The reflectivity does not show a correlation to the polarisation in the range of $\pm 10\,^{\circ}$ degree change of polarisation. The reflectivity fluctuates around 1.35 % over the entire range.

A difference of the coating charge between the qualification tests samples and the flight components in terms of coating thickness was also not seen. A design feature of these optical components is that the coating does not extend over the full surface. This allows us to measure the height of the coating using a 2D Taylor Hobson surface profiler. Two samples were tested, a qualifica-

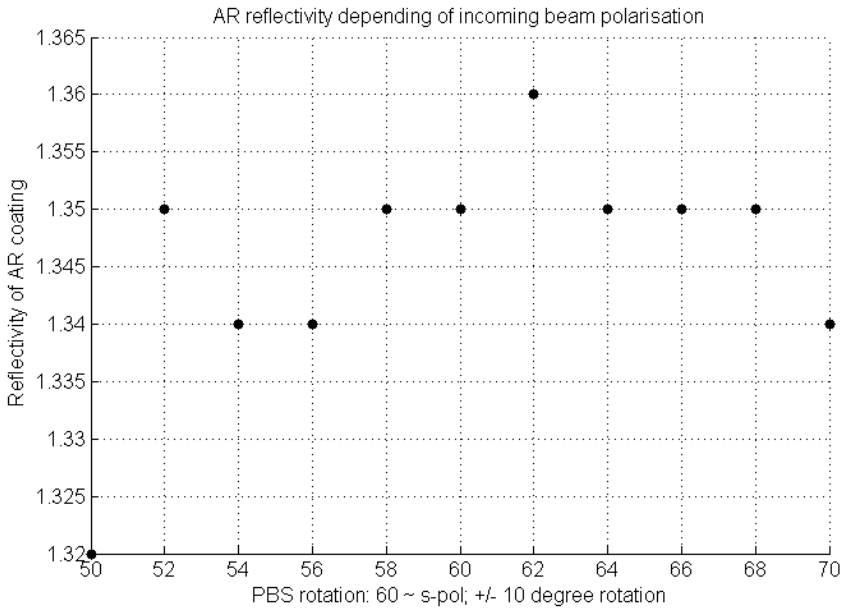

Figure 3.5: AR reflectivity depending on incoming beam polarisation.

tion test run sample (BS07) with acceptable AR coating, and a flight model beamsplitter with the higher reflectivity AR coating. The results of these two measurements are shown in figure 3.6 and figure 3.7. Comparing figure 3.6 and figure 3.7 shows that both coating runs provided a similar coating thickness with an average of 0.35 microns.

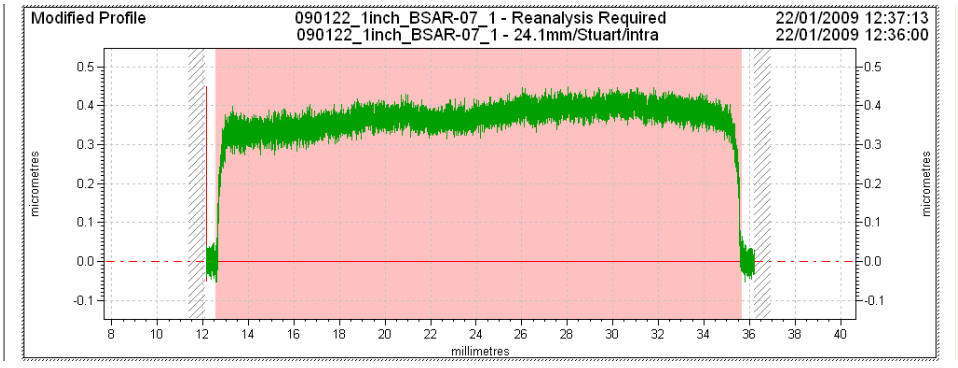

Figure 3.6: 2D scan of the surface profile of the flight model qualification AR coating; marked in red is the area where the coating is applied to the surface.

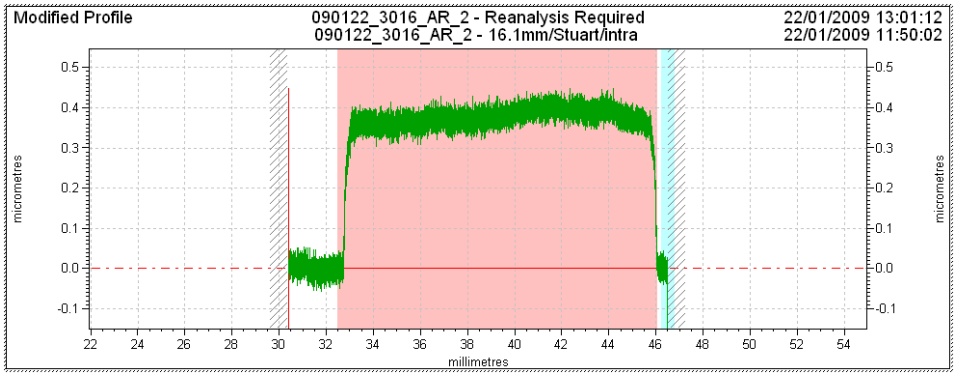

Figure 3.7: 2D scan of the surface profile of the flight model AR coating; marked in red is the area where the coating is applied to the surface.

3.2 Characterisation of flight model optical components using a spectrophotometer

One of each of the coated flight model components was measured using a spectrophotometer. Unknown polarised light was used and the component was mounted with the angle of incidence (AoI) for which the component was coated. Figure 3.8 shows the measurement curve of each of the components. Due to the fact that unknown polarised light was used and that the components have a thickness of 7 mm, the measurements of the beamsplitter coating are not absolute values of the transmission for which the beamsplitter was designed. The mirror with the coating for 45 ° degree AoI shows a reflectivity $R \geq 99.7$ in the bandwidth of 1050 - 1125 nm, and in the case of the mirror with coating 22.5 ° degree AoI it shows a reflectivity $R \geq 99.7$ in the bandwidth of 1032 - 1168 nm. Interestingly, the "input beamsplitter" - a beamsplitter with only an AR coating and a non-coated beamsplitter side - shows an extremely low transmission compared to a non-coated fused silica reference piece of 1 mm thickness. The transmission of the reference piece is 91.9 % which equals ~ 4 % reflectivity of each surface of the reference component, which is the expected

reflectivity of a non-coated fused silica surface. The input beamsplitter shows a transmission of ~86.9 %. Assuming that the reflectivity of the non-coated surface of the component is 4 % would result in a reflectivity of the AR coating of ~9 %. This can only be explained by taking into account that the polarisation of the spectrophotometer is not aligned for s - polarisation. To prove that a test with p - polarised light was carried out using a 1064 nm laser.

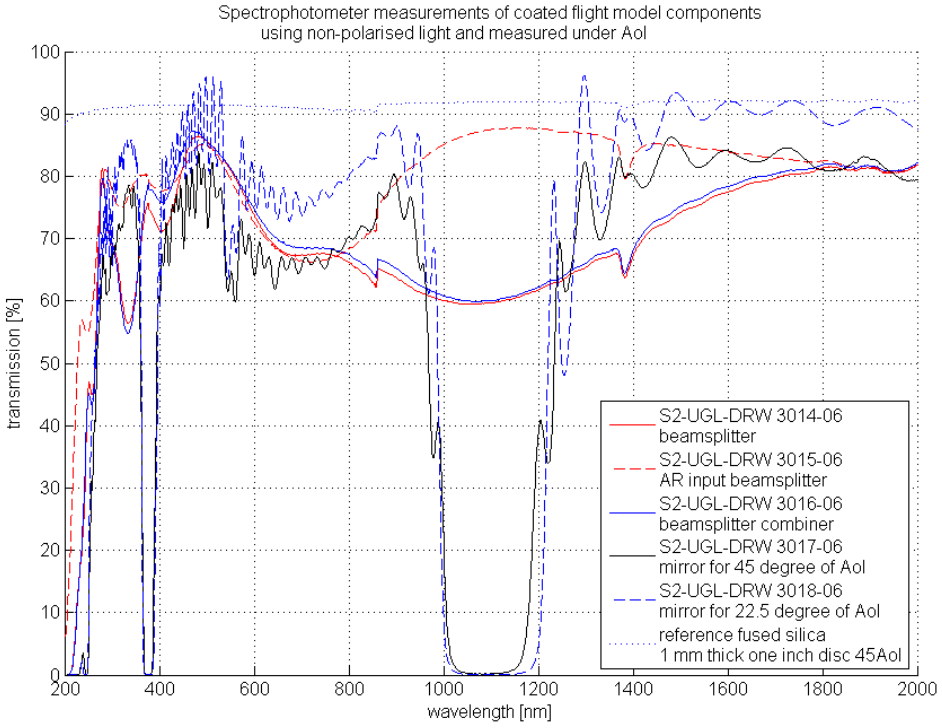

Figure 3.8: Spectrophotometer measurements of coated flight model components.

3.2.1 AR coating reflectivity at p - polarisation

A PBS was set up in front of the "input beamsplitter" on the same stage as the beamsplitter, using a half wave plate the beam was set-up such that the

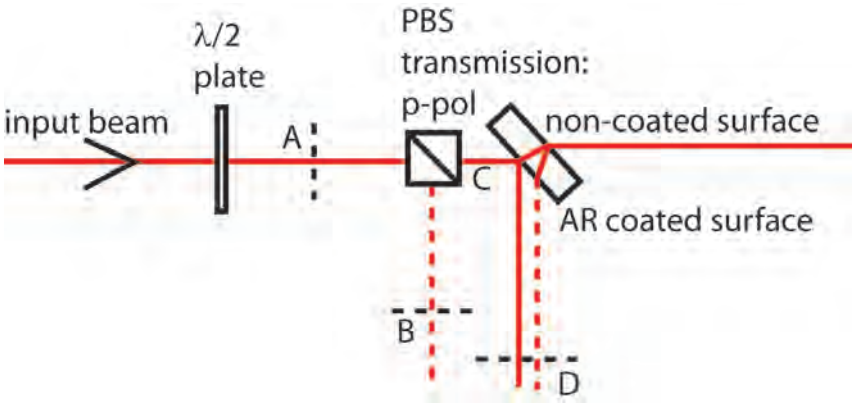

Figure 3.9: Set-up for measuring the reflection of the AR coating at p-polarisation.

maximum throughput of the PBS was p-polarised light. The beam power was measured using a photodiode at the position A, B and D. At the position C measurements were not taken. At the position D two measurements were taken; the reflection of the front surface (the AR coated surface) and the reflection of the back surface (the non coated surface). The half wave plate was aligned to a minimum beam power at position B. The following analysis was carried out:

$$\begin{aligned} \text{Total power of p-polarised beam: } C &= A - B \\ \text{Reflectivity of the AR coated surface: } R_{AR} &= \frac{D_{AR}}{C} \\ \text{Reflectivity of the non coated surface: } R_{non} &= \frac{D_{non}}{C - D_{AR}} \end{aligned}$$

In the case of the AR coated surface a reflectivity of 8.9 % was measured. The non-coated surface showed a reflectivity of 5.8 %. Therefore a total reflectivity of 14.7 % was measured. This explains the high reflectivity of the input beam-splitter of 13.5 % at the spectrophotometer measurement (assuming that the used measurement beam of the spectrophotometer was mainly p-polarised).

Chapter 4

Optical bench interferometer

The monitoring system of LTP must be able to handle a range of movement of the proof masses of a few hundred microns. The required displacement measuring precision is $10\,\mathrm{pm}/\sqrt{\mathrm{Hz}}$ at the frequencies band of 3 - 30 mHz. Hence the requirement is to have an interferometer with a wide dynamic range as well as high sensitivity. For this reason, a homodyne interferometer is not suitable, because it has a normal operating point – the dark fringe. The best choice is a heterodyne operating Mach-Zehnder interferometer [16] as explained in this chapter. A detailed design of the interferometer is given and associated hardware components – the laser and acousto-optical modulators – are described.

4.1 Modulation Bench

The principle of the Mach Zehnder interferometer is explained in figure 4.1. The incoming beam is divided into two identical arms using a 50:50 beam-

splitter. In a heterodyne interferometer two beams are frequency shifted by traveling through an acusto-optical modulator (AOM), such that for instance,

$$f_{beam1} = f_0 + (80\,\text{MHz} - 500\,\text{Hz}) \tag{4.1}$$

$$f_{beam2} = f_0 + (80\,\text{MHz} + 500\,\text{Hz}) \tag{4.2}$$

where f_0 is the frequency of the incoming beam. The heterodyne frequency is then

$$f_{het} = f_2 - f_1 = 1\,\text{kHz} \tag{4.3}$$

Afterwards both beams are superposed and the heterodyne frequency is measured. Any change in an arm length will be seen as a phase shift $\Delta\phi$ in the heterodyne signal. This change is represented in figure 4.1 by a piezo-electric device as a mount for one of the mirrors. This piezo movement represents any effect that causes tiny changes in the path difference in the interferometer. Common effects which can cause phase shifts, are thermally introduced mechanical and structure deformations. To be able to measure the small phase shifts caused by proof mass movements onboard LTP, it is important to reduce these effects.

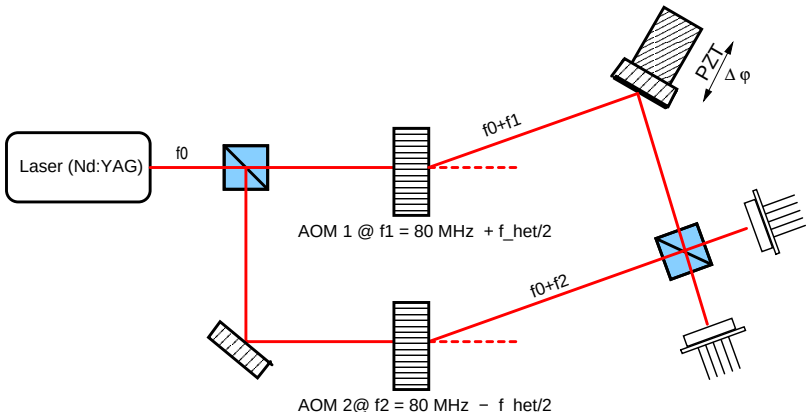

Figure 4.1: Schematic drawing of a heterodyne Mach-Zehnder interferometer.

To obtain the frequency shifted laser beams for a heterodyne interferometer, a modulation bench is used. The bench contains two acousto-optic modulators (AOMs) and their electronics as well as the Nd:YAG laser itself. An AOM consists of a piezoelectric transducer and a piece of tranparent material such as glass or quartz. The piezoelectric transducer is attached to a modulated material in such a way that the oscillating electric signal applied to the transducer creates sound waves in the material. These acoustic waves - usually radio-frequency (RF) - change the local density of the material, and thus the index of refraction changes. The intensity of the single first order is directly linked to the power of the RF control signal. The AOMs used are operated at a frequency around 80 MHz with an efficiency of 85 %. The selected ND:YAG laser, used during construction of the OBI is a INNOLIGHT MEPHISTO 500 delivering up to 500 mW output.

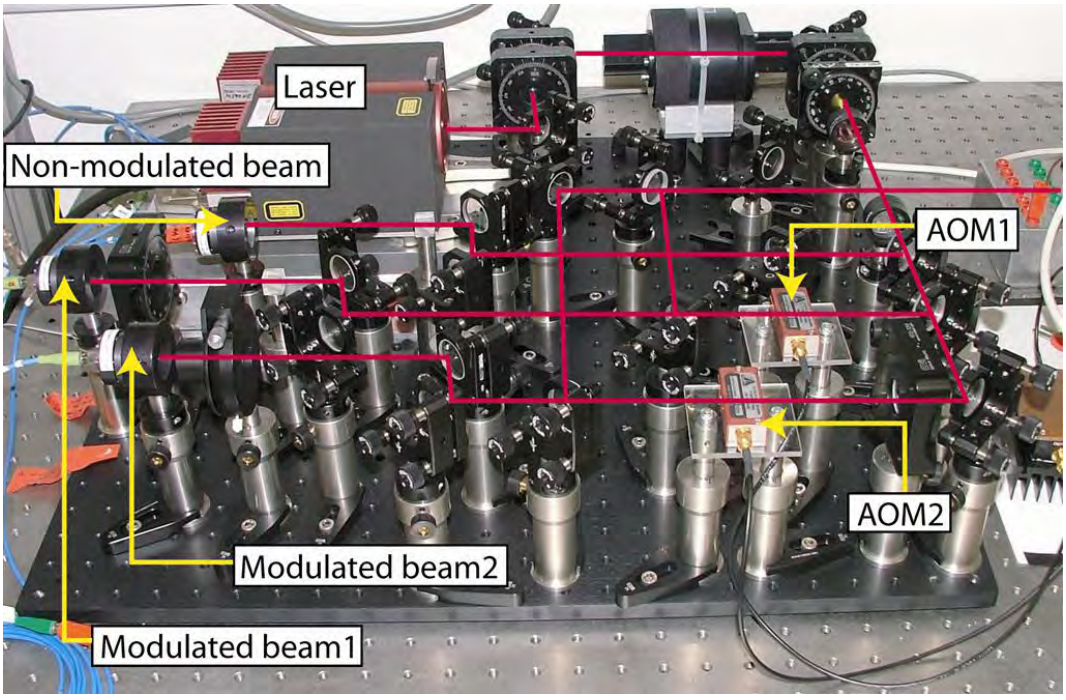

Figure 4.2: Modulation bench set-up (further description in text).

Figure 4.2 shows the modulation bench used in its present state. The Nd:YAG laser is located on the left hand side. The beam travels through several optical elements. Part of this beam is extracted to provide non-modulated light. The remaining beam is then split into two equal-intensity beams which are modulated by the AOMs. Then 10% of each beam is extracted to generate a control heterodyne signal. The transmitted beams are coupled into optical fibres using commercial fibre couplers. These optical fibres are providing light e.g. for the optical LTP prototype bench in a temperature controlled laboratory environment.

The following equation describes the time-dependent progression of the heterodyne signal at the output of a heterodyne interferometer:

$$\begin{aligned} \cos\phi &= \cos\left(\Delta\omega t + \Delta\phi_{meas}\right) \\ &= \cos\left(2\pi f_{het}\cdot t + \frac{2\pi\Delta L}{\lambda}\right), \end{aligned} \tag{4.4}$$

where $\Delta\phi_{meas} = \frac{2\pi\Delta L}{\lambda}$ and Δ L is the path length difference between the two arms of the interferometer.

Figure 4.3 shows the schematic set-up of a reference interferometer and a measurement interferometer. On the left hand side is shown the modulation bench set-up and on the right hand side the ultra-stable optical bench. The arm lengths of the interferometers are divided into three regions: L1 and L2 are the arm length segments outside of the ultra-stable optical bench, and are sensitive to phase-shifts induced by mechanical and thermal fluctuations. L1M, L2M, L1R and L2R are optical path length segments on the ultra-stable bench. The phase shift in the measurement interferometer is given by following equation:

$$\phi_M = 2\pi f_{het}\cdot t + \frac{2\pi}{\lambda}\cdot(\mathrm{L1} + \mathrm{L1M} - \mathrm{L2} - \mathrm{L2M}) \tag{4.5}$$

Similarly, the phase in the reference interferometer is given by.

$$\phi_R = 2\pi f_{het} \cdot t + \frac{2\pi}{\lambda} \cdot (\mathrm{L1} + \mathrm{L1R} - \mathrm{L2} - \mathrm{L2R}) \tag{4.6}$$

Subtracting of equation(4.5) from equation (4.6) we get.

$$\phi_M - \phi_R = \mathrm{L1M} - \mathrm{L1R} - \mathrm{L2M} + \mathrm{L2R}$$

This result is independent of L1 and L2 and since the optical path length differences of the reference interferometer are constant on an ultra stabile optical bench:

$$\phi_M - \phi_R = \mathrm{L1M} - \mathrm{L2M} + \mathrm{const.}$$

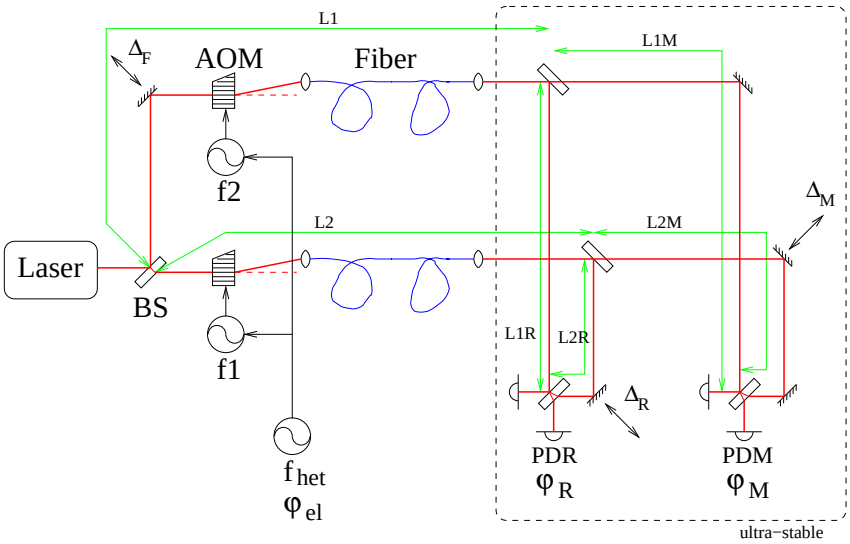

Figure 4.3: Measuring of a path length difference. A list of acronyms can be found in table 4.1 on the next page.

Consequently, optical path length differences can be determined by measuring phase differences by having a reference and a measurement interferometer on an ultra stable optical bench.

labelled acronyms	discretion
BS	beamsplitter
AOM	acoustic-optic modulator
f2	frequency 2
f1	frequency 1
f_{het}	heterodyne frequency
ϕ_{el}	electronics input phase
ϕ_R	reference output phase
ϕ_M	measurement output phase
L1	length 1 to ultra-stable bench
L2	length 2 to ultra-stable bench
L1M	length 1 on ultra-stable bench in measurement path
L2M	length 2 on ultra-stable bench in measurement path
L1R	length 1 on ultra-stable bench in reference path
L2R	length 2 on ultra-stable bench in reference path
PDR	reference interferometer photodiode
PDM	measurement interferometer photodiode
Δ_M	Modulation
Δ_F	Frequency

Table 4.1: Labeling of figure 4.3.

4.1.1 Stabilisation of frequency noise

Lasers are not perfectly stable in frequency (ν). Such frequency noise δf_0 couples directly into phase measurement variations $\delta\phi$:

$$\delta\phi = \frac{\Delta L}{c} \cdot \delta f_0 \tag{4.7}$$

with $\delta f_0 = 2\pi \cdot \delta\nu$. The frequency fluctuations can be reduced by means of an electronic feedback system. The correction signal for this feedback system is provided by a third interferometer. This is a frequency interferometer, also located on the ultra stable optical bench. The arm length difference of this interferometer is very large (Δ L $\gg 0$), so that an amplified signal $\delta\phi$ is generated, to be injected in the feedback electronics. In the case of the LTP OBI the arm length difference is designed to be 39 cm.

4.1.2 Contrast of the heterodyne signal

Figure 4.4 shows the schematic heterodyne signal measured with a photodiode. The contrast C is given by:

$$C = \frac{I_{max} - I_{min}}{I_{max} + I_{min}} \tag{4.8}$$

The value of C is between 0 and 1. The heterodyne signal can be described with the following equation:

$$I(\phi) = A\,(1 + C \cdot \cos(\phi)), \tag{4.9}$$

where A is the the amplitude of the signal at the photodiode and $\cos\phi$ is given by the equation (4.4).

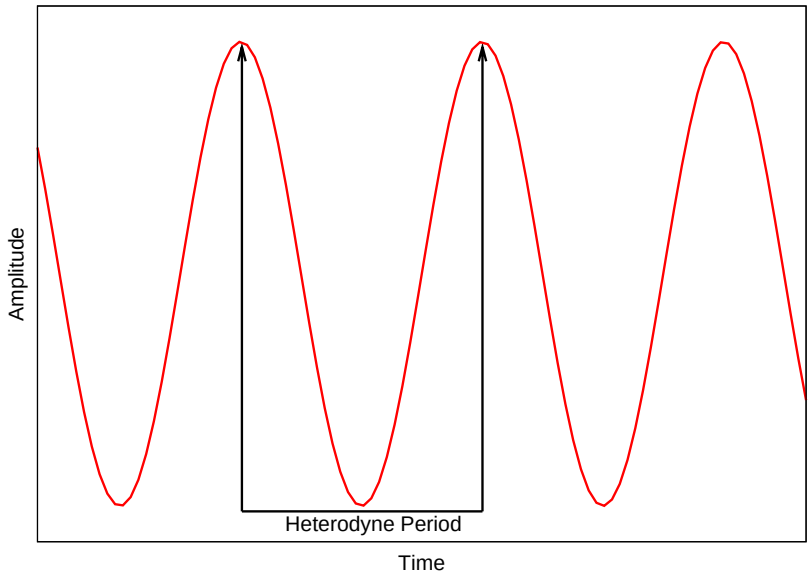

Figure 4.4: Heterodyne signal at a photodiode.

4.1.3 Relative wavefront quality

A CCD camera is used to measure the wavefront of the recombined beams. It is a Xeva camera manufactured by XenICs. The CCD material is Indium Gallium Arsenide (InGaAs) suitable for a wavelength range of 900 – 1700 nm.

The resolution is 320×356 with a pitch size of 30 microns. The camera is linked by a USB2.0 connection to a LINUX based computer running a programme developed by Felipe Guzman Cervantes (AEI Hannover) [32]. A reference photodiodes sensing the heterodyne signal generates timing signals to control the camera image acquisition. Figure 4.5 show a photograph of a relative wavefront quality measurement set-up. The measurement gives information of the relative beam match of superposed beams illustrated in figure 4.6.

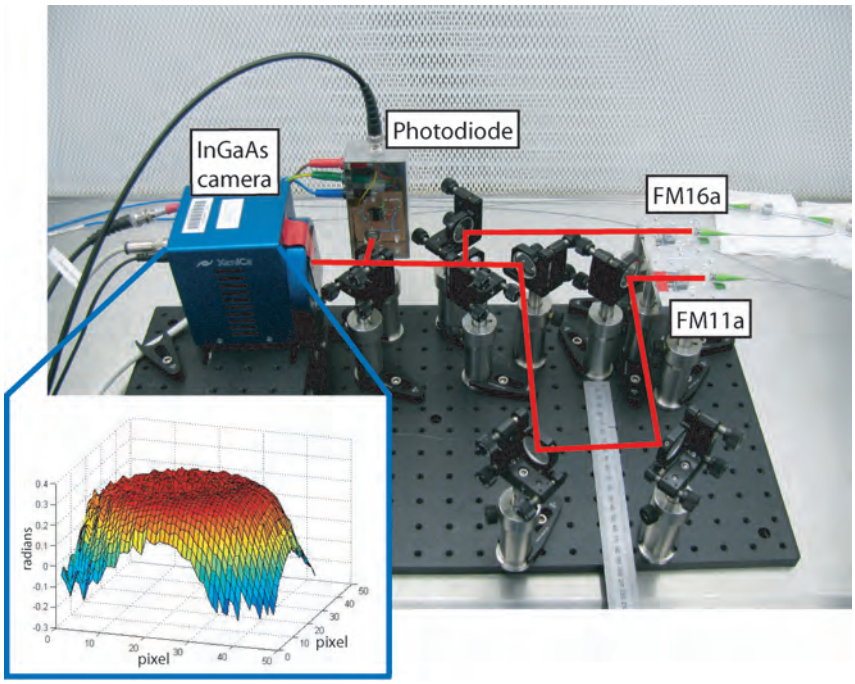

Figure 4.5: Photograph of a set-up for measuring the relative wavefront of combined beams. The InGaAs camera is at the left hand side of the picture (blue box); a neutral density filter is attached to prevent the CCD chip from overexposing and blooming effects.

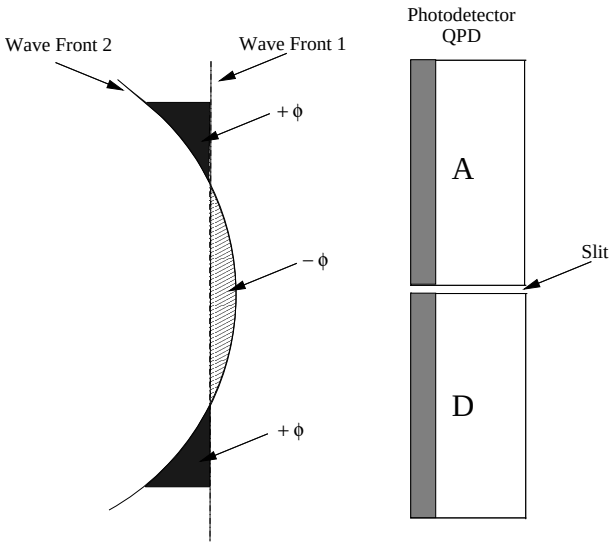

Figure 4.6: Overlapped wave fronts of interfering beams whose parameters are different. Inhomogeneous phase front [33]

4.2 LTP optical bench requirements

The optical requirements for the LTP OBI are given in the project requirements specification [30]. A summary of the thesis relevant requirements will be given in the following:

• LTP-PFM-OBI-3003: The OBI and its components should be able to withstand a radiation dose of up to 20 krad.

• LTP-PFM-OBI-3103: The FIOS should be bonded to the bench so that with the electrode housing optical windows in place the optical beam will hit the test masses at a height of 12.5 mm ± 25 μm above the polished surface of the OBI. The nominal height of the reflection point on the test masses is 12.5 mm above the surface of the OBI baseplate. The tilt of the optical window means that the beam on the bench has to be ~ 98 μm nearer the OBI.

• LTP-PFM-OBI-3201/3202: Fibre length is ~1.030 m. Each fibre will be within ± 5 mm of its nominal length.

• LTP-PFM-OBI-3205: Power transmission - The optical throughput of the fibre from input to the mating connector to power out of the FIOS should be >80 %.(Includes input loss at the DIAMOND connector, optical loss through the fibre and FIOS and loss due to polarisation imperfections.)

• LTP-PFM-OBI-3206: The minimum bend radius of the fibre should be 40 mm.

• LTP-PFM-OBI-3401: The contrast at the output of the Reference, X1, X2-X1, and frequency noise interferometers must be >80%.

• LTP-PFM-OBI-4102: The FIOS should be bonded to the bench so that the optical beam is parallel to the surface of the OBI, with an allowable variation of ± 30 μrad.

• LTP-PFM-OBI-4201: The FIOS output beam ellipticity should have a ratio of minor to major axes of >0.85.

• LTP-PFM-OBI-4202: The beam radius should be between 500 and 650 microns from each FIOS to all measurement photodiodes.

• LTP-PFM-OBI-4204: Matching of beam sizes from FIOS1 and FIOS2 should be such that the ratio of beam sizes is <1.2 at the X1-X2, X1 and reference photodiodes.

• LTP-PFM-OBI-4205: Matching of beam curvatures from FIOS1 and FIOS2 should be such that the absolute value of the difference in reciprocals of beam radii is <0.32 at the X1-X2, X1 and reference photodiodes i.e. 1/R1-1/R2 < 0.32 m^{-1}.

• LTP-PFM-OBI-4209: The output of each FIOS should be linearly polarised with the angle of polarisation perpendicular to the top surface of the OBI to within ± 3.5 degrees.

4.3 Material requirements

The requirements of the material of an ultra-stable bench for use aboard LTP are: a low thermal expansion coefficient, radiation hardness, a low out-gassing rate and non-magnetic property. Thermal expansion on the optical bench has to be minimised in order that the read-out is sensitive to the required displacement measurement. The materials used have to be radiation hard so that cosmic rays do not influence optical component properties e.g. beamsplitter transmission. Due to cleanliness and contamination issues a low out-gassing rate is required. To protect the test masses from external forces non-magnetic materials are used.

Mirrors and beamsplitters on top of the ultra-stable optical bench form the interferometers (further detail in section 4.4) and are individually attached to the Zerodur baseplate using a technique called silicate bonding (see section B.1). This technique is highly suitable for space applications since it provides strong and stable bonds. Other non critical optics (the PBS and the lens inside its U-groove carrier) are epoxy glued. The mirrors and beamsplitters are made of high grade fused silica (LTP-PFM-OBI-4303 [30]). Fused silica has a low

thermal expansion coefficient ($0.5 \times 10^{-6}/°C$) and is radiation hard to cosmic rays. Zerodur is a glass ceramic with a very low thermal expansion coefficient ($0.05 \times 10^{-6}/°C$) (LTP-PFM-OBI-3301 [30]). The coatings of the optical components were subject to space qualification by irradiation tests (see chapter 2 and chapter 3). The designed fibre injector (see chapter 5) consists of known and suitable materials such as fused silica, PEEK tubing with a low out-gassing rate and thermal expansion rate, and titanium strain relief. The lens to collimate the beam is made out of a Corning glass (ECO-500). Due to the unknown properties of this material, the lenses have been subject to irradiation tests. This was also done for the optical windows which are made out of a certain kind of glass and are located in the vacuum tanks as transmitted optics. The window material was specially selected to minimise main noise sources e.g. thermal variation of optical pathlength and stress-induced change in refractive index and optical pathlength [34].

4.4 OptoCAD simulated layout

This section is intended to give an understanding of the simulation of the interferometer layout for LISA Pathfinder. The simulation was done using a program called OptoCad. OptoCad is a Fortran 95 program written by Roland Schilling to trace Gaussian beams through an optical set-up in two dimensions. OptoCAD simulates the beam starting at a defined point and tracks reflection and transmission by different optical components. In the LTP case it simulates the properties of the fibre injector by passing an input beam of a certain diameter through a lens at a certain distance. It then calculates the propagation on the remainder of the optical bench and provides information on the beam properties such as beam diameter, waist, and curvature as well as information on the position of the beam in given origin hitting defined components.

In total there are four interferometers as shown in figure 4.7. Beam1 coming from FIOS1 is indicated in red. Beam2 coming from FIOS2 is indicated in blue. Beam2 stays on the optical bench where as beam1 leaves the optical bench and gets reflected by the test masses. The mirrors (M) and beamsplitters (BS) are numbered and labelled. In total 22 mirrors and beamsplitters are located on the bench. The test masses are shown in figure 4.7 as yellow squares. The electrode housing around the test masses is also indicated with a hole of 6 mm. The optical windows where the light passes through to enter the vacuum cans (not shown in figure) which house the test masses are not part of the OBI, but as the beams are transmitted by these optics they do affect their phases. These effects must be considered during the OBI layout and construction process and therefore were also investigated further. The optical windows are labelled 'WIN1' and 'WIN2'. The photodiodes, shown in black, were the responsibility of the University of Birmingham and are not further discussed within this thesis.

As mentioned four heterodyne interferometers are used so that the test mass

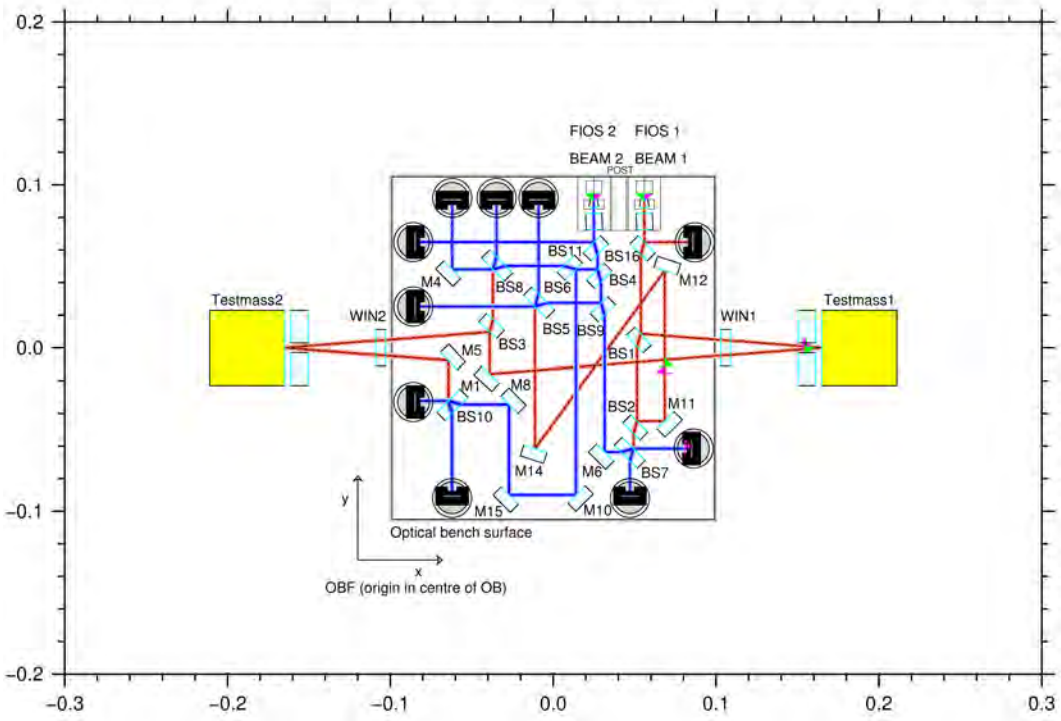

Figure 4.7: OptoCAD simulation of the OBI. The axes are labelled in meters for all OptoCAD simulations.

movements can be tracked over several wavelengths. The constant pathlength difference in the interferometers on the optical bench is compensated by a length difference of 36 cm of the feed-in fibres before the optical bench.

The reference interferometer, shown in figure 4.8, provides the reference output phase ϕ_R for the other interferometers. The frequency interferometer, shown in figure 4.9, has a stable pathlength difference of ~ 38.4 cm. The first measurement interferometer is the so-called X1 interferometer, shown in figure 4.10. It measures the pathlength variations of test mass 1 with respect to the optical bench. The other measurement interferometer is the so-called X1-X2 interferometer, shown in figure 4.11. It measures the pathlength variation between test masses 1 (TM1) and test mass 2 (TM2).

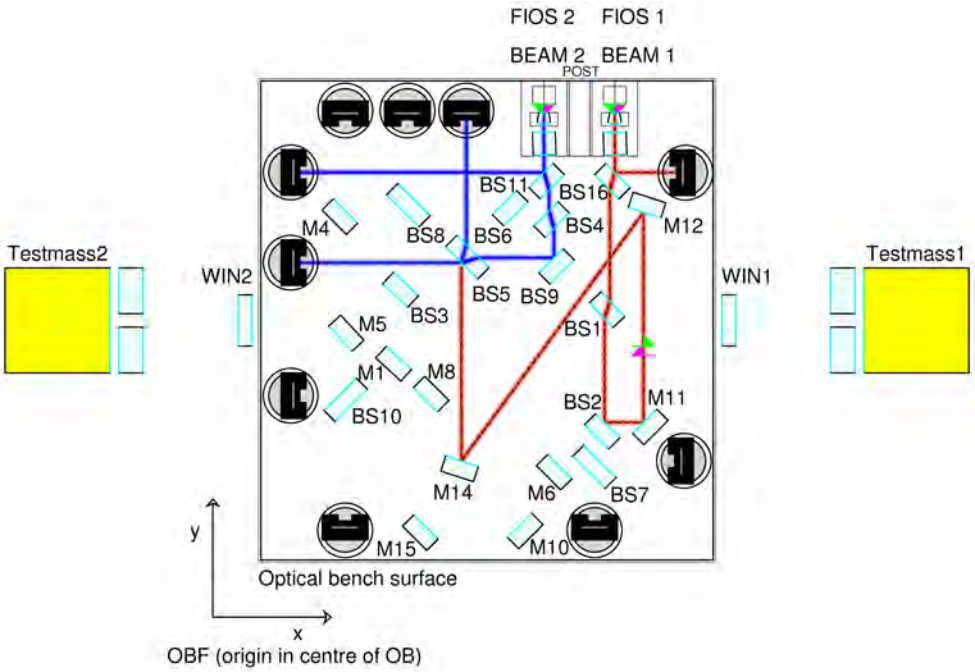

Figure 4.8: OptoCAD simulation of the reference interferometer.

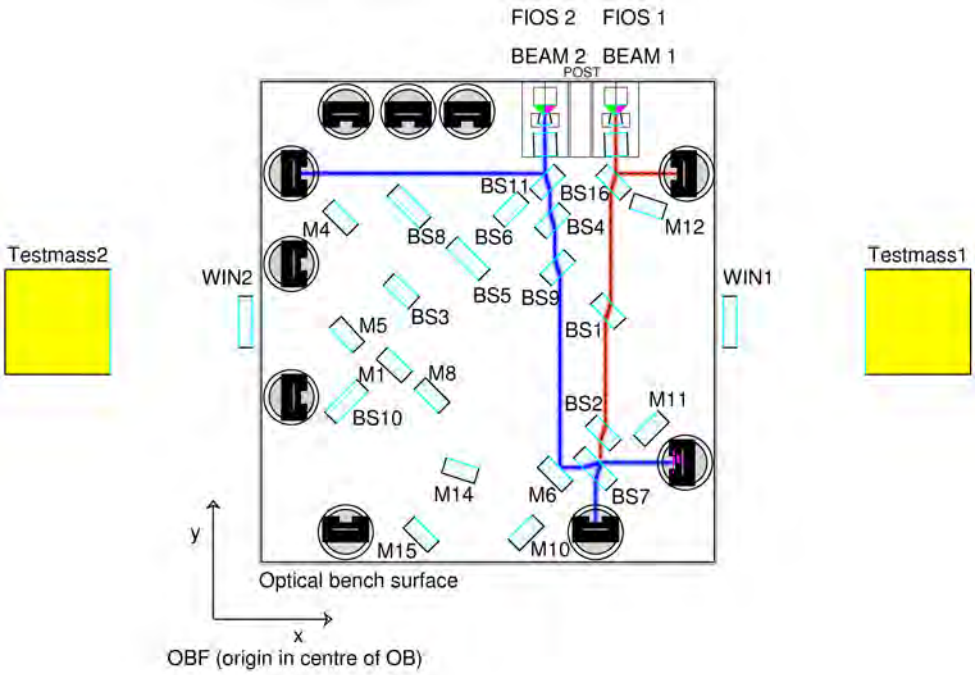

Figure 4.9: OptoCAD simulation of the frequency interferometer.

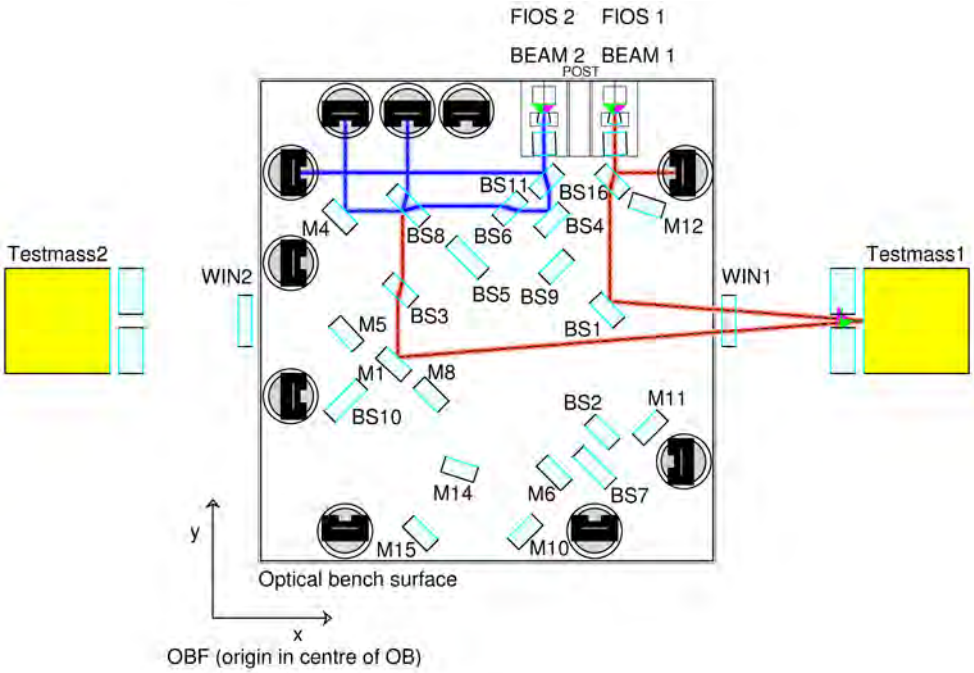

Figure 4.10: OptoCAD simulation of the X1 interferometer.

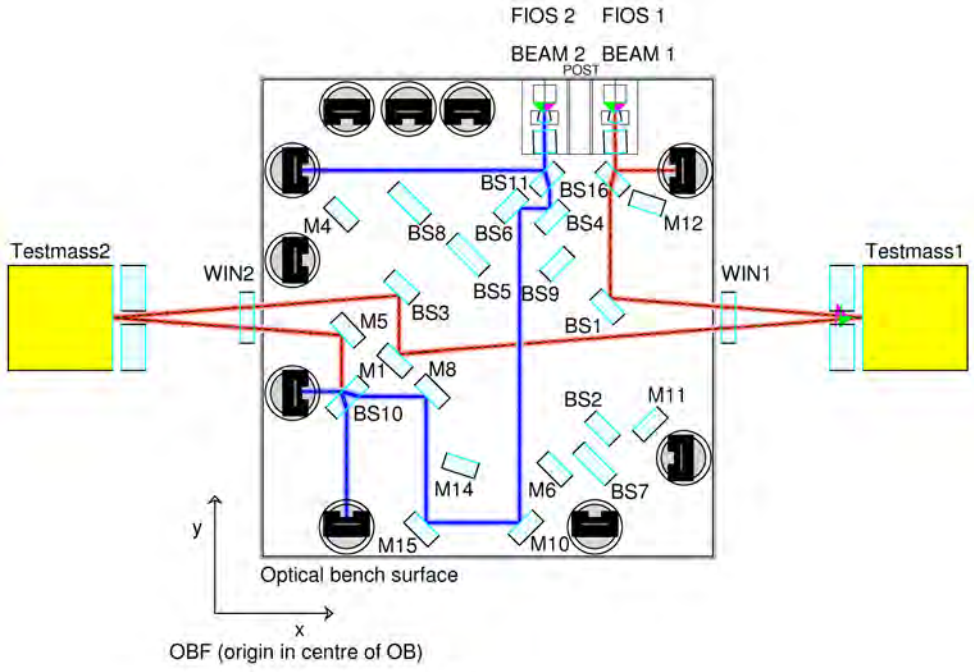

Figure 4.11: OptoCAD simulation of the X1-X2 interferometer.

The OBI provides the ability to monitor the displacement of two drag-free test masses along the x-axis with picometer accuracy over several wavelengths. Besides monitoring the movement of the test masses it also provides an alignment sensor – the differential wavefront sensing (DWS). The technique of the DWS is described in [35].

Both fibre injectors are designed such that the best match of beam size and curvature is at the X1-X2 interferometer. Due to the different pathlengths on the optical bench both fibres injector are individually designed. Beam1 has a maximum pathlength of 765.41 mm and beam2 of 406.58 mm. For this purpose the distance of the lens from the beam output is simulated such that the beam radius is between 500 μm and 650 μm at all measurement photodiodes. Using OptoCAD the ideal distance of the lens from the fibre output was 3.40 mm for FIOS1, which results in a beam diameter of 1058.4 μm at 5 cm and 1241 μm at 70 cm distance measured from the back of the fibre mounting structure. In the case of FIOS2 the ideal distance is 3.38 mm, which provides a beam diameter of 1074.8 μm at 5 cm and 1524.4 μm at 70 cm.

The chosen Geltech moulded glass aspheric lens is selected due to its optical properties. The focal length of the lens is 6.24 mm with a numerical aperture of 0.40. The material is a corning lead free glass (ECO550). This lens is standardly used for commercial fibre couplers at 1064 nm wavelength providing a beam diameter of ~1 mm.

4.5 High precision alignment

The requirement of the LTP project are very tightly defined: to minimise the coupling of the test mass rotation noise to the test mass longitudinal read-out, the beam of the X1 and X1-X2 interferometer is required to hit the test masses accurately in the middle of the front face with an maximum error of $\pm 25\,\mu$m. The optical contrast at the output of the reference, frequency, X1, and X1 - X2 interferometers must be $> 80\,\%$. To fulfil this some components of the optical bench must be placed with high precision e.g. the angle alignment of BS1 has to be within $50\,\mu$rad [36]. Other optical components can be placed within $\pm 50\,\mu$m. With the aid of the OptoCAD simulation each optical component position is defined. By transforming the OptoCAD component data into Solidworks layout, the templates for the optical components are constructed. For critical components OptoCAD provides nominal reflection points of the beams. These refection points can be extrapolated to lines in the Cartesian coordinate system of the OBF (Optical Bench interferometer reference Frame) such that picking any two points on that line defines the nominal beam direction. Template and precision alignment techniques are explained in further detail in following sections.

4.5.1 Brass templates

The templates having pockets - cut outs. One template, shown in figure 4.12, defines the position of the post. The post is the mounting structure for the fibre injectors on the bench (see chapter 5). A pocket is designed to house three ball bearings which are defining the location of the optical component; two ball bearings are located at the long side and one at the narrow side of the component. The template gets aligned using a Coordinate Measuring Machine

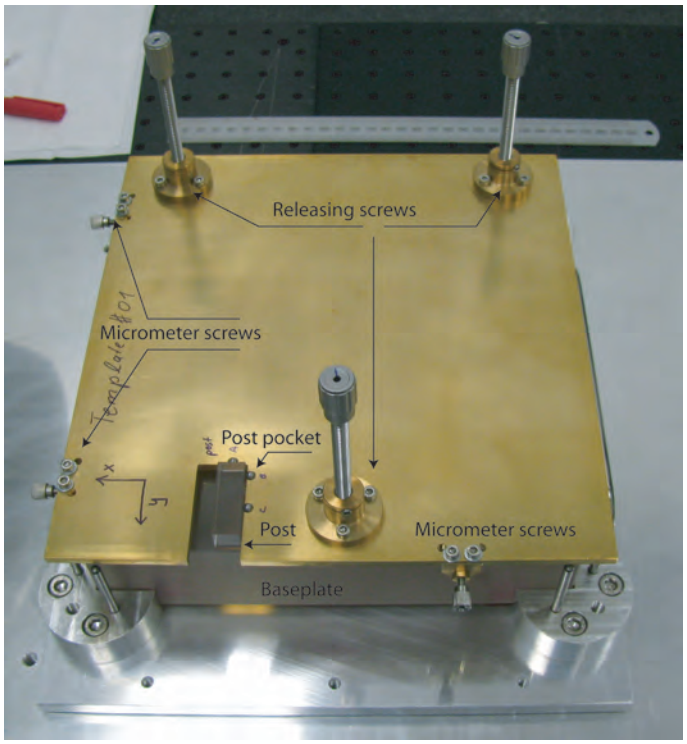

Figure 4.12: Template for post bond.

(CMM). The positions of the ball bearings with respect to the optical bench are measured. Along two sides of the templates micrometer adjustors are attached. They keep the template in position by touching the side of the Zerodur optical bench (shown in figure 4.12). Using the micrometer adjustable screws the template position can be manipulated. This measurement and adjustment is repeated until the required position of the template is found. In the case that a template defines locations for more than one optical component pocket, two ball bearings with the furthest distance to each other are measured for the alignment procedure. In the case of the template for the so-called"post bond" only one pocket for the post exists and the template can be aligned within the CMM uncertainties of few microns. If the template has several pockets the component position uncertainties depend also on the relative accuracy of the machined pockets; this is around 50 microns. In total seven templates were

manufactured for 14 components whose absolute position is not critical. After a bonding stage the template is moved away from the component carefully; the template is moved sidewards and then screwed above the level of the freshly bonded component using three releasing screws which are attached to the top of the template before it is lifted up. This process minimises the risk of damaging bonded components during template removal.

4.5.2 Calibrated quadrant photodiode pair

For bonding alignment of critical components a calibrated quadrant photodiode (CQP) pair is used. The CQP device is shown in figure 4.13. It consists of two quadrant photodiodes which are mounted into an $190 \times 100\,\mathrm{mm}$ Invar structure, a metal alloy which has a low thermal expansion coefficient of $1.3 \times 10^{-6}\,^{\circ}\mathrm{C}$ at $93.33\,^{\circ}\mathrm{C}$. The incoming beam is split into two beams by a 50:50 beamsplitter; the first quadrant photodiode has a pathlength of ~ 2 cm measured from the beamsplitter, the second beam has a pathlength of $\sim 48\,\mathrm{cm}$. Thus simultaneously centering the beam on both quadrant photodiodes defines a unique beam position and propagation direction with respect to the Invar structure. If the offset between the centred optical beam and the Invar structure is known then one can use a physical measurement of the Invar structure to determine the beam's position and direction. These offsets are obtained by calibrating the CQP. Once calibrated, the CQP can be used in one of two ways. The first is to align it onto a pre-existing beam. Measurement of the CQP position can then give the beam's position and direction. The second use of the CQP is as a calibrated target: placing the CQP at a particular point and orientation given by an OptoCAD modelled beam vector allows aligning a component by steering the beam following it onto the target, so that the beam is centered on both photodiodes.

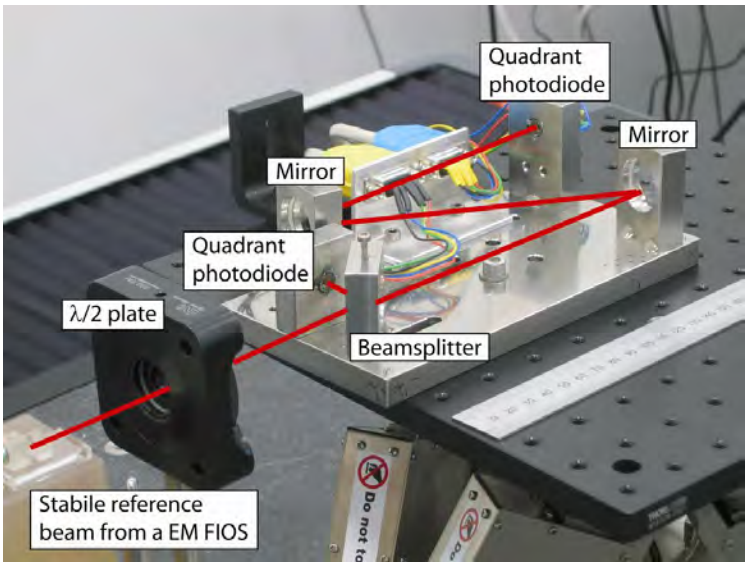

Figure 4.13: Picture of the calibrated quadrant photodiode device.

The signals from each quadrant of each photodiode are amplified, digitised, and taken into a computer running a program written in LabVIEW. This allows the x and y position of the beam on each photodiode to be calculated and displayed. The total power is also displayed. The readout can use either DC light or amplitude modulated (AM) light. For DC light the total light power for each quadrant is used to calculate the beam position on that photodiode. For the AM light it is the amplitude of the modulated signal on each quadrant that is used. The DC and AM modes have virtually identical sensitivity to beam movement, with beam movements of $< 1\,\mu$m being easily observable. The advantage of the AM mode is that it is much less susceptible to noise sources such as changes in background light levels or offset drifts in the electronics. AM is therefore the standard operating mode. A screenshot of the program display is shown in figure 4.14. The program provides a read-out of the power on the QPD. The position of both beams are displayed. The sensitivity of these displayed can be changed and the x and y position of the beam is given. The display can be scaled to read out the beam displacement in μm. To do

this the CQP is mounted on a precision actuator (hexapod), aligned to the beam, and then displaced by known amounts (typically 100 μm) in x and y direction.

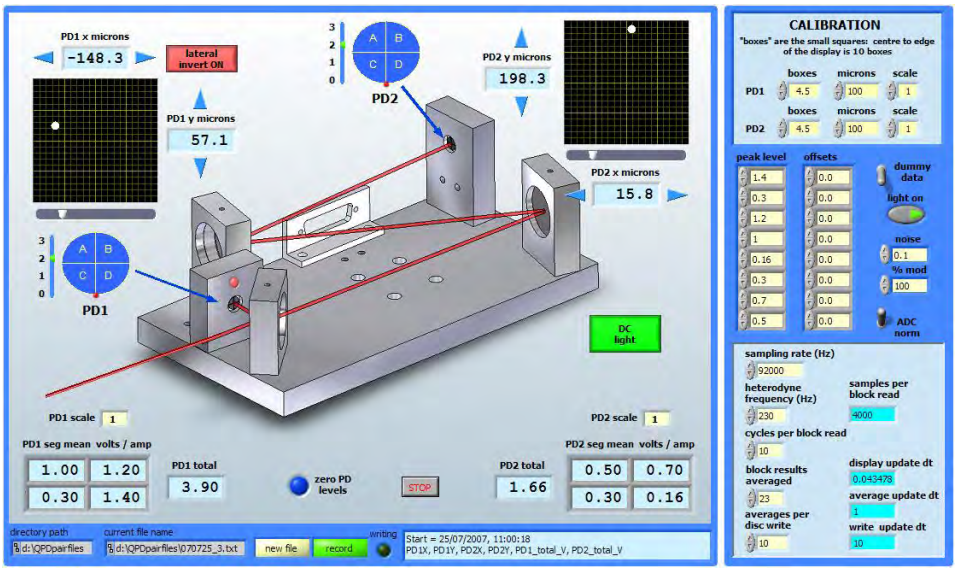

Figure 4.14: Screen dump of LabView programme.

Measurement of the CQP position is done using a CMM. This can measure the position of the Invar baseplate with a precision of 1 - 2 μm. However this does not directly give the optical beam position and direction. To obtain this the CQP must first be calibrated.

It is easiest to describe the CQP calibration procedure using a 2D example shown in figure 4.15. To calibrate the CQP a very stable reference beam but unknown in position and direction is needed. For this purpose a stable monolithic fibre injector (LTP FIOS prototype design) was epoxy bonded onto a stable slab of Zerodur.

The following 2D example is presented only for explanation and was not the actual calibration routine: *The CQP was aligned to this beam and its position was measured using the CMM (Measurement 1). Then the CQP was moved along the beam, re-centred to the beam, and again the position of the Invar*

baseplate (Measurement 2) was measured. These two measurements already provide information on the beam direction, but not of its offset from the Invar baseplate. The CQP was then turned over and again aligned to the beam and its position (Measurement 3) was measured, this was repeated once more (Measurement 4). The blue dots represent the positions of the quadrant photodiodes (shown for simplification in a straight line as centred on the optical beam) and the red dots represent the measured position of the CQP reference point.

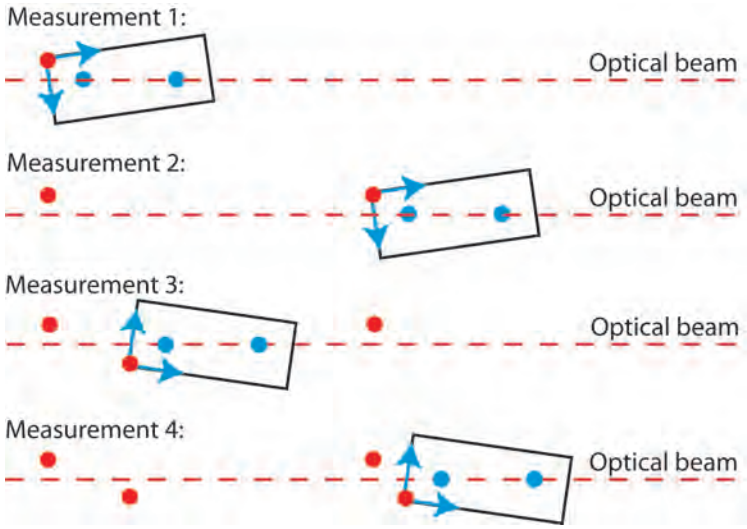

Figure 4.15: 2D - schematic drawing of the routine of the CQP calibration.

The optical beam must then be the mid line between these measured points. In such a way both the direction and offset of the beam relative to the baseplate was defined. In practice several extra measurements were carried out to over-constrain the CQP calibration. The calibration can then be made by a best fit to all the measurement points. The extra points also allows a consistency check on the calibration. The obtained calibration numbers are used to calculate the expected beam parameters for each measurement and compare these with the parameters of the fitted beam. These residual errors give a measure of the uncertainties in the CQP calibration.

In practice the CQP is a 3D object, requiring a slightly more complicated procedure. The main differences are that the CQP must be measured in at least 3 orientations (rolled about the beam axis) and that the reference points on the CQP baseplate will lie on a cylinder around the beam axis, rather than on two straight lines parallel to the beam axis. Once again a best fit to all the measurement points was used to obtain the dimensions of the cylinder. An example plot of such a calibration is shown in figure 4.16.

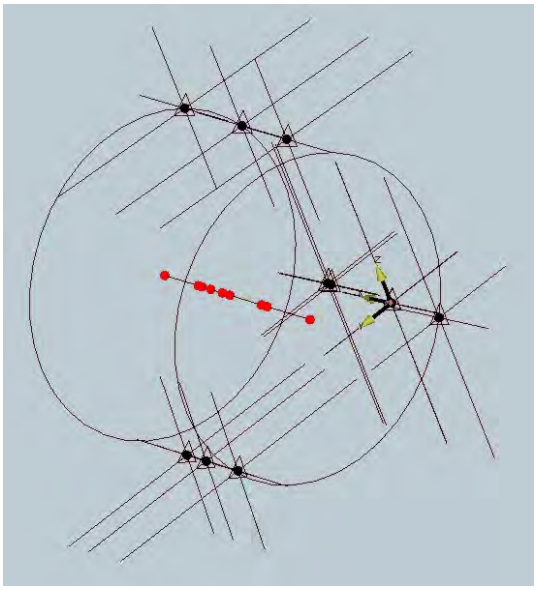

Figure 4.16: Measurement drawing of CQP calibration in 3D.

The black dots in the triangles are the measurements of the CQP reference points. The cylinder is a best fit to these measurement points and is used to generate the CQP calibration numbers. The calibration numbers are then used for each measurement to generate the beam position (the red dots), and the differences between these measurements and the cylinder axis plotted to get a measure of the error in the calibration. As with the 2D example, the residual errors can be calculated between each individual measurement and provides the overall best fit to get an idea of the accuracy of the calibration.

It is possible to perform a quick check of the calibration without going through the full calibration performance. This consists of taking two measurements, ideally $\sim 20\,\mathrm{cm}$ apart on a single stable beam. Each measurement uses the CQP calibration numbers to produce a beam position and direction. These two measurements of the same beam should produce consistent numbers for the two beams. Any lack of consistency points to a problem in the measurement or CQP calibration that should be investigated before further measurements are taken.

The CQP is calibrated as a target device with a residual uncertainty of $\sim \pm 2.5\,\mu\mathrm{m}$ in position and $\sim \pm 20\,\mu\mathrm{rad}$ in angle. As such the CQP can be used very accurately as a beam vector measuring device and as a beam target device. To steer a beam the component has to be placed in a stable and reproducible way. This will be explained in following section.

4.5.3 Actuator alignment bonding

Components which have to steer the beam to a particular point are placed using adjustable actuators. Examples are the fibre injectors and the components which are reflecting the beam towards the test masses. In the case of the fibre injectors the correct height and angle of the outgoing beams are important since misalignment errors are not correctable at a later stage. In the case of the beamsplitters BS1 and BS3, shown in figure 4.7, the positions of the components have to be aligned so that the beam hits the test masses in their centres with an uncertainty of $\pm 25\,\mu\mathrm{m}$. Components which are recombining two beams also have to be bonded with precision alignment.

Figure 4.17 show the precision actuators in a test set-up. The position of the component is defined using three ball bearings. One ball bearing is placed at the narrow side of the component. This ball bearing defines the lateral position

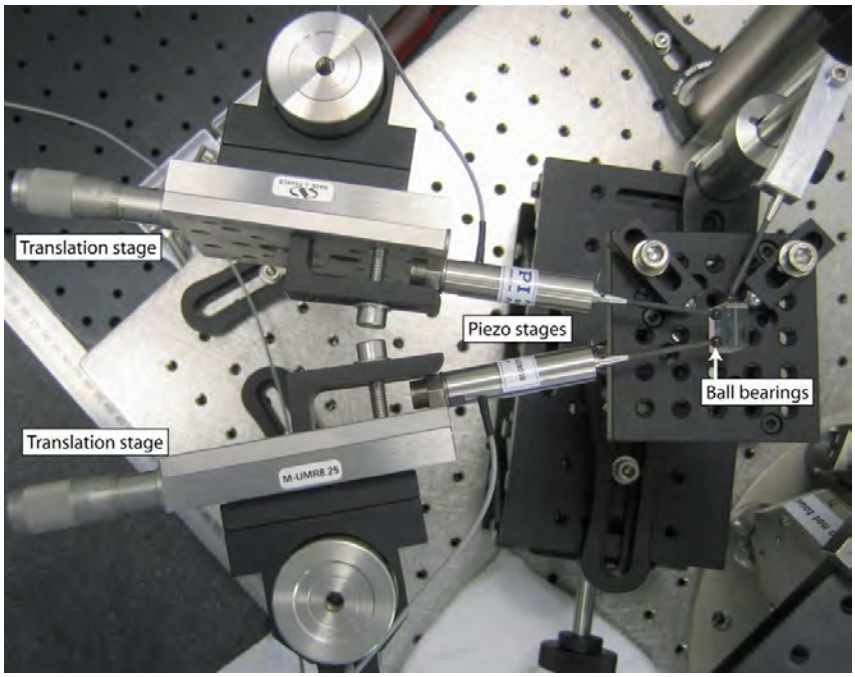

Figure 4.17: Photograph of experimental performance tests of actuators.

of the component and is aligned such that the incoming beam hits the middle of the mirror surface and in the case of a beamsplitter such that the beam travels centred through the component. The position of this ball bearing is less critical and does not influence the component alignment itself. The component alignment is given by the position of two ball bearings positioned at the long side of the component. These two ball bearings are attached to precision actuators. The actuator consists of a sub-micron-precision piezo stage which is attached to a micrometer translation stage to provide the required travel range of the actuator. The correct position of these actuators is found in several alignment steps. Along the OptoCAD modelled beam vector the CQP is placed as a target device. Furthermore the OptoCAD model provides the position of the component and so the actuators can be placed roughly at the correct point. The CMM measures the position of the ball bearings in relation to the location of the optical bench so that the location of the actuator can be

controlled. The component is placed against the ball bearings of the actuators. To avoid optical contacting of the components octane as a buffer solution is used. The component is then aligned by manipulating the actuators. When the beam is centered onto both photodiodes of the CQP the correct position has been found. This position is verified by locating the component several times against the ball bearings and reproducing the centering of the beam on the CQP. Finally the component is bonded at this position. After bonding the component the actuators are removed and the reflected, and in the case of a beamsplitter also the transmitted, beam vector is measured using the CQP. These measurements are used to feed-back into the OptoCAD simulation for alignment of subsequent optical components.

Chapter 5

LTP fibre injector

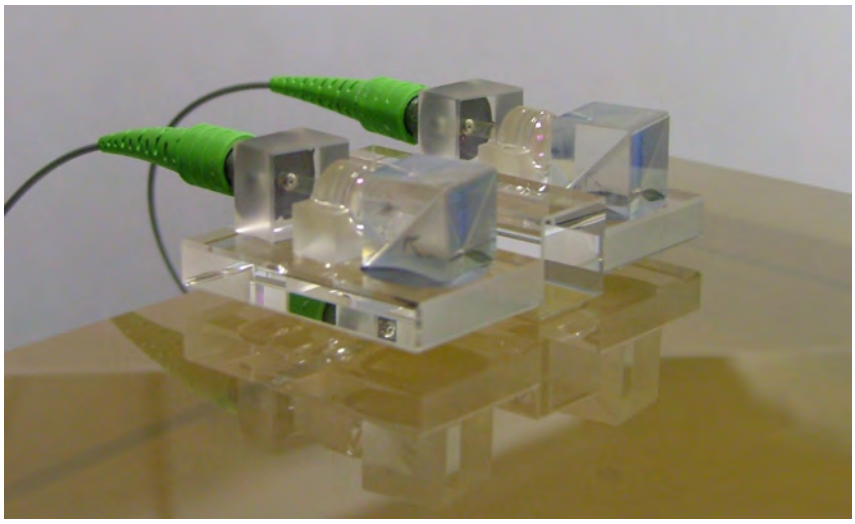

Figure 5.1: Photograph of the fibre injector qualification model pair bonded onto the post on the prototype LTP optical bench.

This chapter presents the design, construction, and the qualification process of the LTP fibre injector design, shown in figure 5.1. Results of the fibre injector precision alignment on the optical LTP prototype bench are also provided.

5.1 Fibre Injector design

This section describes the design and implementation of the customised ultra-stable fibre injectors. The fibre injector consists of glass components which are either glued or silicate bonded together and an optical fibre which includes strain relief cladding. Suitable commercial fibre injectors were not immediately available and would require further development to fulfil the challenging requirements for LTP fibre injectors in terms of alignment, non-magnetic material and stability. The optical beam height of the OBI is required to be 12.4 mm and it has to be parallel to the surface of the OBI, with an allowable variation of $\pm 30\,\mu$rad.

The designed fibre injector optical subassembly (FIOS) consists of a stripped fibre held in a holed cuboid including strain relief, a lens mounted in a close-fit U-groove and a polariser; all parts are attached to a FIOS baseplate as shown in figure 5.2.

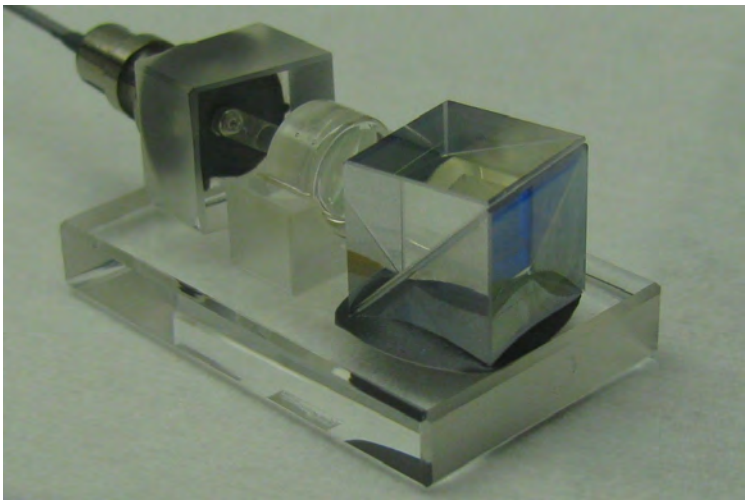

Figure 5.2: Photograph of a FIOS qualification model.

5.1.1 Fibre mounted assembly

The supplied Fujikura Panda optical fibre from Diamond SA has two flight qualified fibre connectors and consists of a polarisation maintaining single mode fibre. It has a softer acrylate polymer cladding shield and a very stiff PEEK protective tubing. The fibre is cut into two parts and the cleaved fibre end is used to construct a LTP fibre injector. To produce a stable and rigid mounting structure a fibre end mounting design was developed as shown in figure 5.3.

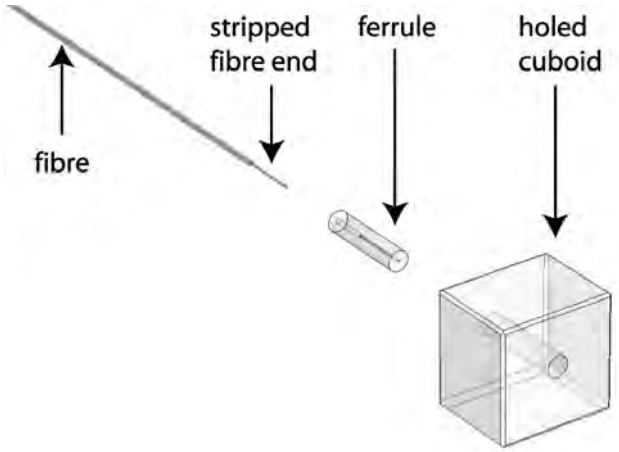

Figure 5.3: Exploded diagram of fibre mounting assembly (without strain relief).

The stripped fibre end is glued inside a close-fit ferrule to increase its diameter and to stabilise it. The ferrule including the fibre end is glued inside a close-fit holed cuboid with s-polarisation orientation towards the $\lambda/10$ polished bottom. This holed cuboid provides a suitable beam pointing and a suitable mount for the fibre end which can be silicate bonded to the FIOS baseplate. This cuboid assembly is called the FMA (Fibre Mounted Assembly). The optical output surface of the FMA is polished to $\lambda/10$ to provide a good quality beam. This is done at an angle of eight degrees to the beam axis to prevent

back-reflections propagating inside the fibre towards the laser. Furthermore, strain relief structure is applied around the fibre end on the back of the FMA to protect the fibre from damage as shown in figure 5.4. A titanium strain relief is glued to the back of the FMA and the PEEK of the fibre. Special care has to be taken that the fibre inner part is not glued to the titanium strain relief, that could cause polarisation errors due to applied mechanical stress. A (green) hytrel boot is placed over the titanium and part of the fibre to prevent damage due to bending the fibre too tightly.

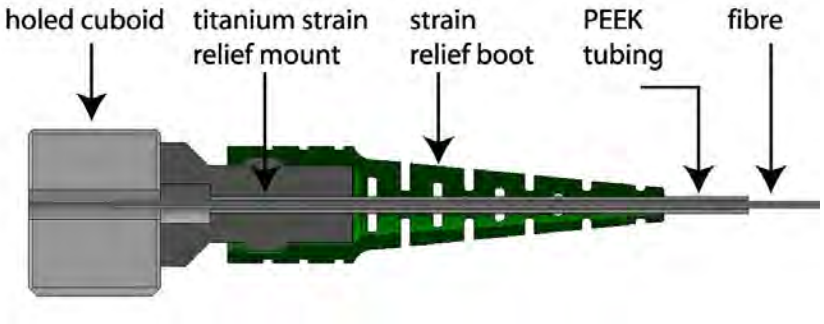

Figure 5.4: CAD model of the fibre mounted assembly.

To mount the fibre in the ferrule the fibre end was specially prepared. The Peek tubing was removed from the fibre end using a mechanical stripper. The remaining inner part of the fibre was separated from the cladding shield. The cladding material has to be removed in such a way that only the undamaged inner core of the fibre consisting of the two indexes of glass remains. Different methods to do this have been tested and are presented in more detail.

One of the techniques was to etch the cladding with sulphuric acid. A concentrated sulphuric acid solution was heated up to 190°C. Then the fibre end was dipped in it for a duration of ~20 s. The fibre cladding blackened and thinned. The final result was checked with an optical microscope (digital Nikon SMZ1000) and a picture is shown in figure 5.5. It can be seen that the

remaining cladding is damaged by the acid and that there is some residue on the core. It was not possible to obtain a sharp boundary between the stripped section and the remaining cladding without damaging the fiber core. From this point of view this stripping method was unsatisfactory for our purpose.

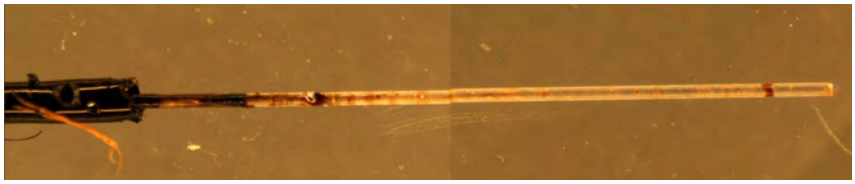

Figure 5.5: Fibre end with removed cladding using sulphuric acid; core diameter 125 μm and cladding 400 μm.

Figure 5.6 shows a fibre stripped using a dichloromethane solution. The technique works as follows. The fibre end is immersed in the solution for a duration of two hours. Then the cladding is very easily mechanically removed (by hand using a clean room cloth). The result is a clear stripped fibre without any residue. This method is very reliable, but it caused the same problem of uncontrolled weakening of the remanning cladding with a large uncertainty of stripped fibre length.

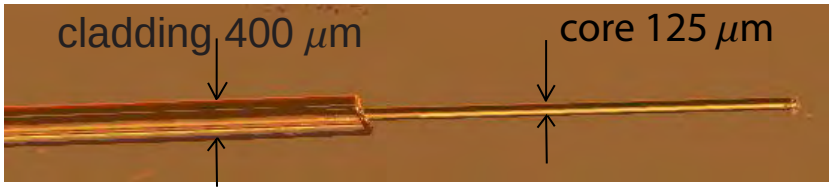

Figure 5.6: Fibre end with removed cladding using dichloromethane; core diameter 125 μm and cladding 400 μm.

Different mechanical stripping tools have also been tested. The stripped fibre was inspected using a microscope, as shown in figure 5.7. The No – Nik fibre optic stripper with a stripping diameter of 152 μm was found suitable for our application. The stripping of a fibre mechanically can be done to millimeter precision and has the advantage that no weakened cladding material remains. The mechanical stripper scores through the cladding without touching or nicking the fibre core. The cladding is then pulled by hand from the fibre core. Several tests proved that this can be achieved within given fibre length tolerances of $\pm$ 5 mm and without damaging the fibre core.

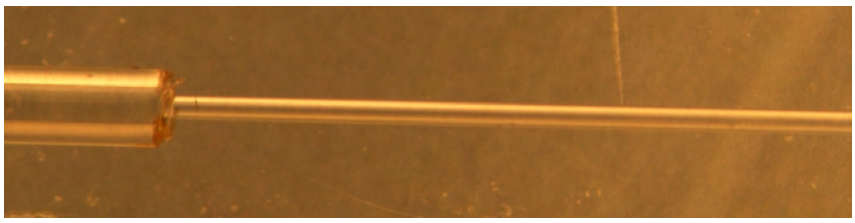

Figure 5.7: Fibre end with removed mechanically; core diameter 125 μm and cladding 400 μm.

The bonded FIOS QM pair was visually inspected for damage of the fibre in the FMA as part of the fibre injector investigation . The ground top surface of the FMA mounting block was wetted with octane to allow several minutes of observation. Figure 5.8 and figure 5.9 show a microscope picture of the FMA of FIOS1 and FIOS2. On the left hand side the fibre input is present, marked as FMA back, on the right hand side the polished front surface, marked as FMA face. The stripped fibre is threaded into a close fit ferrule, which is placed in the close fit hole of the mounting cube. Up to the cone of the ferrule the fibre cladding remains, but one can see the fibre cladding is slightly damaged at the end. No fibre core damage is observed. The pictures were taken after environmental vibration and shock tests and thermal-vacuum tests. The

pictures show no different features to other investigated FMA which have not been environmentally tested.

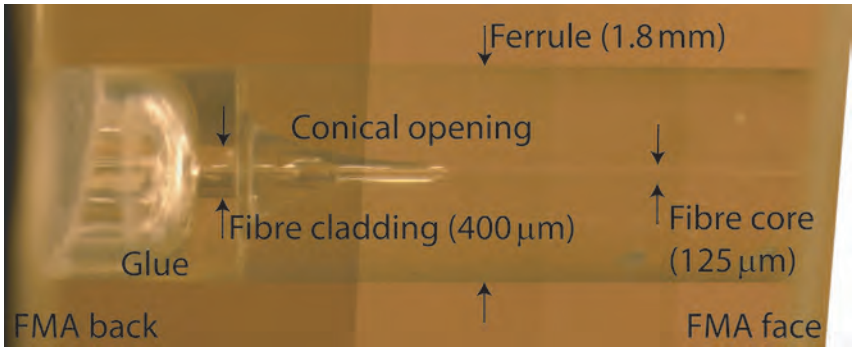

Figure 5.8: Microscope picture of FIOS1 QM inside the FMA cube.

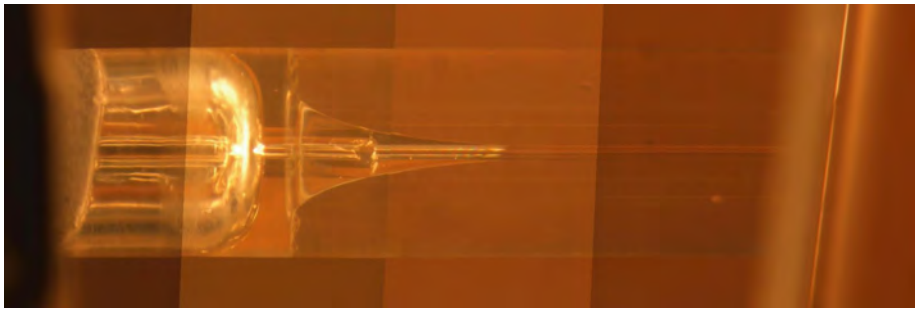

Figure 5.9: Microscope picture of FIOS2 QM inside the FMA cube.

5.1.2 Lens alignment

The used lens is a biconvex aspheric lens. A precision made U-groove is used to mount the lens in such a way as to align the lens centre with the beam from the fibre end and also to provide a flat surface to bond to the FIOS baseplate. The lens and U-groove are cleaned with acetone and the lens is glued into the U-groove using an epoxy glue called EpoTek 301-2. The assembly is cured at room temperature and heated to 40°C to reach full strength. The fibre mounted assembly and the fused silica U-groove holding the lens are silicate bonded onto the fused silica FIOS baseplate. The fibre mounted assembly is positioned using a template whereas the lens is precision manipulated while beam parameters are monitored. This manipulation is shown in figure 5.10. A CCD camera is used to monitor the beam during alignment. The distance of the lens to the fibre output defines the beam parameters. The nominal beam parameters are calculated using OptoCad, which also provides a theoretical calculation of the lens distance.

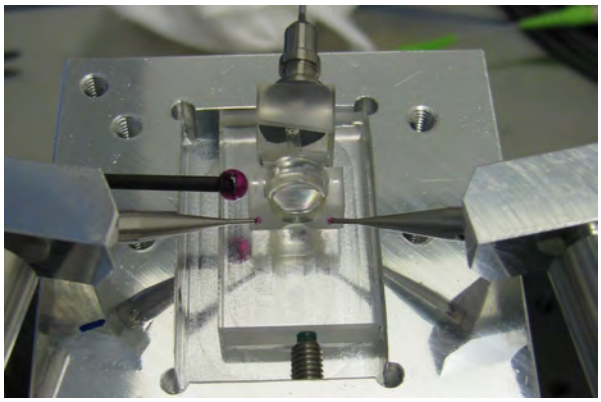

Figure 5.10: Photograph of the U-groove with lens inside the jig during the bonding step.

The nominal distance of the lens from the FMA beam output face is in the case of FIOS1 3.40 mm and of FIOS2 3.38 mm. Due to the pathlength dif-

ference on the LTP OBI, both FIOS have individual beam parameters. The beam modes are optimised for the recombination at the X1-X2 interferometer. During the construction of the Proto-Flight Model (PFM) FIOS1 it appeared that the U-groove of the lens had not silicate bonded over the entire bonding surface. A symmetrical dry area was left in the centre of the bond, as shown in figure 5.11. This was discovered after the FIOS was removed from its jig after the bonding step. Due to the jig, the bonding quality could not be investigated earlier. This was the first occasion in which a dry area was observed, so further investigation was necessary. Due to the shape of the dry area, a dirt particle or contamination is unlikely to be the cause. The fringe patten of e.g. a dirt particle looks circular. Therefore the flatness of the bonding surface of similarly glued lenses to U-grooves was investigated using a Zygo laser Fizeau interferometer to measure the flatness of bonding surfaces.

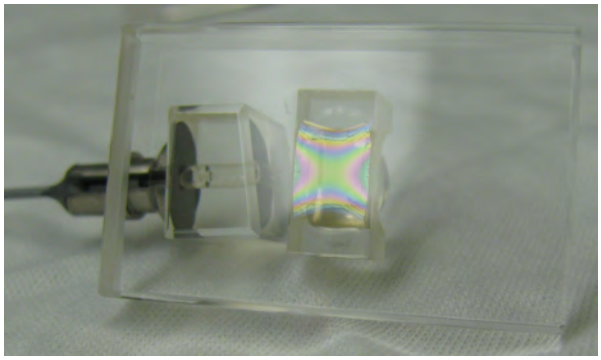

Figure 5.11: Photograph of the lens U-groove bond of PFM FIOS1.

The Zygo measurement analysis uses the metrology program called MetroPro. Figure 5.12 shows a screen shot; the top left window shows the flatness of the bonding surface including a colour scheme, the right top window shows the same information in 3 D. The bottom left window provides a scan over the surface following the marked line in the window above. The bottom right window shows the fringe pattern during the measurement. The measured values

are given in the field in the middle of the left hand side. One U-groove without a glued lens and five U-grooves with glued lenses were measured. Two different kinds of deformation of the bonding surface were observed. Due to the shape of deformation they were named valley-deformation (figure 5.13) and saddle-deformation (figure 5.14).

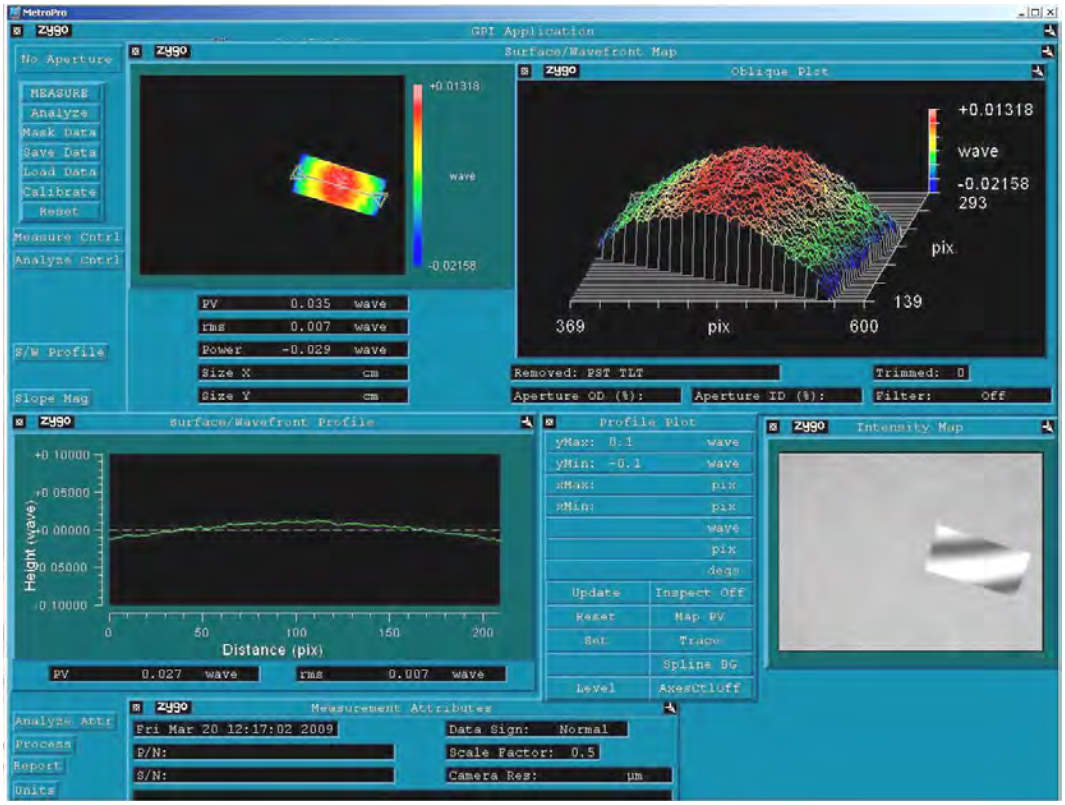

Figure 5.12: Zygo measurement of a U-groove without glued lens.

The measurement of the U-groove without glued lens showed the expected flatness of better than $\lambda/10$ as specified (figure 5.12). Peak to valley value (pv) over the masked surface is 0.035 wavelength ($\lambda/29$). The results of the measurements are summarised in table 5.1. The valley-deformation causes a global flatness of up to a pv of 2.305 wavelength. The fringe pattern of the measurements (figure 5.13 bottom right hand side) shows a similar shape as the dry area. Therefore it is likely that the U-groove for the lens bond of PFM

FIOS1 showed a similar valley-deformation, which caused the dry area. The flatness of the saddle deformation of $\lambda/3$ to $\lambda/2$ over the total surface and a flatness of better than $\lambda/4$ over most of the bonding area (figure 5.14) gives a possible reason why such dry area have not been previously observed in U-groove bonds.

	sample label	Flatness pv [wavelength]
Saddle-deformation	PFMlens2	0.453 (0.344)
measurements	FSlensMkI1	0.317 (0.182)
Valley-deformation	FSlensMkII1	1.986
measurements	FSlensMkII2	1.562
	FSlensMkI2	2.305

Table 5.1: Conclusion of the measured flatness of five samples. Central area flatness shown in parentheses.

The deformation of the U-groove is caused by forces generated during curing of the glue. An attempt was carried out to relax the stress of a U-groove afterwards and to recondition the former flatness quality of the U-groove bonding surface. A property of this glue allows the join to soften when it is heated to a higher temperature than was used for the curing process. During the curing process the U-groove and lens were cured at 40 °C. A sample U-groove (FSlensMkII1, pv = 1.986 waves) was reheated to 60 °C. After reheating of the lens the temperature was slowly decreased until it reached 24 °C after four hours. The flatness measurement was then repeated. But, it showed that this process caused a further deformation to pv = 2.282 waves. More lenses were glued into U-groves and the flattest ones selected for further PFM bonds.
Also the deformation over time and temperature was further investigated. The flatness of the U-groove mounts was tested and they show a flatness better as $\lambda/20$ before the lenses were glued into the mount. After the glue was cured

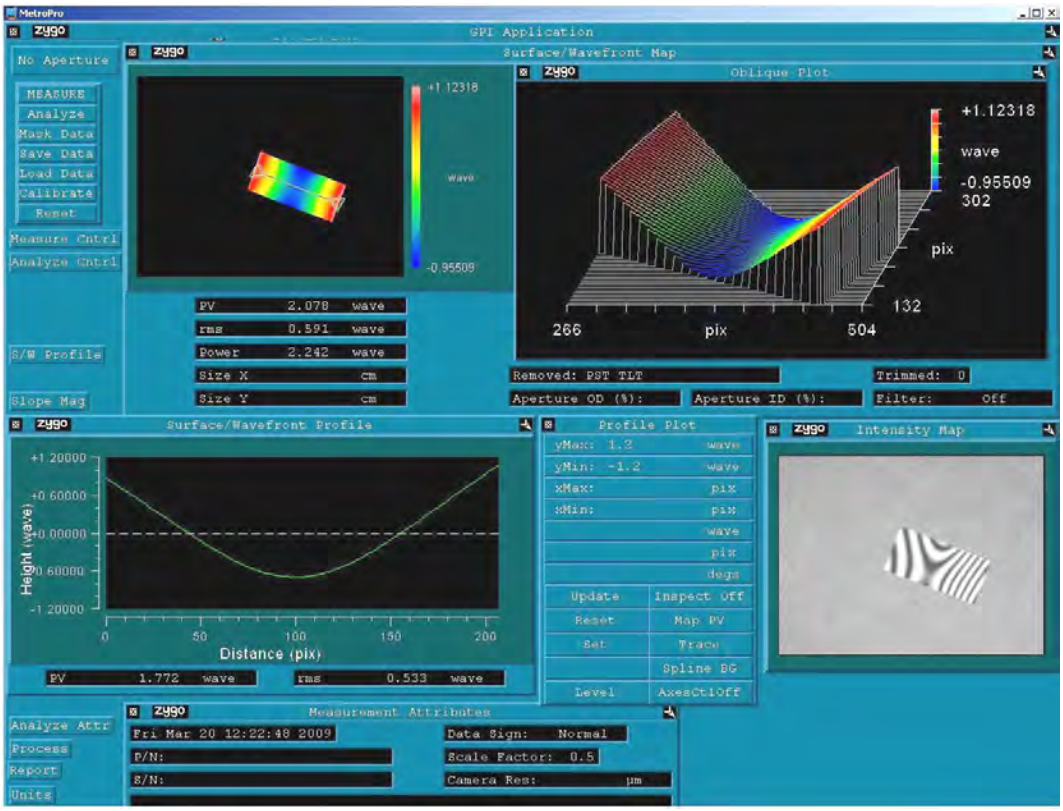

Figure 5.13: Flatness measurement of a valley shape deformation.

(2,5 days) at room temperature the flatness was measured. The measurement was repeated three days after the components were further cured in the oven at 40 °C. In the case of lens 16 and lens 18 the U-groove showed a valley deformation, which increased after placing the parts in the oven. The deformation of lens 16 was not measurable using the Zygo instrument; this leads to the conclusion that the deformation was greater than the instrument can measure. Lens 15 and lens 17 with a flatness of $\lambda/10$ after the lens glued in the U-groove developed a saddle deformation of better than λ over the total range and a flatness of $\sim \lambda/3$ in the central area after being in the oven. It is assumed that those lenses are suitable for further silicate bonds and they have been chosen for further LTP FIOS constructions.

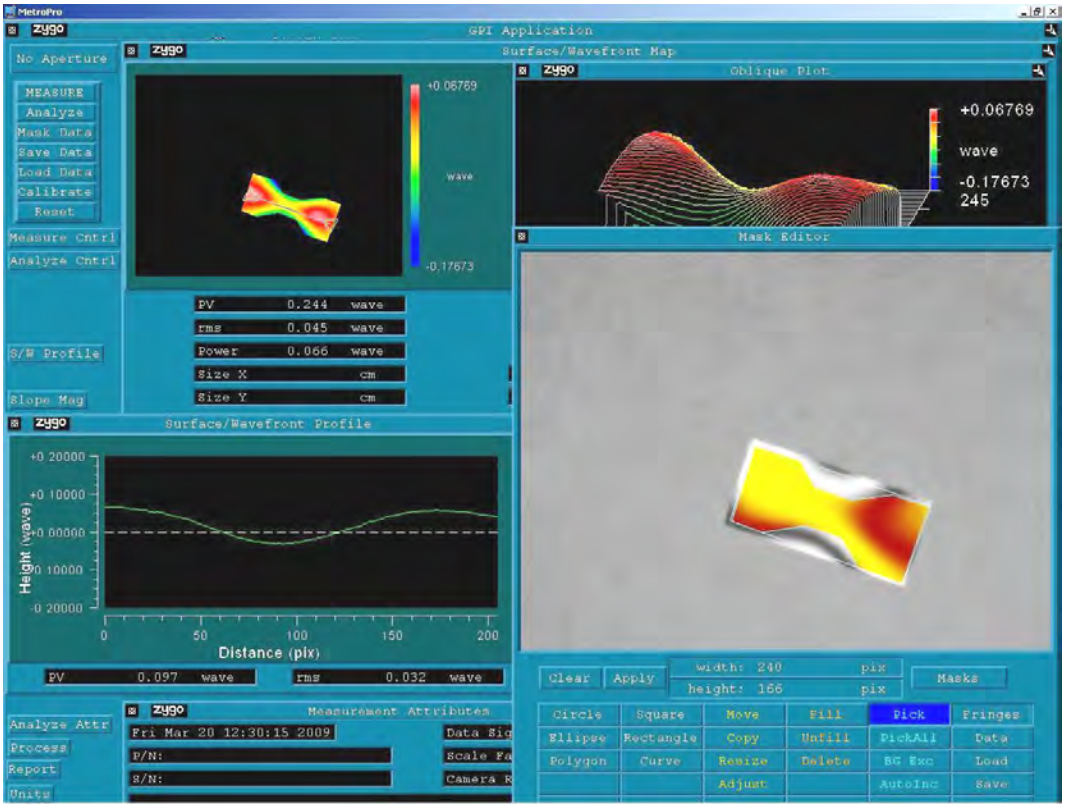

Figure 5.14: Flatness measurement taken over the ridge of the saddle shape (masked in colour in bottom right window).

Lens number glued in U-groove	Flatness pv before placing in the oven [wavelength]	Flatness pv after placing in the oven [wavelength]
lens 15 in U-groove 008	0.112	0.714 (0.334)
lens 16 in U-groove 009	0.474	not possible to take
lens 17 in U-groove 010	0.102	0.493 (0.297)
lens 18 in U-groove 019	2.285	2.778

Table 5.2: Conclusion of the measured flatness; in brackets is the flatness of the central area.

The deformations appear due to the U-groove thickness at its lowest point measuring 1.9 mm. The U-groove design was limited by the required height

of the beam. Such effects should be considered for future mount designs. For the current LTP optical bench project glued lenses have undergone a flatness check so that a suitable lens was chosen.

Figure 5.15 shows the bonded lens of the PFM FIOS2 model. The U-groove of the lens showed a saddle-shaped flatness deformation. As expected the bond covered almost the entire surface with the exception of the steep side of the saddle shape (marked in red in figure 5.15). To exclude the dry spots from the flatness analysis a mask was applied to the previous flatness measurement. The mask does not include these areas. A global flatness of pv = 0.388 wavelength is estimated for the bonded area. The amount of bonding fluid (0.432 μl) and the bonding force was sufficient to obtain a bond over almost the entire area. This confirms the assumption that saddle shaped deformation within the measured range of flatness allows silicate bonding.

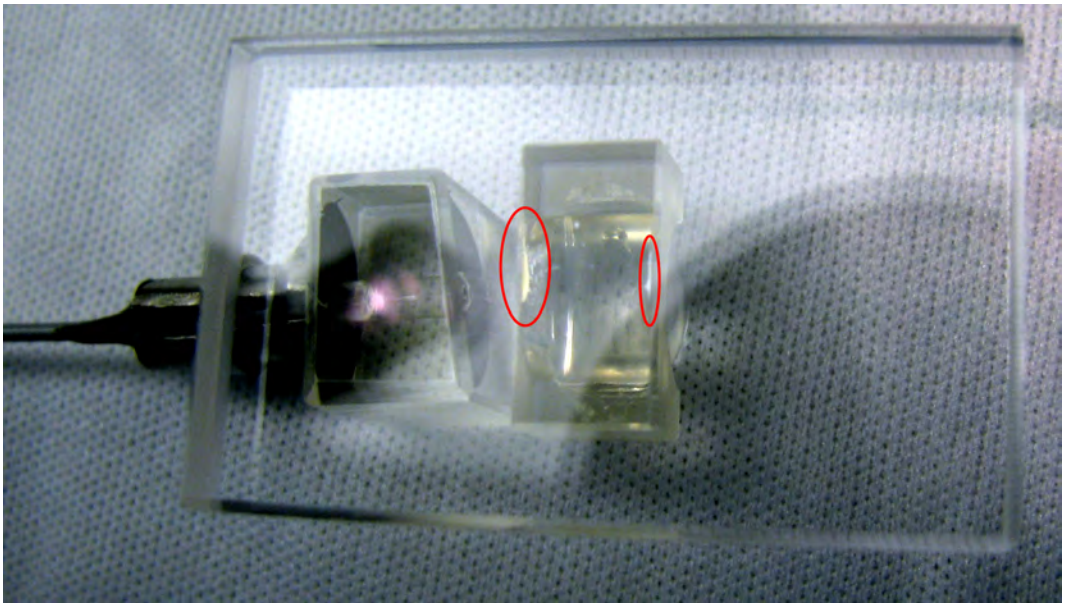

Figure 5.15: Photograph of a bonded saddle deform U-groove looking through the FIOS baseplate to the U-grove bonding surface (in red are marked the areas where dry spots appeared).

5.1.3 Polariser alignment

To ensure the correct polarisation (s-polarisation) on the prototype LTP optical bench, a fused silica polarizing beamsplitter cube is part of the FIOS design. The polarisation axis alignment out of the fibre is given by the fibre orientation in the FMA. Investigation of the optical properties of the flight qualified polariser showed that each polariser influences the beam differently in terms of beam pointing. As a result all polarisers were tested using the same stable input beam and a three point reference mount for locating each polariser under investigation in such a way that it was possible to compare the polarisers with each other. Not only does each polariser give a different beam shift but the amount of shift depends on the direction in which the light goes through the polariser. The polariser was set such that the rejected light was rejected vertically out of the measurement plane. This leaves two orientations for further investigation. The beam shift varies from a few tens of microrad to a few millirad. This is due to the polarisers not being perfectly square. This effect was used to compensate for another beam shift effect which was caused by the tolerances of the FMA template alignment. Each individual FIOS beam vector was measured before choosing a matching polariser to compensate best the in-plane beam shift closer to the ideal beam vector.

The polariser itself was placed at an angle of incidence to minimise back reflection in the system. In the case of the FIOS QM this was done with an angle of incidence of eight degrees, such that the beam shift caused by the polished front surface of the FMA was compensated. But this led to an unexpected effect on the polarisation axis. It was shown that the plane of polarisation at the output of the polariser is dependent on the angle of incidence. Therefore this attempt to control the beam shift was not used for later LTP fibre injectors. To stay within the polarisation angle tolerances, the polariser was rotated only two degrees, which is still sufficient to minimise the effect of back reflection.

5.2 Fibre injector placement

The fibre injectors were placed along the post, shown in figure 5.1. The post was bonded using a template, see section 4.5.1. The position of the post defines the position of the FIOS pair in X, and the rotation ϕ around the Z – axis. The bonding alignment procedure permits the FIOS to be aligned with respect to Y and most importantly to the height Z and the rotation θ around the X – axis. The rotation η around the Y – axis is defined by the post and FIOS baseplate perpendicularity. Figure 5.16 illustrates the coordinate system and the alignment principle for positioning the FIOS relative to the baseplate.

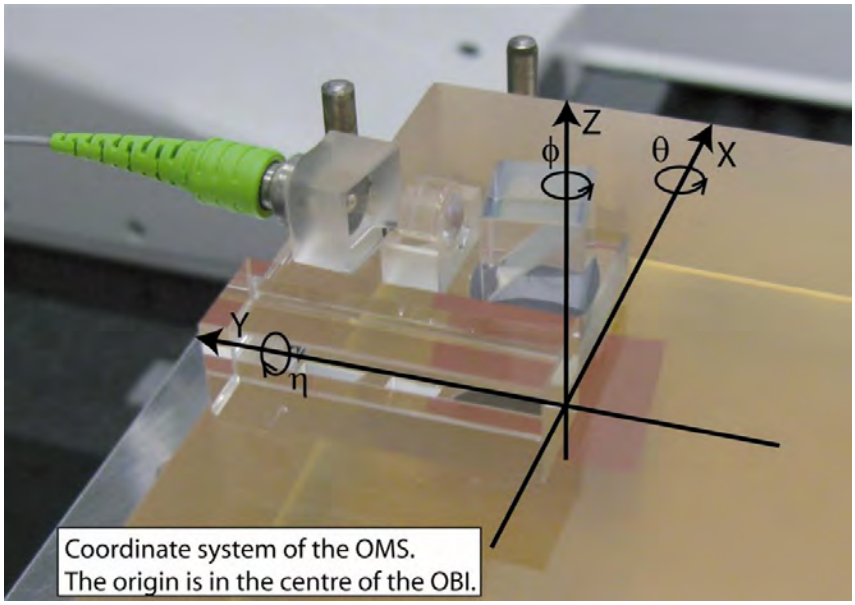

Figure 5.16: Coordinate system of the Optical Metrology Subsystem (OMS).

The bench is placed vertically with a slight tilt towards the positioner actuators which define the position of the FIOS such that the position of the fibre injector can be defined by the actuators settings. Figure 5.17 shows FIOS1 just after bonding. The fibre tail has to be supported during the alignment process (left hand side of the figure). The FIOS is aligned by aiming the beam

towards the CQP (right hand side of the figure), see section 4.5.2. The Opto-CAD simulation determines the beam vector. The CQP is then placed at the position of the simulated beam vector with respect to the optical bench. The CMM was used to find the position of the optical bench and hence to position the CQP.

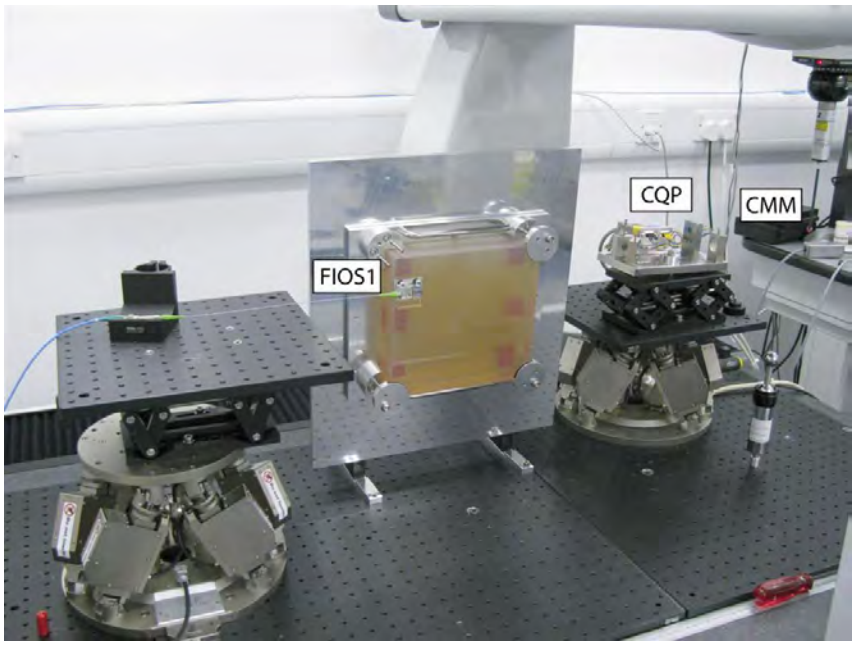

Figure 5.17: Photograph of FIOS1 QM bond.

Figure 5.18 shows the alignment of FIOS2 in more detail. Two 'positioner actuators are supporting and defining the position of the FIOS during the alignment procedure; they are positioned ~2 cm apart. The fibre tail has to be carefully supported to avoid affecting the FIOS positioning. Due to the slight tilt of the bench towards the "positioner actuator" a counter-balance was necessary to hold the FIOS vertically onto the post. The counter-balance was loosely hooked into the FIOS and occupied the gap between the FIOS baseplate and the optical bench, and was removed after the bond had formed.

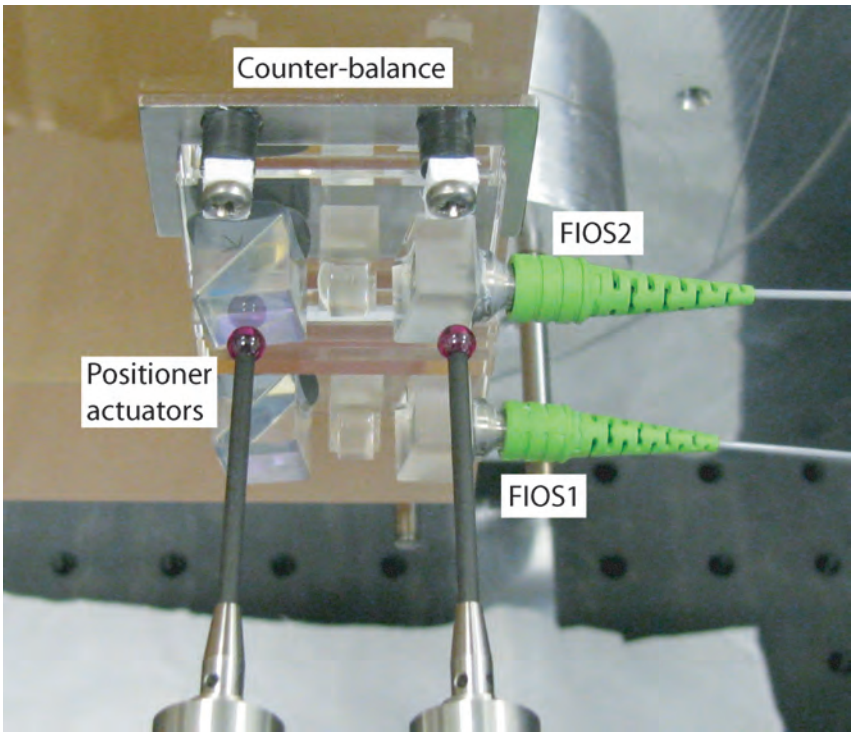

Figure 5.18: Photograph of FIOS2 QM bond.

During alignment the FIOS floats on an octane buffer solution until the correct position of the FIOS was found by adjusting the positioner actuators to complete the alignment. The repeatability of the FIOS position was tested several times before the FIOS was bonded. Only one FIOS is bonded at a time. After each bond the assembly has cured at room temperature for 24 hours and is placed in the oven at 40°C for seven days to cure the bond. FIOS1 QM and FIOS2 QM were bonded onto the post to a beam height of 12.5 mm (this is ~ 100 microns higher than for the LTP OBI; this compensates for the operation of the prototype LTP optical bench without optical windows) and parallel to the optical bench. The beam height of FIOS1 was measured to be 12.493 mm directly after bonding using the CQP and the angle in z direction of 6.3 μrad was measured after bonding. Further measurements revealed that the CQP had inadvertently been located incorrectly due to calibration issues. This re-

sulted in the beam having a different vector from the simulated beam vector. A more sophisticated measuring routine has been developed so that this error will not be repeated for further alignments using the CQP. The actual beam height and angle were measured after re-calibration of the CQP and curing of the FIOS pair. The beam height of FIOS1 is 12.485 mm and the angle in z - direction is 22 μrad. The beam height of FIOS2 is 12.486 mm and the angle in z - direction is - 15 μrad. However, this proves that the FIOS can be placed within the given requirement of a particular height and a parallelism to the optical bench of $\pm$ 30 μrad.

5.3 Fibre injector qualification

The fibre injector must undergo a full "space qualification" process [37]. This section presents the qualification project of the LISA Technology Package (LTP) fibre injector in terms of vibration and shock, thermal cycle tests, and associated optical performance tests. The mounting structure and method for sinusoidal vibration and random vibration tests as well as shock tests will be presented. A pair of fibre injector (FIOS) qualification models (QM) have been built to the same requirements and process as the proto flight model (PFM). This FIOS QM pair is bonded to a representative prototype Zerodur baseplate for the qualification process. The Zerodur baseplate is used as a reference baseplate for optical performance testing before and after the FIOS pair are subjected to vibration and shock and thermal vacuum tests and at various temperatures as part of temperature tests. In the case of the flight model LTP OBI environmental shaking tests, the bench will be mounted using specially engineered inserts. However the baseplate of the optical LTP prototype bench does not have inserts, and another way of mounting the baseplate is presented. Vibration and shock tests were carried out in two steps; firstly the mounting structure and method was pre-tested using a dummy Zerodur baseplate and secondly the qualification of the FIOS QM was carried out. The requirements of mechanical tests levels were relaxed between both steps as a result of spacecraft structure investigations at Astrium, Germany. There are a number of optical performance tests that were repeated at various stages of the building and testing of the fibre injectors pair. These are shown in Figure 5.19.

The results of the pre-tests are concluded in [38]. Further information can be found in following LTP project documents: [4], [39], [40], [41], [42], [43], [44], [45], [46], [47], [48], [49], [50], [51], [52]

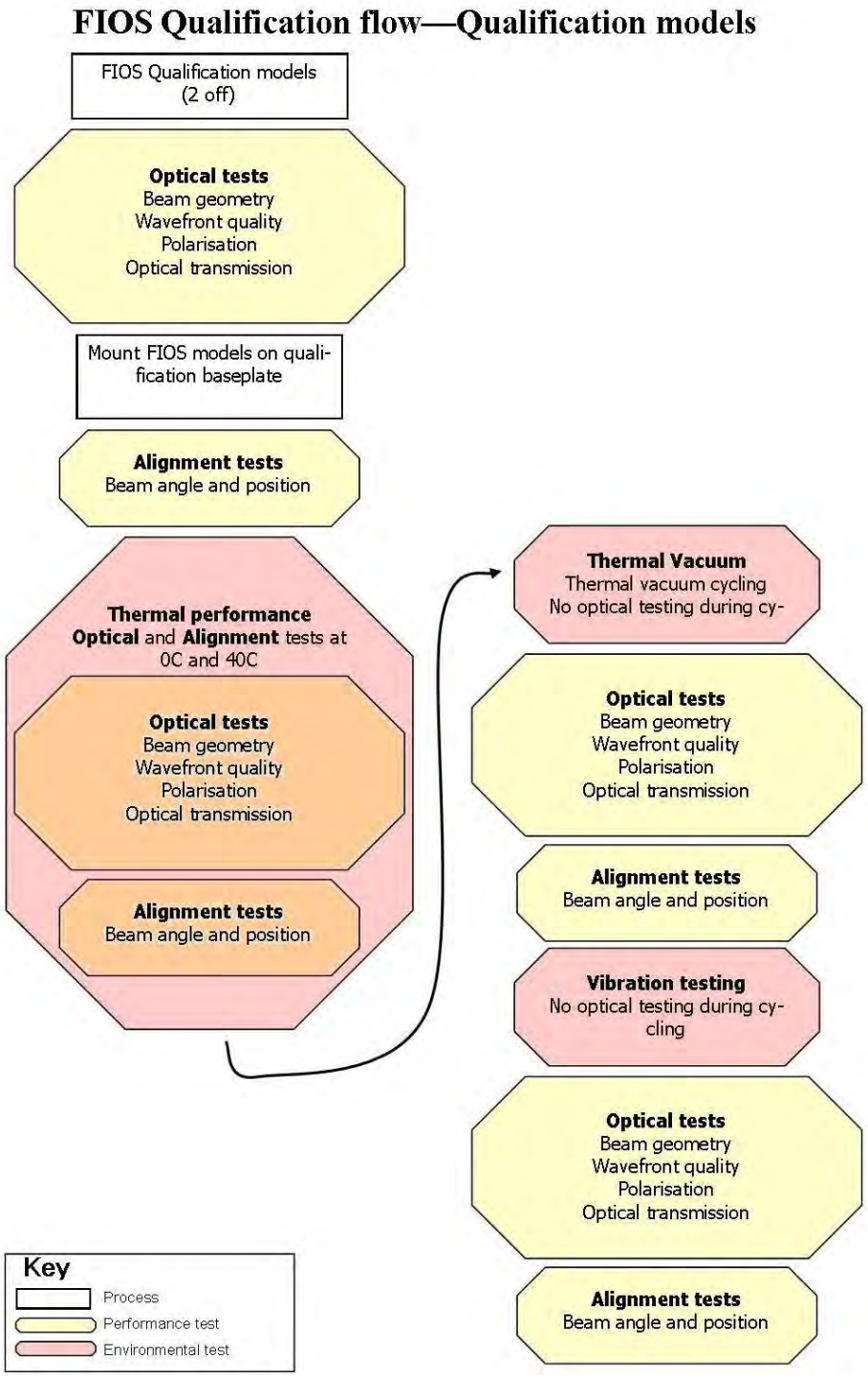

Figure 5.19: Performance and environmental testing of the FIOS qualification model [4].

5.3.1 Requirements of the fibre injector qualification process

The vibration and shock pre-tests were carried out to the original requirements of the LTP OBI structure, which are listed in table 5.3 and table 5.4. The tests were carried out to the qualification load with the acceptance load as the lower limit. The updated requirements to which the FIOS qualification model was carried out follow in table 5.5, and table 5.6.

Frequency Hz	Acceptance g	Qualification g
10	8	10
30	32	40
100	32	40
Sweep rate, 1 sweep up	4 octave/min	2 octave/min

Table 5.3: Original OBI sinusoidal qualification loads, along all three axes.

Frequency Hz	Acceptance PSD g^2/Hz	Qualification PSD g^2/Hz
20 - 100	+ 6 dB/octave	+ 6 dB/octave
100 - 500	0.32	0.5
500 - 2000	- 7 dB/octave	- 7 dB/octave
Total	15.5 g, rms	20 g, rms
Duration	60 s	120 s

Table 5.4: Original OBI random qualification loads, along all three axes. PSD (Power Spectral Density)

Frequency (Hz)	Qualification in X - axis
5	8 mm 0-pK
20	13 g
70	13 g
90	18 g
100	18 g
Frequency (Hz)	Qualification in Y - axis
5	9.3 mm 0-pK
20	15 g
40	15 g
60	20 g
100	20 g
Frequency (Hz)	Qualification in Z - axis
5	13.6 mm 0-pK
20	22 g
60	22 g
80	27 g
100	27 g
Sweep rate 1 sweep up	2 octaves per minute

Table 5.5: OBI sinusoidal updated qualification loads depending on the OMS – axes.

The fibre injector assembly is subjected to thermal vacuum cycling. The thermal vacuum cycling is specified in the document [41]. For the OBI the operating temperature range is 10° C to 30° C and non-operating and storage temperature ranges are both 0° C to 40° C [OMS-5.3-16]. The qualification temperatures are these ranges extended by 10° C. The tolerance of the temperature is ∼3 ° C. Qualification tests were preformed at 0 ° C and again at

Frequency (Hz)	Qualification in X - axis and Y - axis [g^2/Hz]
20	ramp up with +6 dB/octave
80	0.13 g^2/Hz
400	0.13 g^2/Hz
2000	ramp down with -7 dB/octave
Total	8.9 g, rms
Duration	120 sec
Frequency (Hz)	Qualification in Z - axis [g^2/Hz]
20	ramp up with +6 dB/octave
100	0.5 g^2/Hz
150	0.5 g^2/Hz
200	ramp down to 0.08 g^2/Hz
700	0.08 g^2/Hz
2000	ramp down with -7 dB/octave
Total	11.1 g, rms
Duration	120 sec
Frequency (Hz)	Shock levels in X - axis and Y - axis SRS, g (Q=10)
70	5 g
1000	200 g
10000	200 g
Frequency (Hz)	Shock levels in Z - axis SRS, g (Q=10)
70	5 g
700	50 g
10000	50 g

Table 5.6: OBI random and shock updated qualification loads depending on the axes; SRS (Shock Response Spectrum).

40 ° C; in addition optical performance tests were also carried out at 10° C and 30° C. These tests are performed at atmospheric pressure. Furthermore the qualification model must undergo a thermal vacuum cycle. Optical performance tests (OPT) are made at 20 ° C before and after the cycle process at atmospheric pressure and before and after environmental tests also at 20° C for comparison.

5.3.2 Mounting structure and method for vibration and shock tests

A suitable mounting structure was needed, which holds the prototype Zerodur baseplate and can be easily mounted onto the vibration table. To mount a Zerodur baseplate into this mounting structure a strong but temporary joint was needed. Waxes are commonly used to mount glass for polishing and cutting, therefore different waxes were tested in small shear tests, of which *Logitech Quartz* wax seemed the most suitable for this application.

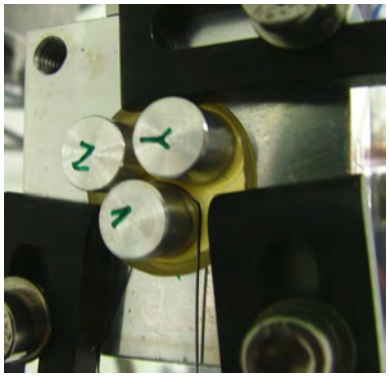

Figure 5.20: Picture shows a wire loop around one of the three aluminium pieces wax-bonded to an one inch Zerodur test disc.

Different sized aluminium pieces were wax-bonded onto one inch Zerodur test discs. The aluminium pieces and the test discs were heated to 70°C and the wax was applied. After the assembly cooled down, these discs were clamped in a

close fit mount for the pulling test. A loop of wire were used to apply a force to one of the waxed samples by means of a pulling engine as shown in Figure 5.20. The average adhesion of the tested *Logitech Quartz* wax is $15.82 \pm 0.43\,\mathrm{kg/cm^2}$. This is three times more than the required value of $5\,\mathrm{kg/cm^2}$ [38]. Afterwards the Zerodur test discs have been cleaned of the wax using acetone and were prepared as usual for silicate bonding [53]. It was shown that silicate bonding is still possible after removing the wax.

Large scale tensile tests were also carried out using two 10 cm diameter discs, which had been wax bonded together and were then pulled apart. Six test runs were carried out. The measurement were carried out using a commercial pulling machine. The wax bonded pieces are mounted in a jig and are pulled apart from each other. The force is measured and displayed against the travel distance of the pulling machine. Forces of $8.4 \pm 1.2\,\mathrm{kN}$ were measured, shown in figure 5.21. This equates to $\sim 10\,\mathrm{kg/cm^2}$. In the case of run3 at the bottom part of the curve some margin can be observed, which is due to the mount in the pulling machine.

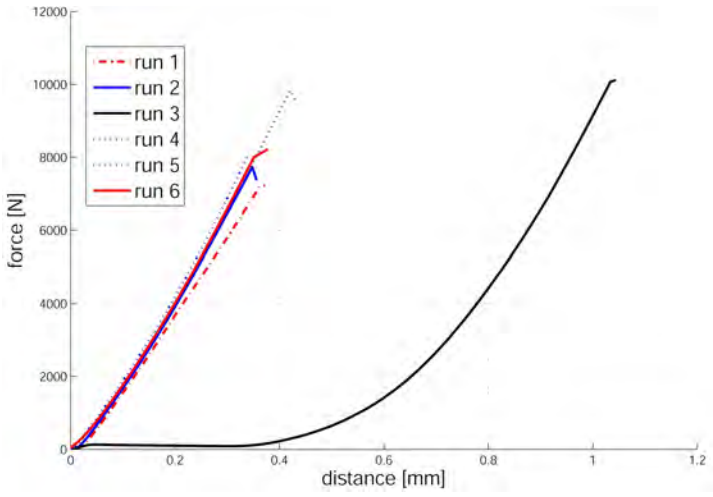

Figure 5.21: Graph of measured force of tensile tests.

These measurements show that the wax-bond would be strong enough to hold a Zerodur baseplate under the toughest acceleration of 40 g. But the behaviour of the wax-bond is unknown during vibration and shock tests, therefore a test run with a wax-bonded dummy Zerodur load was carried out.

Figure 5.22 shows the dummy Zerodur load wax-bonded into the designed hollowed aluminium adapter plate and the safety structure top plate. The aluminium adapter plate has a thickness of 60 mm and is hollowed out to a depth of 20 mm to provide a close fit to the size of the Zerodur baseplate. The baseplate is wax-bonded in the adapter plate. The limiting factor for the thickness of the hollowed adapter plate is the mass - the vibration table has a mass limit of 20 kg for our required pre-tests vibration and shock loads.

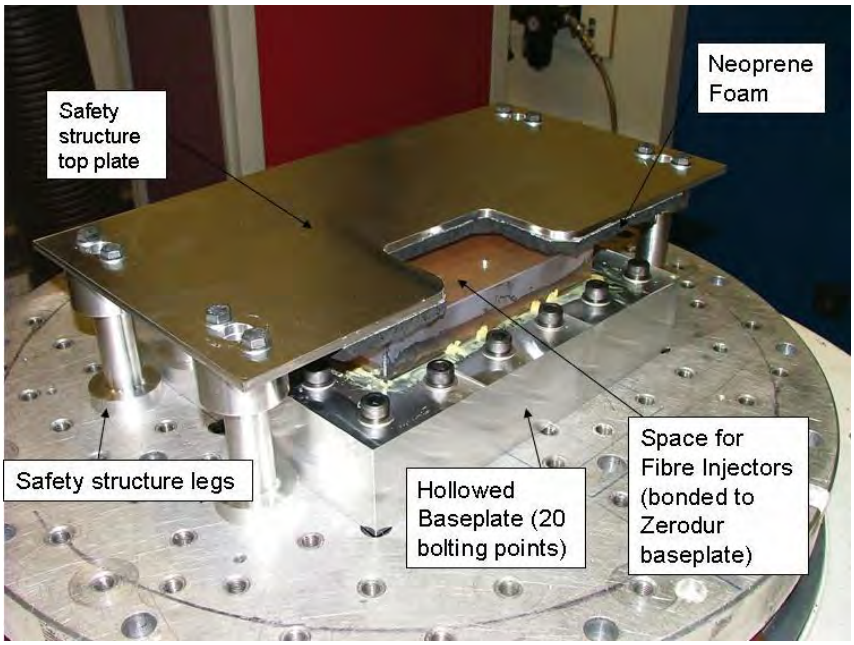

Figure 5.22: Picture of mounting structure on vibration table.

The behaviour of the top plate and the adapter plate including the baseplate during vibration and shock tests was modelled using finite element (FE) analysis. This was done to model the first resonance mode, so that damage to

the baseplate could be avoided. In the case of the adapter plate including the baseplate the first resonance mode was modelled to be over 2000 Hz, which would be above the maximum applied frequency of the planned tests. The first resonance mode of the safety structure was modelled to be 163 Hz, therefore the safety structure is placed over the Zerodur baseplate with a gap such that it is never in contact with the Zerodur baseplate.

5.3.3 Results of the vibration and shock pre-tests

The pre-tests of a dummy Zerodur baseplate (without the FIOS pair) wax-bonded into the mounting hardware were conducted and the results were successful. Figure 5.23 shows the graph of the sinusoidal vibration test in the horizontal direction. Three accelerometers were waxed onto the Zerodur baseplate, the hollowed adapter plate and the top plate. It is easy to see that the acceleration of the Zerodur baseplate and hollowed mount are similar. The acceleration of the top plate is increasing with frequency, due to the fact that the top plate resonance mode is lower and easier to excite, and the top plate shows in figure 5.24 the first resonance mode at 163 Hz. This agrees with the figure obtain by finite element analysis. Furthermore the Zerodur baseplate and the hollowed adapter plate are showing the desired effect of behaving like a monolithic entity with the predicted first resonance mode at 2.1 kHz.

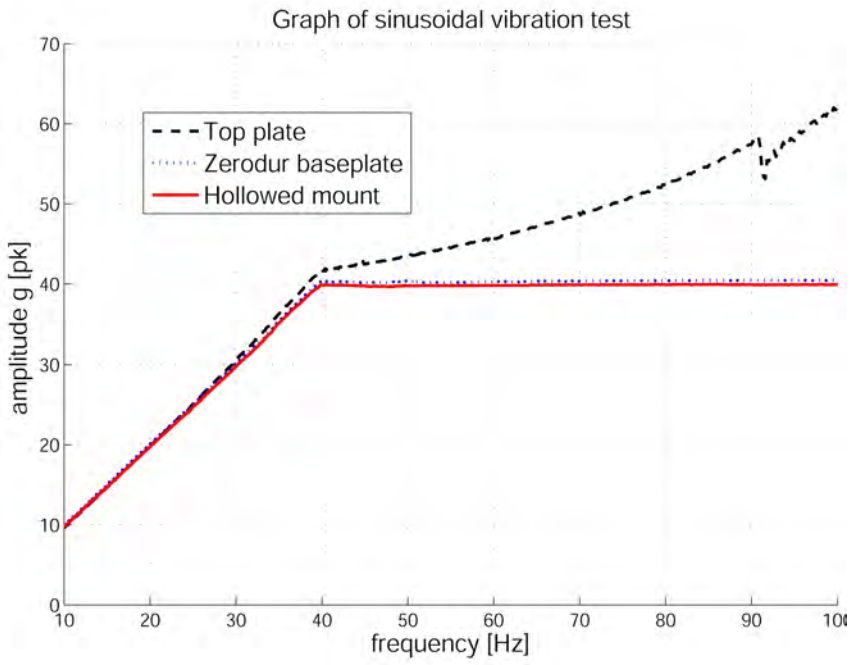

Figure 5.23: Graph of sinusoidal vibration test

The shock tests were even more challenging than the vibration tests. The wax-bond was not renewed before the shock tests were carried out. During the pre-test, damaged areas of the wax-layer were detected after six shocks shown in figure 5.25. Afterwards five more shocks were carried out before the wax-layer and the Zerodur baseplate became loose. The Zerodur baseplate was left undamaged. The damaged wax layer looks like a sheared surface with loose cuts. This appears in the photograph picture as white/light-yellow. As a summary, it can be said that the wax-bond fulfilled the requirements for a suitable joining technique, because after each shock the wax-layer could be examined and if necessary the wax-bond could be redone by heating the structure to re-form it. This was successfully demonstrated by placing it onto a heat plate and re-melting the wax.

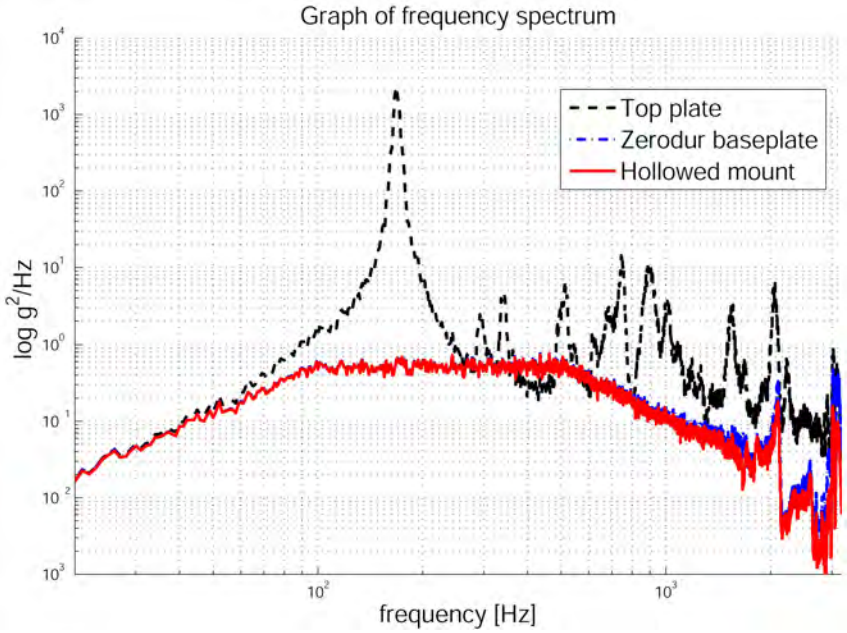

Figure 5.24: Graph of frequency spectrum.

These tests have shown that the waxing technique is ideal to provide a strong but temporary joint of the optical bench to a mounting structure. After re-

Figure 5.25: Picture taken through the Zerodur of the wax layer after six shocks.

ducing the load requirement of vibration and shock tests damage of the wax layer is less likely. Careful and regular inspections of the wax layer allow the detection of a damaged wax layer at an early stage. The monolithic behaviour of the mounting structure and the optical bench itself allows the measurement of the applied acceleration on a particular place of the mounting structure and contact with the optical bench can be avoided. Before and after vibration and shock tests optical performance tests of the FIOS QM were carried out. These tests and their results are discussed in section 5.7.

5.4 FIOS QM vibration and shock tests

This section gives an overview of the vibration and shock tests of the FIOS QM. The tests were carried out at Selex-Galileo, Edinburgh. The mounting structure and harnessing of the fibre cable during tests will be explained and a summary of the response vibration and shock curves given. The FIOS qualification in terms of vibration and shock tests was carried out following the routine shown in figure 5.26 to the level described in section 5.3.1.

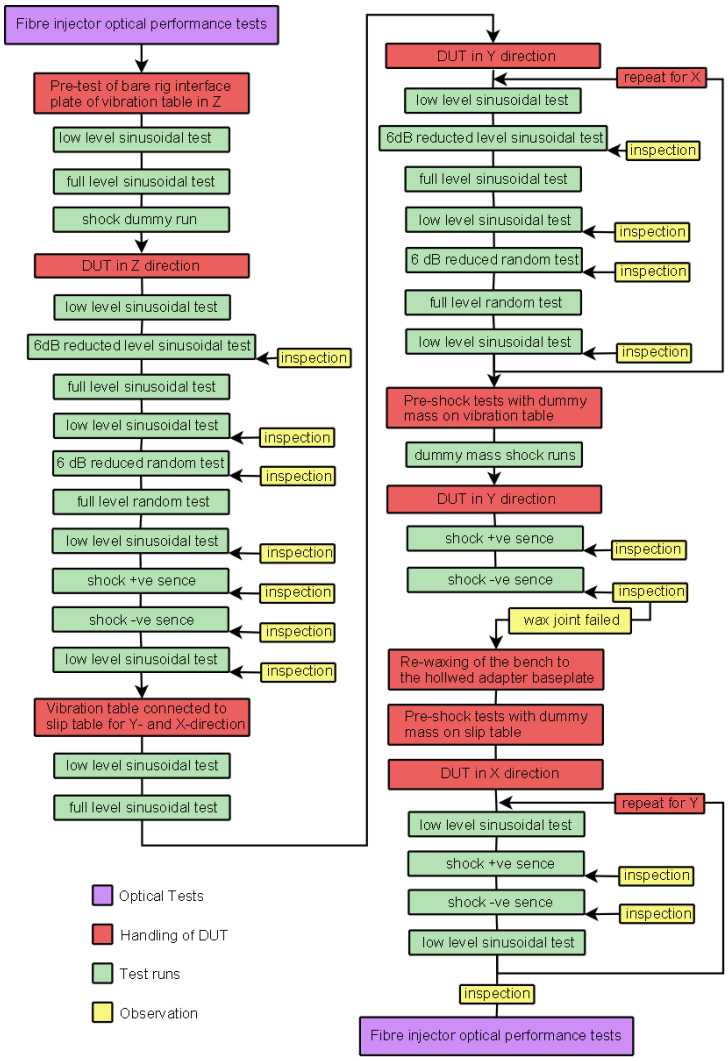

Figure 5.26: Flow diagram of vibration and shock tests as carried out.

5.4.1 Handling of FIOS QM assembly for tests

The hollowed adapter plate is heated in the oven at 100° C. The wax is spread inside equally before the pre-heated FIOS QM Zerodur baseplate is placed in the hollowed adapter plate. To avoid an over-heating of the FIOS pair, the entire assembly was placed on a 40 kg aluminium mass to absorb the heat. This is shown in figure 5.27.

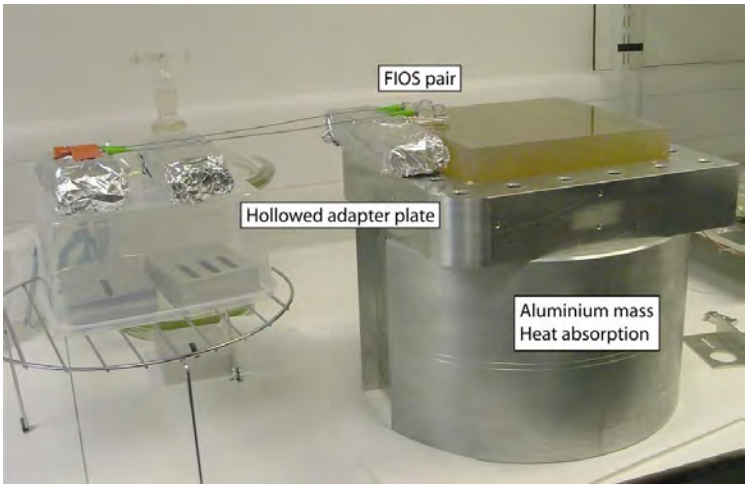

Figure 5.27: Wax bonding of the FIOS QM Zerodur baseplate to the hollowed adapter.

The fibre cables of the FIOS were secured to the hollowed adapter plate in a similar way to that used on LTP. The secured points were at similar distances to those specified for the OBI harness routing. They are screwed at the side of the hollowed adapter plate. At the tie-down points, Viton tubing was placed over the PEEK cladding to protect the fibre, and cable ties were used to secure the fibre to the hollowed adapter plate. The cable ties (shown in figure 5.28) were applied without putting pressure on the PEEK. The Diamond fibre connectors were screwed into a holder attached to the side of the hollowed adapter plate. The red cup was lightly screwed on and epoxy glued temporarily for the tests.

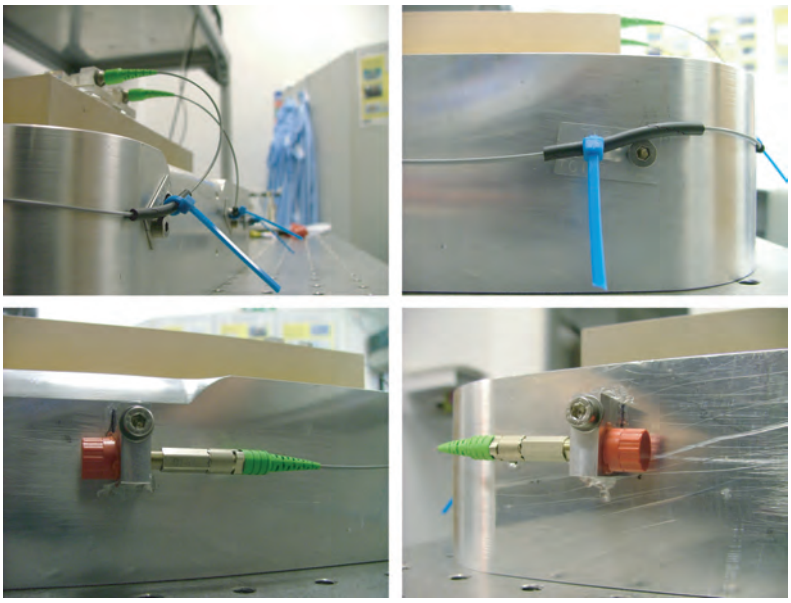

Figure 5.28: Top left and right pictures show the fibre cable routing. Bottom left and right pictures show the mounting of the FC-Diamond connector.

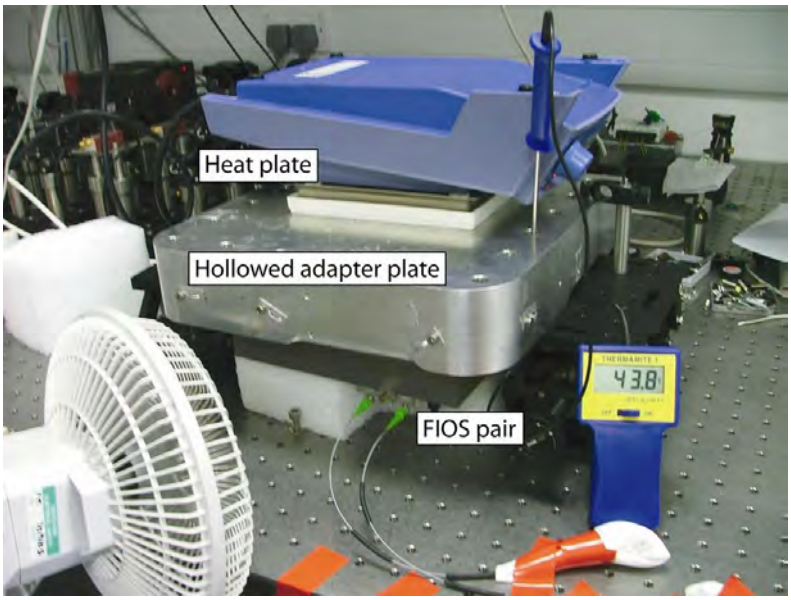

Figure 5.29: De - waxing of the FIOS QM baseplate.

During tests re-heating of the assembly became necessary, after the wax-layer failed at the shock test in Y-direction. The assembly was reheated on the heat plate and the top surface in the region of the FIOS QM pair was water cooled and was kept below 40 °C.
Figure 5.29 shows the set-up for the de-waxing of the FIOS QM Zerodur from the adapter mount after the tests were completed. A heat plate heats up the bottom of the adapter mount. The assembly is set-up upside down such that the Zerodur can drop out onto a foam layer when the wax melts. To avoid over-heating of the FIOS QM pair an air fan was used for cooling.

5.4.2 Set-up on the vibration table

The FIOS QM baseplate assembly is placed directly onto the vibration table for Z-orientation; for Y- and X-orientations it is attached onto the slip table, which is connected to the vibration table. A tri-axial accelerometer is attached to the hollowed baseplate at a point located below the position of the FIOS post. Two control accelerometers are attached to the vibration table itself, shown in figure 5.30.

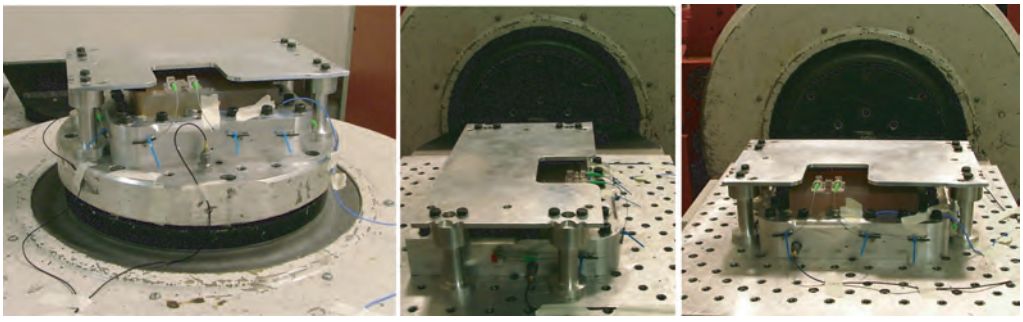

Figure 5.30: DUT attached on vibration table for Z-axis (left) and on slip table for X-axis (middle) and Y-axis (right).

5.4.3 Conclusion of tests

The individual curves can be obtained from [44]. Figure 5.31 shows the sinusoidal curves of all three orientations. The curves fulfil the requirements, listed in table 5.5. Figure 5.32 shows the response curve of random tests and also fulfils the requirements listed in table 5.5 within the tolerance range of ± 10 % in acceleration.

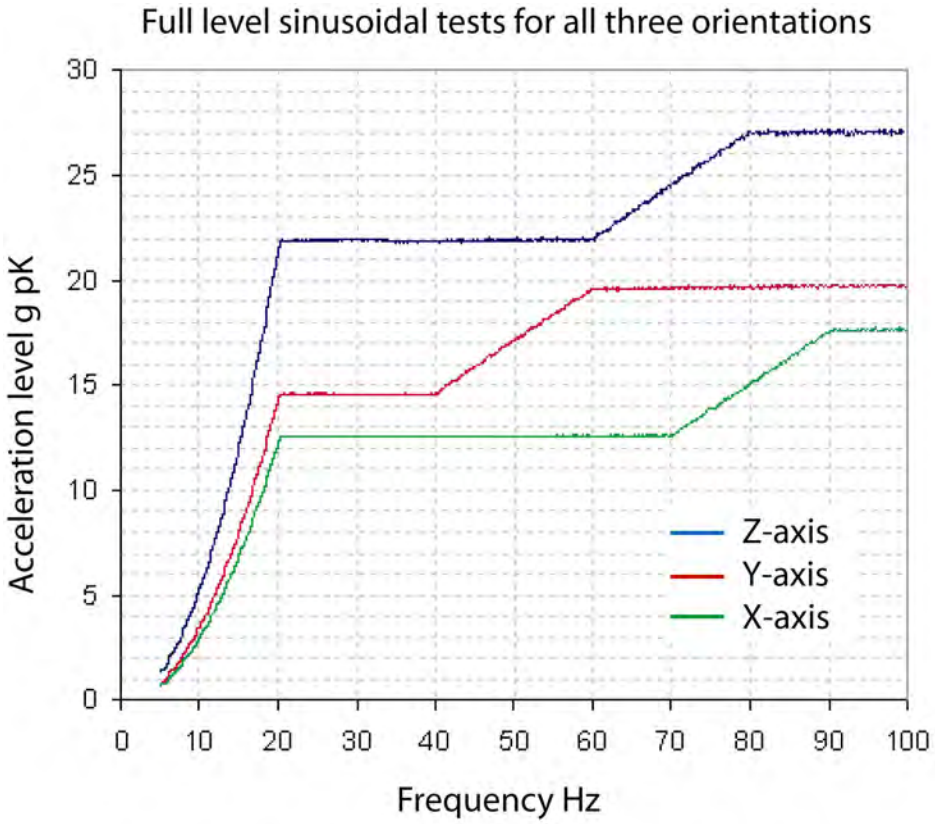

Figure 5.31: Measurements of the acceleration during sinusoidal tests in all three orientations.

Figure 5.33 shows the shock response spectrum (SRS) of all orientations. The tolerances of the shock tests are marked as pale areas in the graph. The SRS

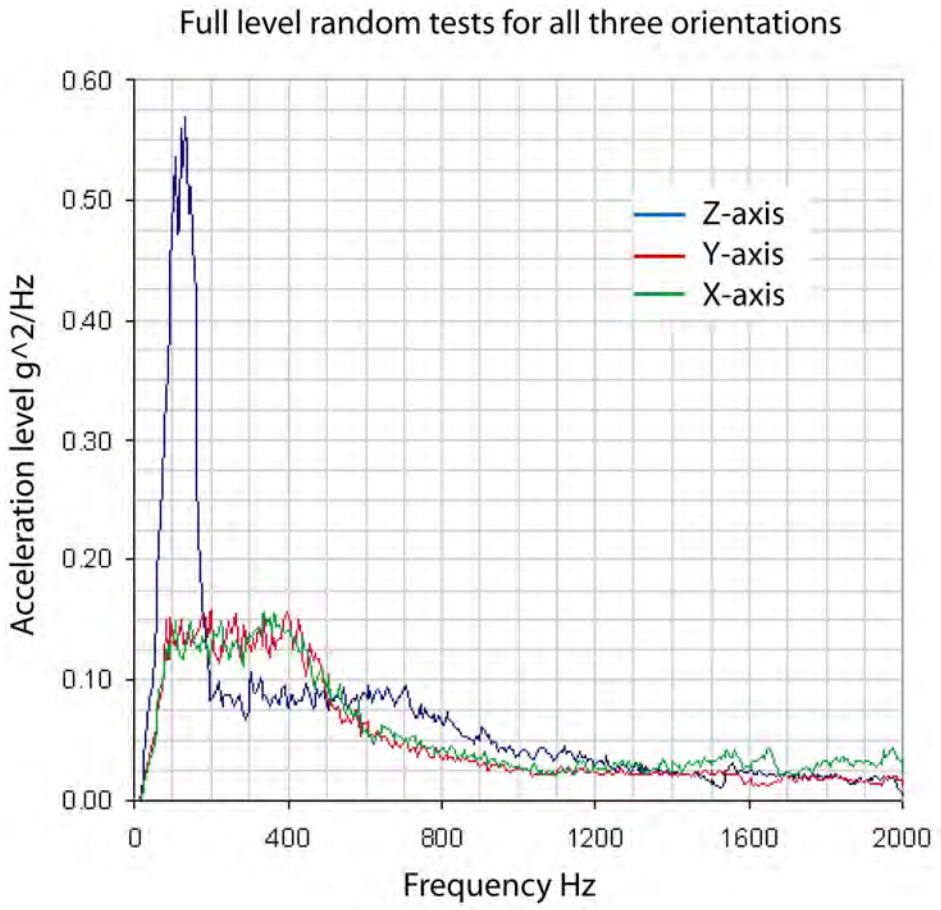

Figure 5.32: Measurements of all three orientations during random tests.

curve of shocks in Z - axis shows that the response curve is within the tolerances in the lower frequency range, above 4 kHz the curve is slightly below the tolerance. The same is the case for shock in the X - axis. The SRS curves for shocks in X - and Y - axis are also showing a slight overtesting of the DUT. These difficulties in X - and Y - axis are due to the experimental limits of the vibration table attached to the slip table. The tests for the Z - axis were carried out directly on the vibration table. Shocks were carried out first on the vibration table for Y - axis, but it appeared that the wax joint is easier to break in the case of shocks and shear forces at the same time. Hence, the shocks for Y - axis have been repeated on the slip table. On the slip table the wax

joint showed some effect due to the shock, but the baseplate kept connected in the hollowed adapter mount through all the shock runs for X - and Y - axes.

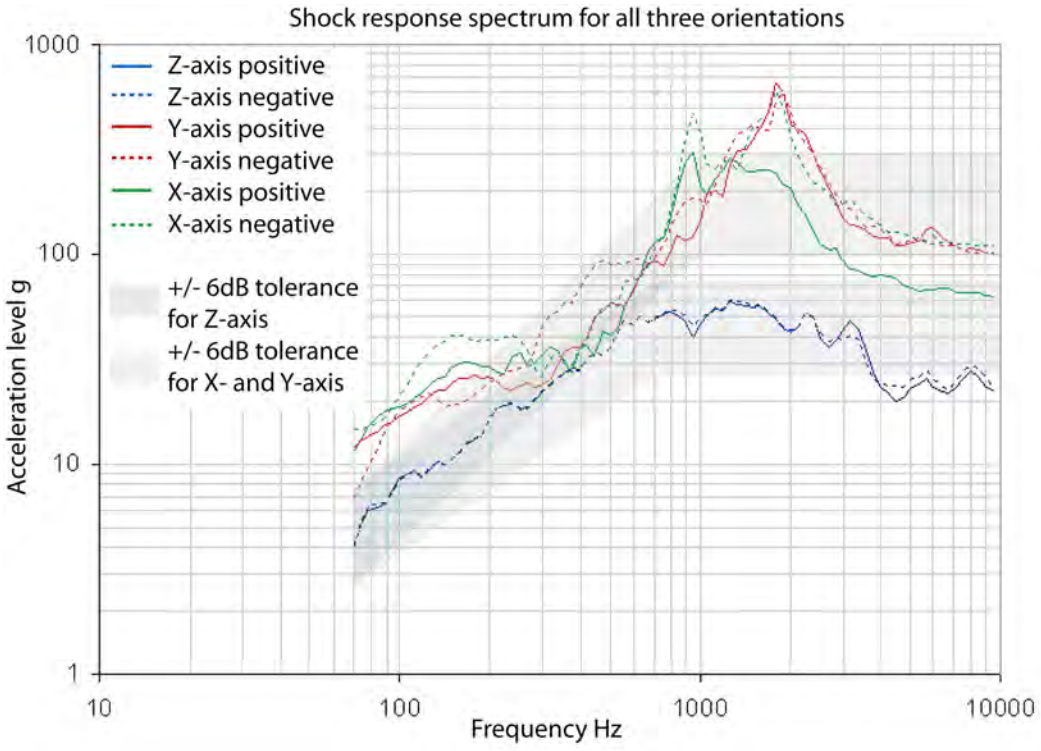

Figure 5.33: SRS curve of all six orientations.

5.5 FIOS QM thermal vacuum tests

The thermal vacuum test was carried out at SELEX - Galileo, Edinburgh. The facility allows one full cycle every six hours. The FIOS QM Zerodur baseplate was placed on a heat plate, which was attached to the vacuum tank tray, shown in figure 5.34. Thermocouples monitor the temperature of FIOS1, FIOS2, the post, Zerodur and one fibre connector. The sensor on the Zerodur baseplate next to FIOS1 became loose during the experiment. The fibre connectors are placed on a metal post beside the Zerodur. The whole assembly is then mounted into the vacuum tank and evacuated to 0.5×10^{-5} Torr before the temperature cycle began.

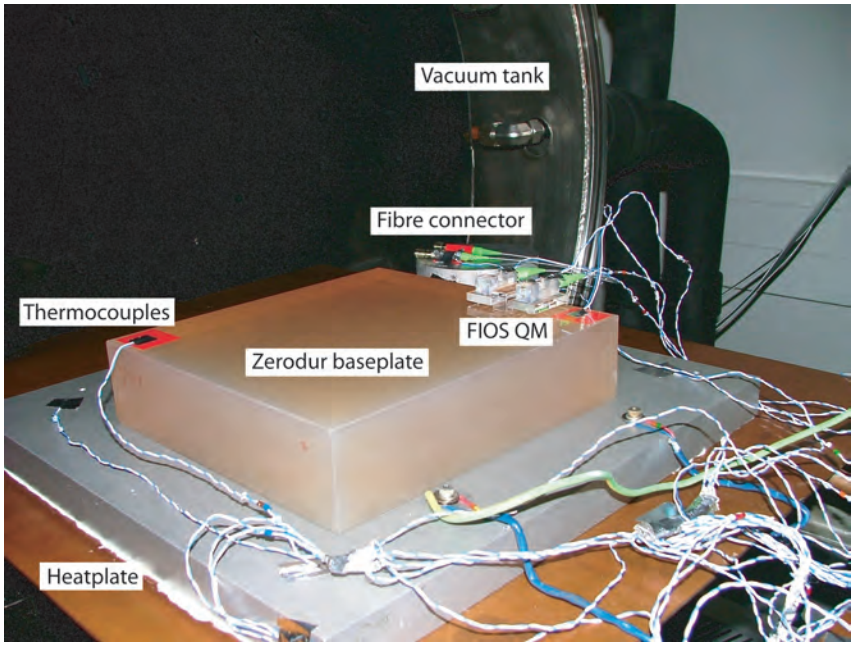

Figure 5.34: Photograph of FIOS QM bench on vacuum chamber tray.

The temperature curves of both FIOS are shown in figure 5.35. The green marked areas indicate the tolerance band of the target temperatures. In total 7.5 cycles were carried out.

The temperature curve of the fibre injector post, Zerodur baseplate and fibre connector are shown in figure 5.36.

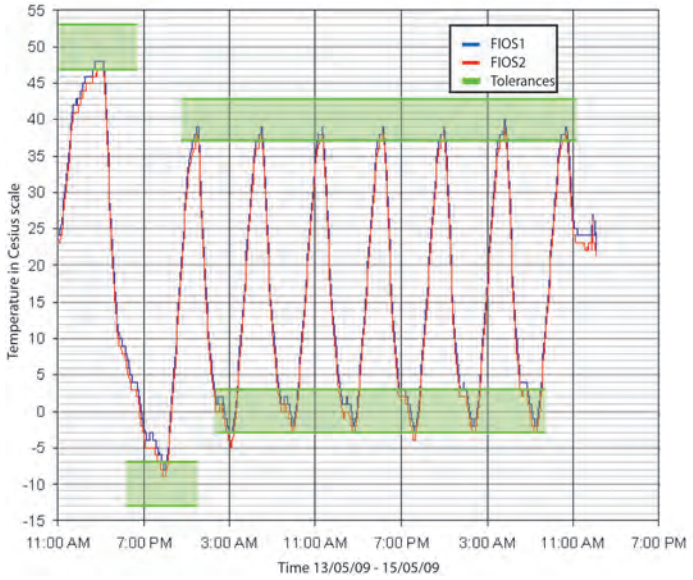

Figure 5.35: Graph of temperature cycle of FIOS QM; in green are the temperature tolerances marked.

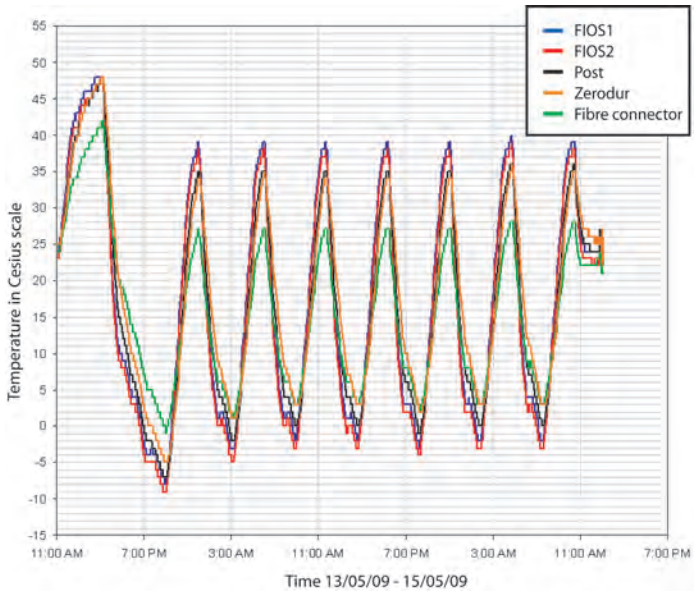

Figure 5.36: Graph of temperature cycle of all sensors.

5.6 FIOS QM temperature tests

The FIOS QM bench is placed on a copper heat plate inside a thermal insulating box (LEGO). The heat plate has a pattern of channels in it through which fluid can be circulated. A Julabo control unit circulates the fluid at a controlled temperature through the heat plate to achieve the desired temperature. The temperature is monitored using a temperature probe PT100, which is placed in the middle of the FIOS on top of the FIOS post and held in place with an aluminium weight. A LEGO lid closes the box, not shown in figure 5.37. The position of the bench is measured using the CMM. The lid (not shown in figure 5.37) has holes to allow access for the CMM probe when the bench is at temperature. Optical Performance Tests (OPT) were carried out at 0 ° C, 10 ° C, 20 ° C, 30 ° C and 40 ° C. In the case of the 0 ° C measurement a dry air flow was installed to prevent condensation on the FIOS QM pair.

5.7 FIOS QM optical performance tests

The following tests have been carried out: optical throughput, polarisation angle, beam geometry, interference contrast (at an equivalent recombination distance of X1-X2 OBI interferometer), wavefront quality (as above), beam position and angle.

In the case of temperature cycle the FIOS QM bench is placed in a thermal insulated (LEGO) box on a heat plate, shown in figure 5.37. The heat plate can be driven from - 30 ° C to + 80 ° C. For these tests the heat plate was operated from 0 ° C to + 40 ° C. The optical performance tests of the beam

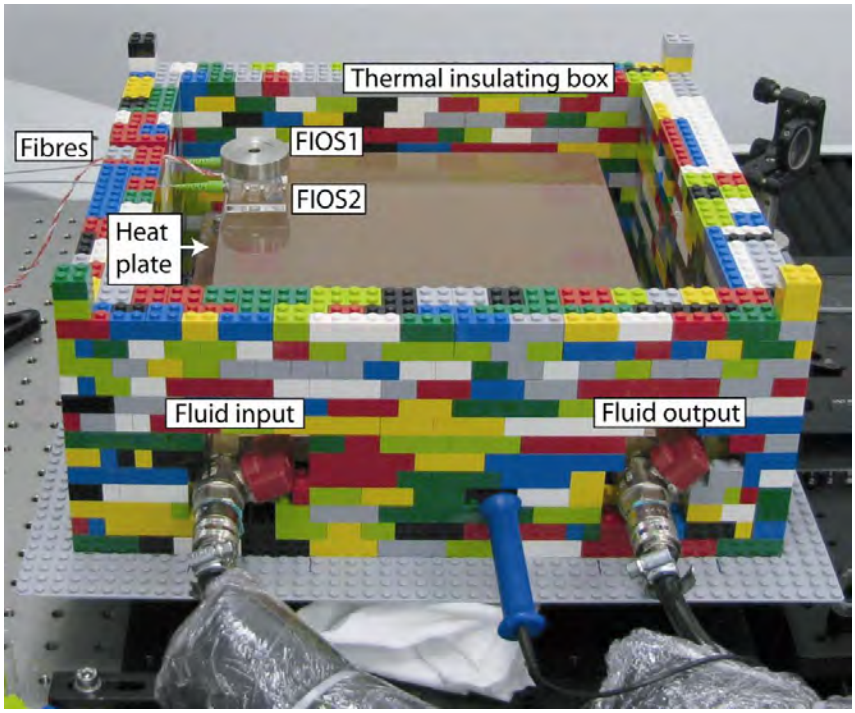

Figure 5.37: Photograph of the thermal test set-up.

where carried out once the beam left the Zerodur baseplate and the thermal insulation. The tests were kept at a similar distance every time that a test was repeated throughout the qualification process.

5.7.1 Optical throughput

The optical throughput was measured by comparing the amount of light coming directly from a commercial fibre with the beam from the FIOS using the same photodiode and feed-in fibre. This is shown in figure 5.38. Due to the beam expansion out of a fibre, the beam was measured within a few millimeters of the fibre end.

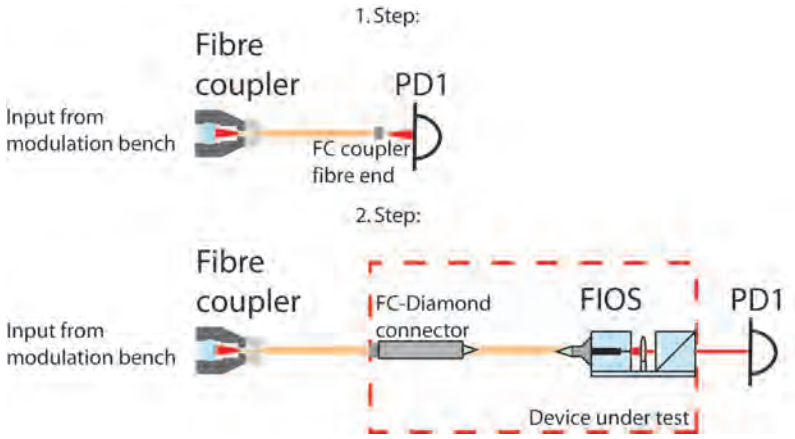

Figure 5.38: Schematic drawing of experimental set-up for optical throughput.

Variations in the transmitted optical power are observed depending on the mounting of the fibre FC connector into the DIAMOND fibre adapter. In particular the connector of FIOS1 was very unreliable and the optical throughput varies from 50 – 80 % depending on whether the fibre FC connector was screwed into the DIAMOND connector or manipulated such that a maximum output was reached. This effect dominates the measurements of the optical throughput for FIOS1 such that during environmental tests the measurements of optical throughput would not be sensitive enough to observe any other effects which may influence the optical throughput. The optical throughput of FIOS2 varies between 81 – 96 % for the same reason. In general it can be said that no temperature influence on FIOS2 could be observed. The values are

fluctuating due to the sensitivity to the faulty connector and the measurement uncertainties. The value for both FIOS at 0 °C is lower than the average. It is assumed that this is caused by condensation effects on the surfaces. The beam has to transmit through four surfaces after the beam output. Table 5.8 provides a list of the optical throughput at particular temperatures.

Temperature Date	FIOS1 optical throughput in %	FIOS2 optical throughput in %
20 °C (13/04/09)	74	93
30 °C (16/04/09)	45	88
40 °C (17/04/09)	56	91
20 °C (17/04/09)	80	96
20 °C (27/04/09)	70	81
10 °C (07/05/09)	49	81
0 °C (22/05/09)	27	73
20 °C (29/06/09)	71	95

Table 5.7: Individual optical throughput measurements at particular temperatures.

5.7.2 Polarisation angle

The polarisation axis of the beam from each FIOS was measured using the same PBS in a rotatable mount for all tests. The set-up is shown in figure 5.39. The transmitted light for both minima was measured. In the case of maximum measurements the maximum throughput was determined by rotating the PBS to maximum throughput and taking the reading on the PBS mount. Due to laser fluctuation this reading has a higher uncertainty than the measurements using the minimum throughput. The minimum throughput

was taken by rotating the mount in 2° rotation steps around the minimum throughput. This gave an accurate reading of the minimum throughput. The total measurement error is estimated at ± 2°. The same PBS in its mount was used for all measurements in order that comparison between the different measurements can be made.

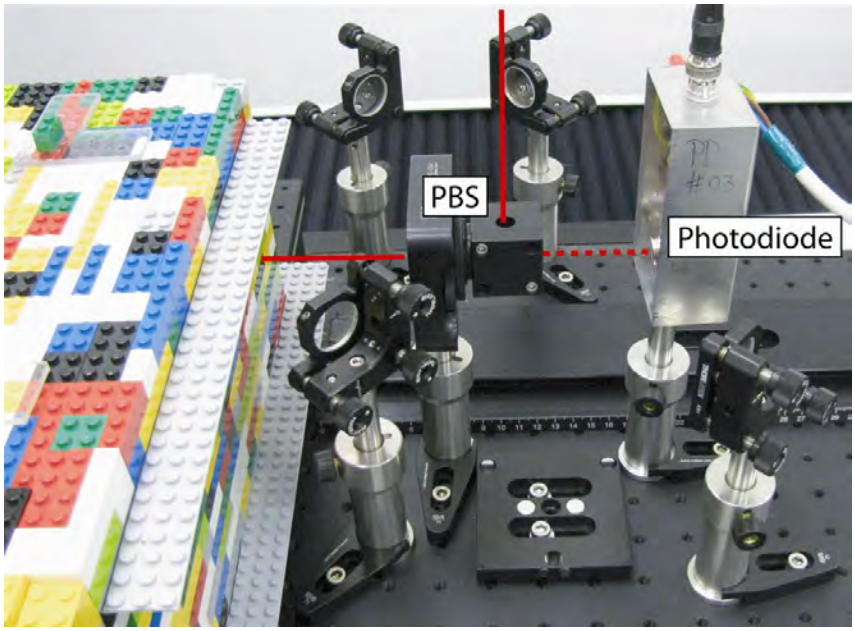

Figure 5.39: Photograph of set-up for polarisation angle measurement.

The beam polarisation angle is altered by the eight degree orientation of the PBS on the FIOS baseplate. The tests show that the polarisation of the beam does not depend on temperature. The polarisation measurement of the beam using maximum throughput is difficult to determine due to laser power fluctuation. Hence the minimum throughput was used for polarisation measurements. The measurements were done within ± 2° accuracy. FIOS1 has a polarisation of 8° ± 2° and FIOS2 of 6° ± 2° in respect to the OBI top plane and this does not change with temperature.

5.7.3 Beam geometry

A CCD camera (WinCAM) is used to measure the beam geometry (beam size and ellipticity). The WinCAM is mounted onto a rail, shown in figure 5.40 on the right hand side. The beam geometry is measured at 5 cm steps. The closest the WinCAM can get to the Zerodur bench is ~8 cm or ~28 cm from the FMA; In figure 5.40 the FIOS QM Zerodur is still attached to the hollowed adapter plate which is wrapped in foil to prevent contamination of the clean room.

Figure 5.40: Photograph of the set-up for the beam parameter measurement after vibration and shock tests.

Figure 5.41 shows the comparison of FIOS1 and FIOS2 in relation to the measurement points on the LTP OBI. The average beam diameter for several 20 °C measurements was taken and a linear fit was done (ignoring the non-linearity of the beam-size spreading). Figure 5.41 shows the beam diameter of FIOS1 in red and FIOS2 in blue. The blue measurement curved is shifted by ~36 cm towards the red curve, so that comparison of the beam diameters at the combination points of the LTP OBI can be made in the case of the reference, X1, and X1-X2 interferometers. The blue curve is not shifted for comparison of

the frequency interferometer. In light green in figure 5.41 are the areas marked of the positions of the combined beams at the measurement photodiodes. As shown, both beams fulfill the requirements of the beam diameter to be 1000 - 1300 μm at all measurement-relevant interferometer points. Furthermore the ratio between both beams is in the range of 1.000 - 1.037 which is < 1.2 as required.

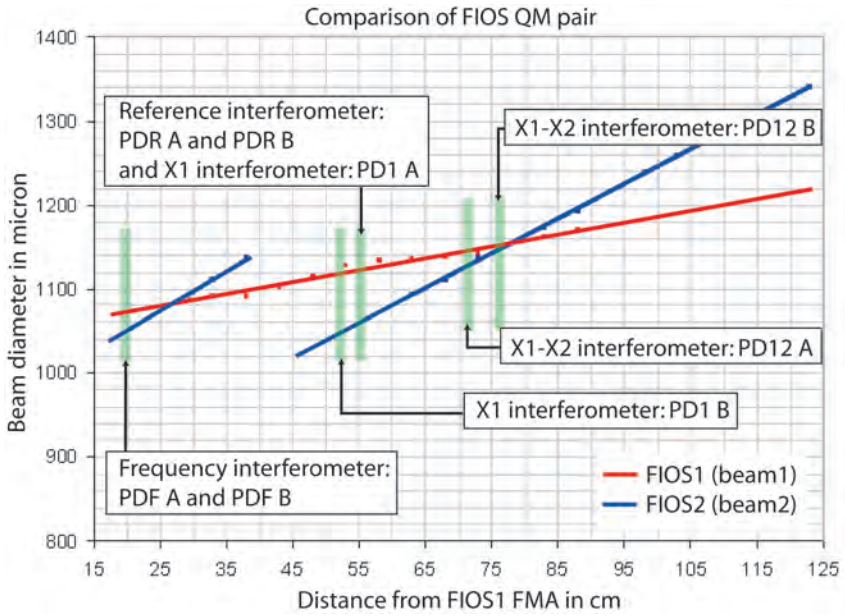

Figure 5.41: Comparison of the beam diameter of both FIOS at room temperature.

Figure 5.42 shows the beam diameter of FIOS1 and FIOS2 for several 20 °C measurements. It can be seen that the different measurements are within ± 3 %. The same fluctuation of ± 3 % also appears during beam diameter measurements for different environment temperatures, shown in figure 5.43. No temperature effect was observed in terms of beam diameter. The same is the case for both beams' ellipticity which was measured to be between 0.95 and 1.01, fulfilling the requirement of being between 0.85 and 1.17.

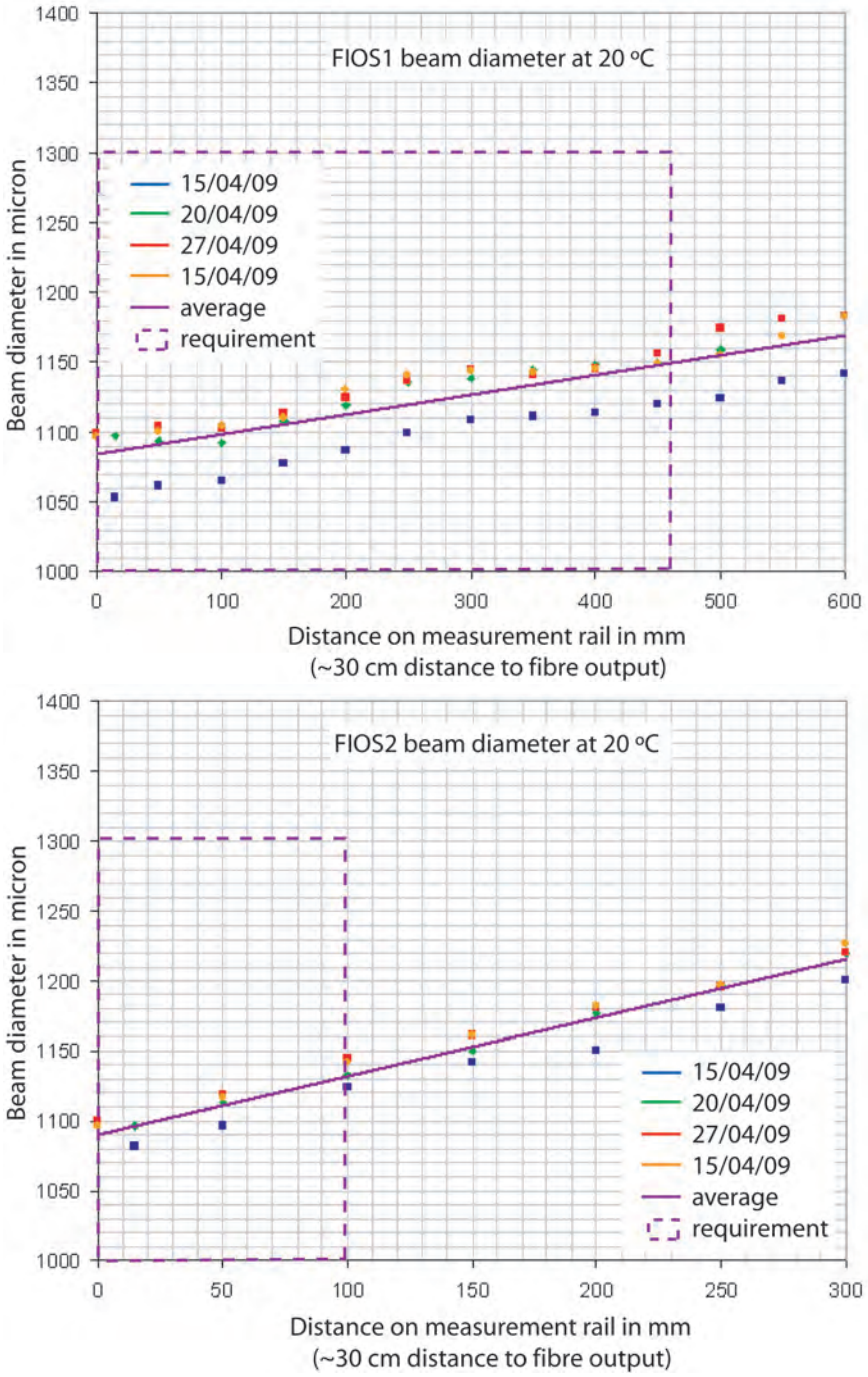

Figure 5.42: Beam diameter of FIOS1 and FIOS2 at several 20 °C measurements.

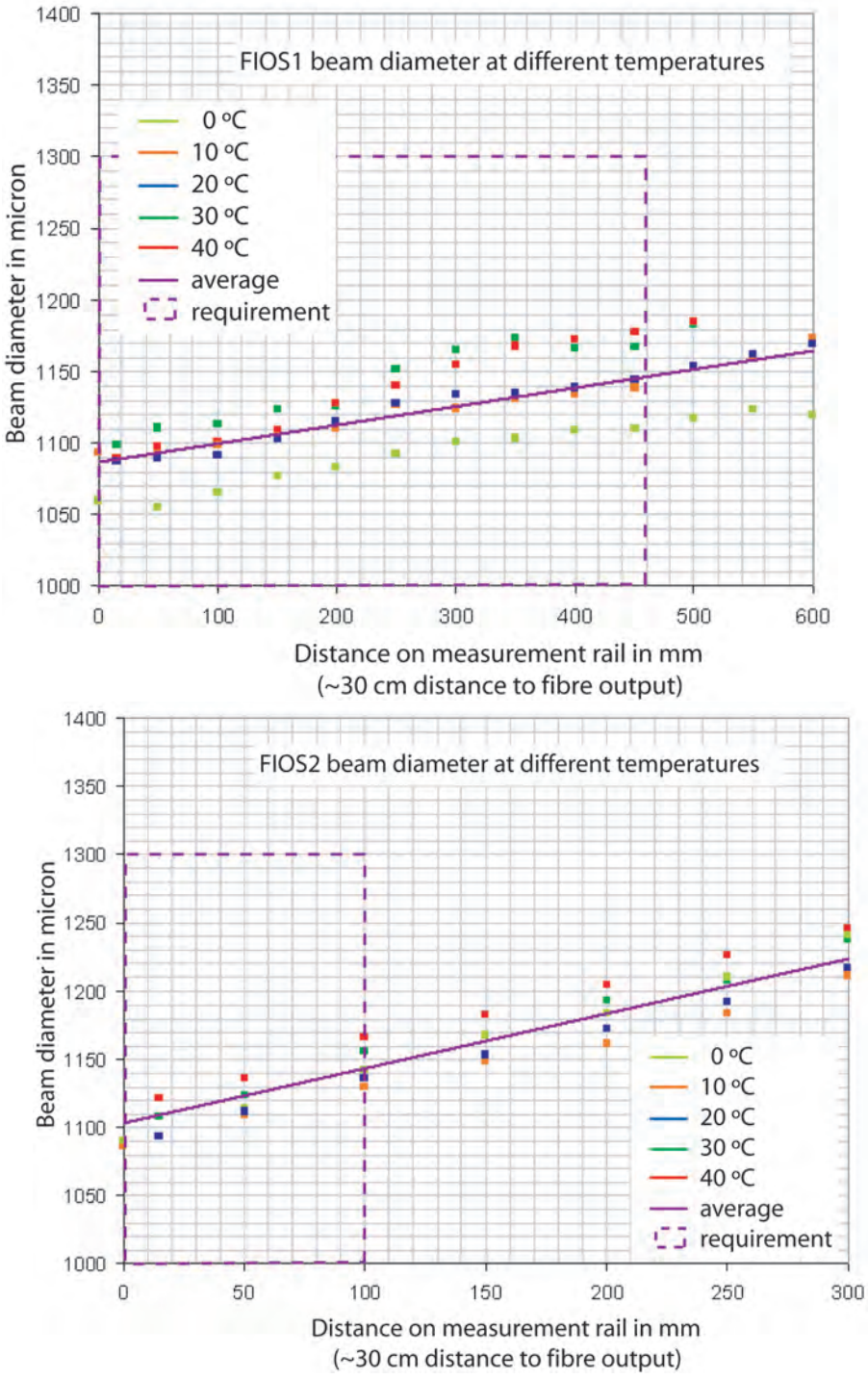

Figure 5.43: Beam diameter of FIOS1 and FIOS2 at different temperatures.

5.7.4 Interference contrast

The same breadboard which is used for setting-up the beam geometry and polarisation experimental set-up is used for the interference measurement. Both beams are brought to interference contrast using commercial mirrors and beamsplitters inside adjustable mounts, such that an optimum interference can be achieved. The pathlength of beam1 (FIOS1) is ~84 cm, and of beam2 (FIOS2) ~48 cm from the beam output of the FMA. A pathlength difference of ~36 cm is used to represent the OBI interferometer layout of X1, and X1-X2, and reference interferometers. The contrast obtained was 97 ± 3 % and was independent of temperature changes.

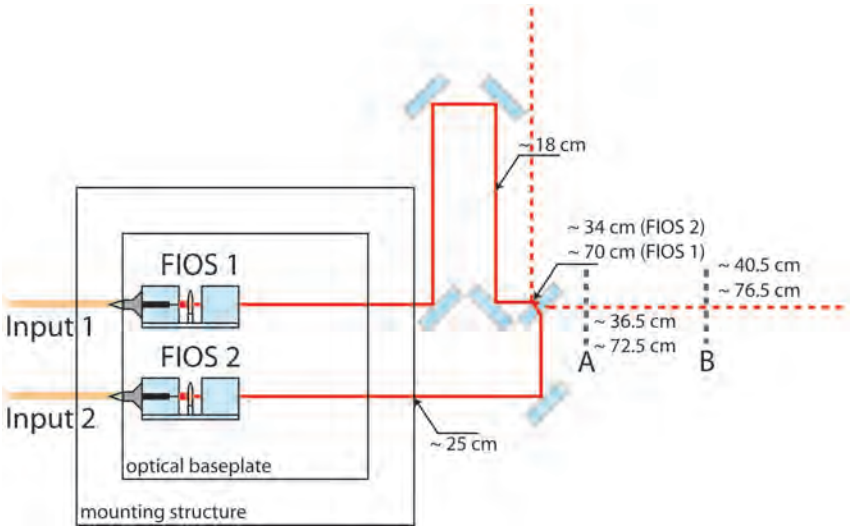

Figure 5.44: Schematic diagram of experiment set-up interference measurement.

5.7.5 Wavefront quality

The set-up for measuring the wavefront quality of the superposed beams is similar to the set-up of the interference measurement. This is shown in figure 5.45. The recombined beam is monitored by an InGaAs wavefront camera [33].

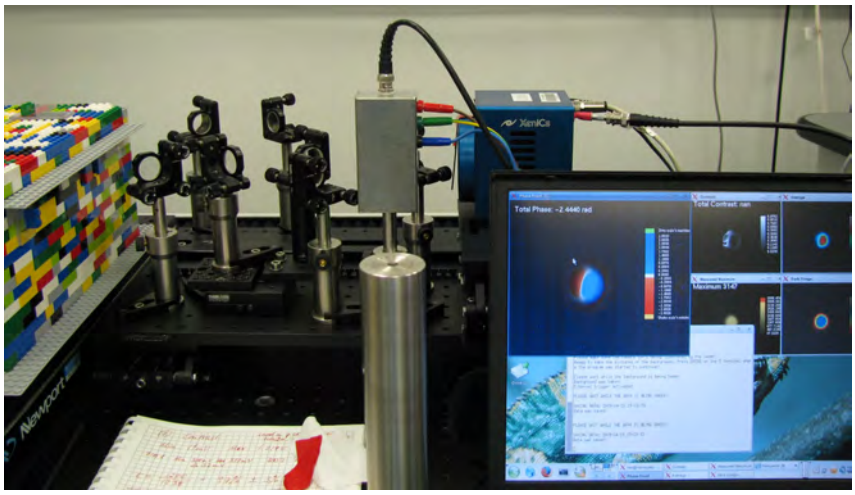

Figure 5.45: Photograph of set-up for interfered beam wavefront measurement.

The wavefront measurement was carried out at a distance of ~90 cm. This is ~14 cm further than the actual combining measurement photodiodes of the X1 – X2 interferometer. The relative wavefront measurement is in the range of 0.3 - 0.6 radian ($\leq \lambda/10$) and does not show any dependence on temperature. Figure 5.46 shows two typical relative wavefront plots of the combined QM beams. Due to the relative wavefront pattern the individual beam wavefronts in the first plot are curved with a different bending radius and cross each other twice. In the case of the right hand plot the individual wavefronts are tilted towards each other with only one crossing in the middle of the beams. The graph plots an area of 1200×1200 microns; the actual beam size is smaller and circular.

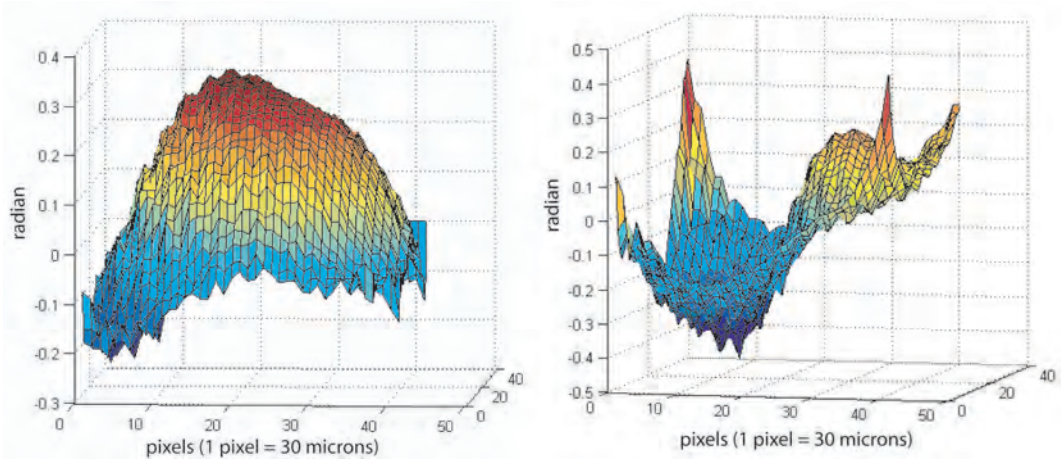

Figure 5.46: Two typical pictures of the wavefront quality of the combined FIOS QM beams taken at a distance of ~ 90 cm from the beam origin.

5.7.6 Beam position and angle

The positions and angles of the beams from FIOS1 and FIOS2 are measured using the Calibrated Quadrant Photodiode (CQP). The CQP is placed on a Hexapod, so that it can be aligned to the incoming beam. The beam was centred on the CQP. The relative position of the Zerodur baseplate and the CQP are measured using a CMM and from this data the beam positions and angles can be determined. Two effects due to temperature have been observed: First the beam was noisier on the CQP read-out system, probably due to convection currents, and second the beam itself was bent upwards by higher temperature and downwards by lower temperatures. A very clear effect of beam bending was observed when the lid of the LEGO box was removed and the beam bend upwards instantly and once the lid was placed back the beam bend downwards. Several investigations were carried out to decouple the beam pointing from the temperature influence. The beam path was covered using tubes of different length. An air fan circulated the air to avoid temperature gradients and the FIOS QM itself was thermally insulated, shielding it with

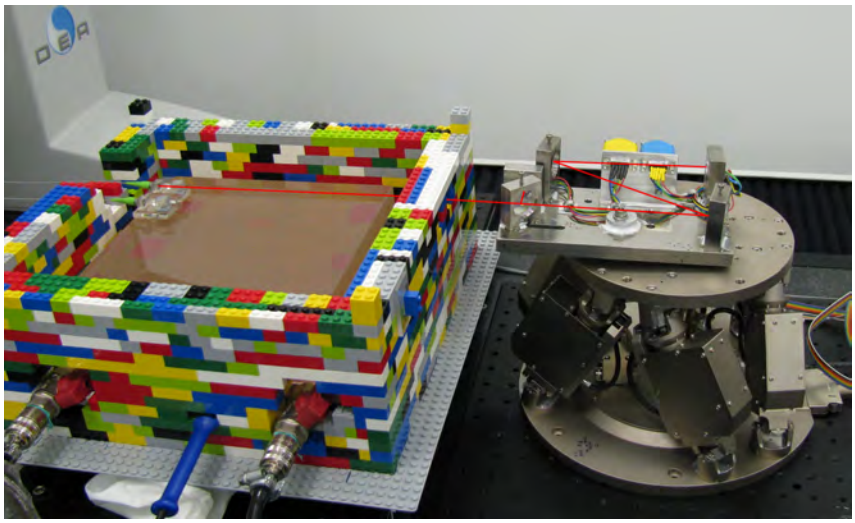

Figure 5.47: Photograph of set-up for beam pointing measurement.

a separated LEGO box. None of these attempts could decouple the complex temperature influence from the measurement of the beam pointing. They were all consistent with the beam pointing effects being due to the influence of thermal gradients in the air rather than internal pointing effect in the FIOS. The beam pointing at 20° C is within measurement uncertainties repeatable. Table 5.8 shows the measurements.

Temperature Date	FIOS1 height (mm)	FIOS1 delta z (μrad)	FIOS2 height (mm)	FIOS2 delta z (μrad)
20° C (15/04/09)	12.485	22	12.4855	-15
30° C (16/04/09)	12.489	43	12.492	10
40° C (17/04/09)	12.495	66	12.487	68
20° C (17/04/09)	12.485	18	12.486	18
Vibration and shock test: S2-UGL-TR-3016				
20° C (27/04/09)	12.483	26	12.487	-8
10° C (05/05/09)	12.492	-40	12.4925	-80
Thermal-vacuum tests: S2-UGL-TR-3017				
0° C (22/05/09)	12.491	-73	12.491	-133

Table 5.8: Beam pointing depending on temperature.

5.8 Fibre injector conclusions

The qualification process of the fibre injector was successful. The FIOS QM fulfilled vibration and shock tests, thermal vacuum tests, and operation tests at the required temperatures. Fused silica is suitable for this space application, furthermore the lens and PBS were proved to be radiation hard (chapter 2). Changes to the design have been implemented in terms of the mounting angle of the PBS. In the case of the flight model fibre injector the PBS is placed at an angle of 2°. The technique of FIOS mounting to the post was successfully tested and the necessary alignment precision was achieved. Tests have shown that the Diamond fibre connectors are critical items. For further missions which combine epoxy gluing and silicate bonding, design limits in thickness have to be followed such that no deformation of bondable surfaces appear as happened in the case of the lens carrier mount. Many aspects of the LTP fibre injector design can be further used or further developed for LISA fibre injectors. One critical aspect in the current LTP design is the fibre output which is very sensitive to contamination. A monolithic all-in-one fibre end to lens structure may be required for the LISA fibre injector.

Chapter 6

Proto-flight fibre injector models

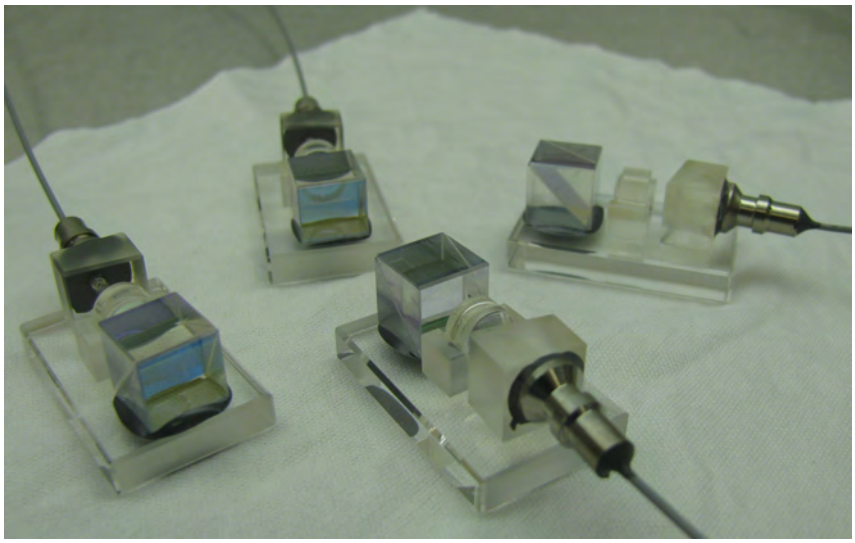

Figure 6.1: Photograph of the FIOS proto-flight models

In total four Fibre Injector Optical Subassembly (FIOS) were built for use on two optical benches for LTP. Two FIOS will be mounted on each bench onto the side of a FIOS mounting post that is bonded to the optical bench. One

optical bench will be the proto-flight model (PFM) and the other optical bench is the flight spare (FS) model. At the current stage no distinction is made between those two benches. The same designation is given to each of the pairs of fibre injectors. At the current stage no decision is made which pair will be assembled on which optical bench. To distinguish between the individual fibre injectors they are named after the labelling on the fibre connector: FM16a, FM11a, FM11b, and FM14b; where FM11a and FM16a form one pair, and FM14b and FM11b the other.

6.1 Optical performance tests of fibre injector

This section presents a summary of the optical performance tests of the fibre injectors after assembly before they have been attached onto the bench and after thermal cycling. For thermal cycling the FIOS were placed on a small clean room cloth on the heat plate in the thermally insulated LEGO box. Figure 6.2 shows a photograph of the set-up.

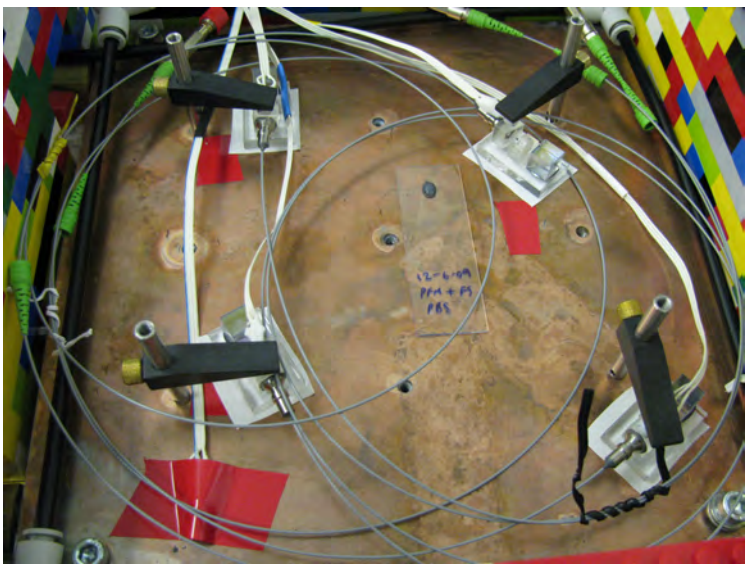

Figure 6.2: Photograph of the thermal cycling set-up.

Temperature sensors were clamped between the FMA and the holder. In total 20 cycles were carried out between 45°C (± 3°C) and 15°C (± 3°C). The thermal cycling took ~ 3 days. The temperature curve is shown in figure 6.3.

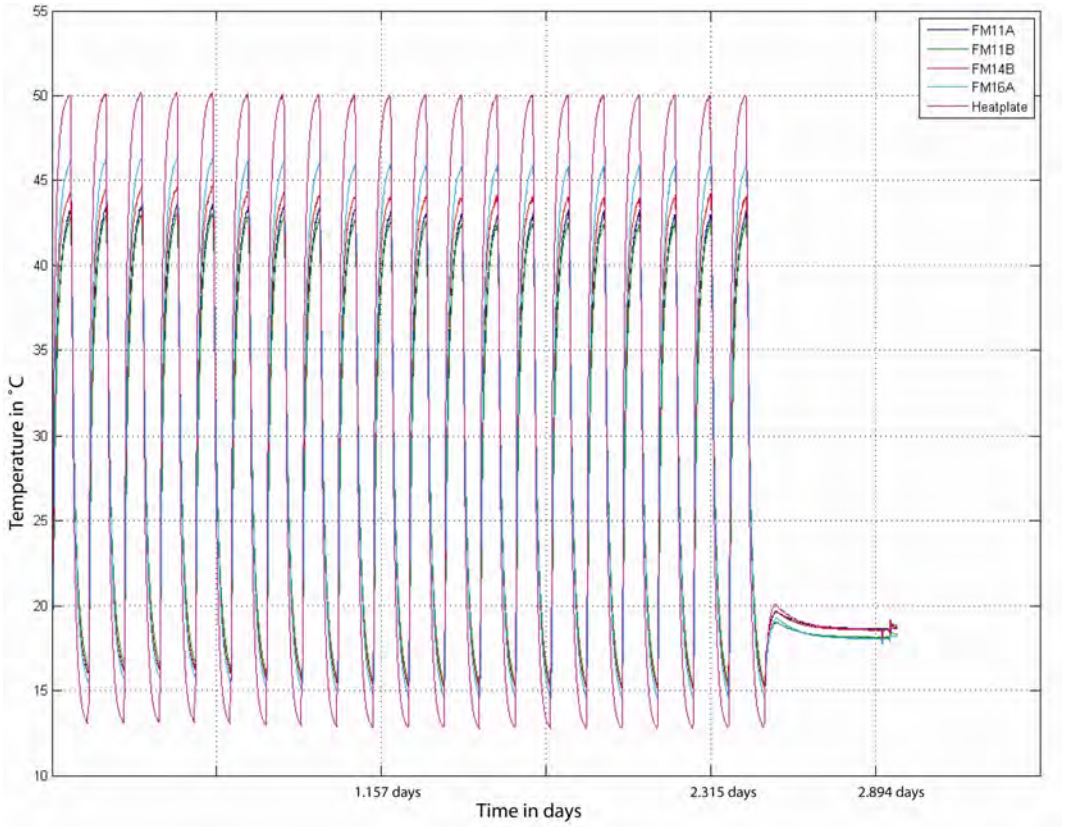

Figure 6.3: Temperature cycle of FIOS proto flight models.

6.1.1 Optical throughput

The optical throughput measurements before and after the thermal cycling were carried out using the same input fibre. All fibre ends were cleaned before measurement. The optical throughput measurement varies within measurement uncertainties. The results are shown in table 6.1. Optical throughput values of above 80 % have been finally reached as required.

	Optical throughput [%] before thermal cycle	Optical throughput [%] after thermal cycle
FM11b	74	89
FM14b	83	84
FM16a	81	89
FM11a	84	87

Table 6.1: Optical throughput measurements.

6.1.2 Polarisation

The angle of the linearly polarised light exiting the FIOS was measured with respect to the FIOS baseplate by using the minima of the optical throughputs of the PBS. The measurements are repeatable within measurement uncertainties. Results are shown in table 6.2. No effect of temperature can be observed in terms of polarisation measurements.

	Polarisation before thermal cycle	Polarisation after thermal cycle
FM11b	$3° \pm 2°$	$3.5° \pm 2°$
FM14b	$2° \pm 2°$	$1° \pm 2°$
FM16a	$1° \pm 2°$	$2.5° \pm 2°$
FM11a	$2° \pm 2°$	$2° \pm 2°$

Table 6.2: Comparison of polarisation after and before thermal cycling.

6.1.3 Beam geometry

The beam diameter and ellipticity were measured at 5 cm steps along a rail using a CCD beam profiler (WinCAM). The closest measurement point was ~ 8 cm from the FMA (Fibre Mounting Assembly) fibre output. In figure 6.4 the beam diameters of all four fibre injectors are plotted having the same distance to the FMA. Where FM11a and FM16a form one pair and FM14b and FM11b are the pair on the other bench. The violet marked line in figure 6.4 marks the distance of the combination of the frequency interferometer. The vertical extent of the line symbolises the requirement of the beam size (1000 – 1300 microns). The analog figure 6.5 shows the matching of beam diameter for both pairs in the case of interferometers of unequal path lengths (~ 36 cm). The recombination points of the reference, the X1, and X1 – X2 interferometer are within the marked violet box, which illustrates the requirements of the beam size.

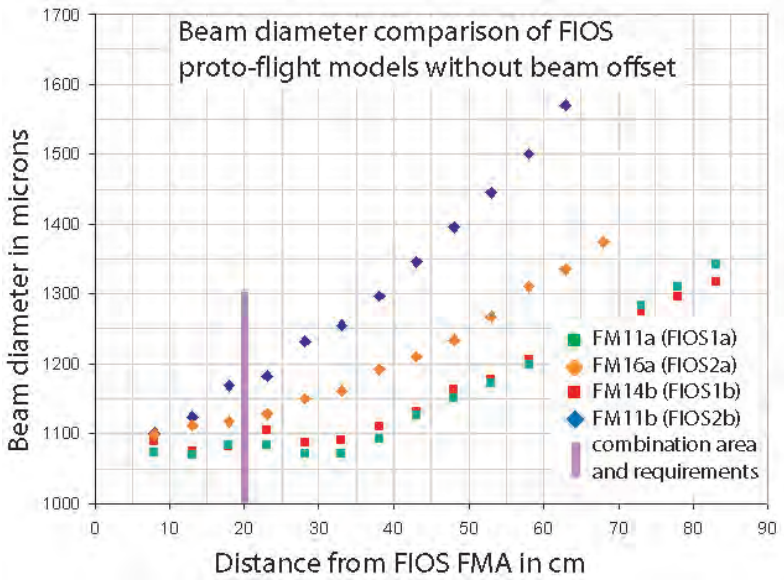

Figure 6.4: Beam diameter of the four fibre injectors without an additional pathlength difference for FIOS2 fibre injectors.

The fibre injectors FM11a and FM14b are very similar; both are designed to function as FIOS1 on their optical bench. FM11b and FM16a (FIOS2) are less similar. FM14b and FM11b form one matched pair with beam diameters ratios of beam diameters that falls between 1.01 and 1.06. Analog the ratio of the second pair FM11a and FM16a lies between 1.02 and 1.08. These fulfill the requirement that the ratio should be < 1.2 so that a contrast of $> 80\,\%$ can be achieved.

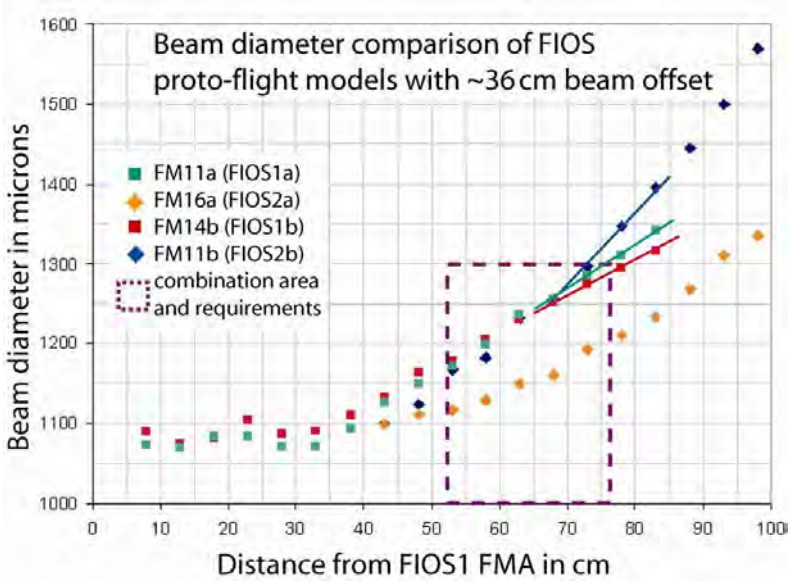

Figure 6.5: Beam diameter of the four fibre injectors with an additional path-length difference of ~ 36 cm for FIOS2 fibre injectors.

In the graph of figure 6.4 is also shown that the beam from FM11a expands faster than the beam from FM16a. However, the beam sizes (marked in violet) at the combination points of the OBI without an offset are well within the requirements.

In the graph figure 6.5 the beam size of FM11b, FM11a, and FM14b are at the upper limit or just a bit above of the requirement of 1300 microns. A fit through the measurement points shows this of FM11b, FM11a and FM14b.

FM11b has a beam size of ~1325 microns at a distance of 76 cm. This is ~2 % above the requirement. Due to the distance uncertainties of beam profiler and the read-out of the beam size it can be assumed that the measurements having an uncertainty of a few percent. So that the beam diameter of FM11b can be accepted for the use as a PFM or FS fibre injector.

6.1.4 Relative wavefront quality and interference contrast

The interference quality of the pair FM11a and FM16a was measured to be 93 ± 3 %. It was noticed that the laser was running slightly in multimode. After correcting this, the interference for the other pair was measured to be 97 ± 3 %. After thermal testing a contrast for both pairs of ~95 ± 3 % was achieved.

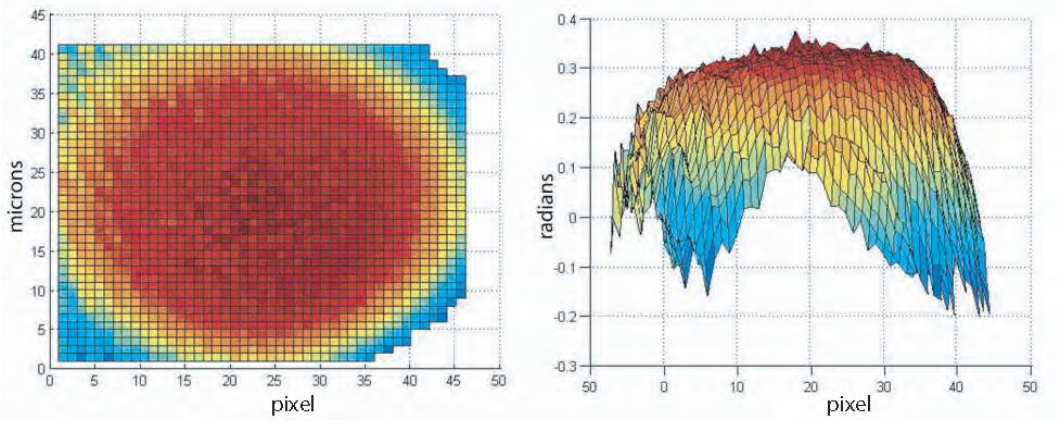

Figure 6.6: Two 2D plots of the same combined wavefront quality of FM14b and FM11b. The left graph shows a top view of the beam, the right graph a side view.

Figure 6.6 shows two 2D plots of the relative wavefront quality, where the optical beams from FM14b and FM11b interfere. Although the beam is circular,

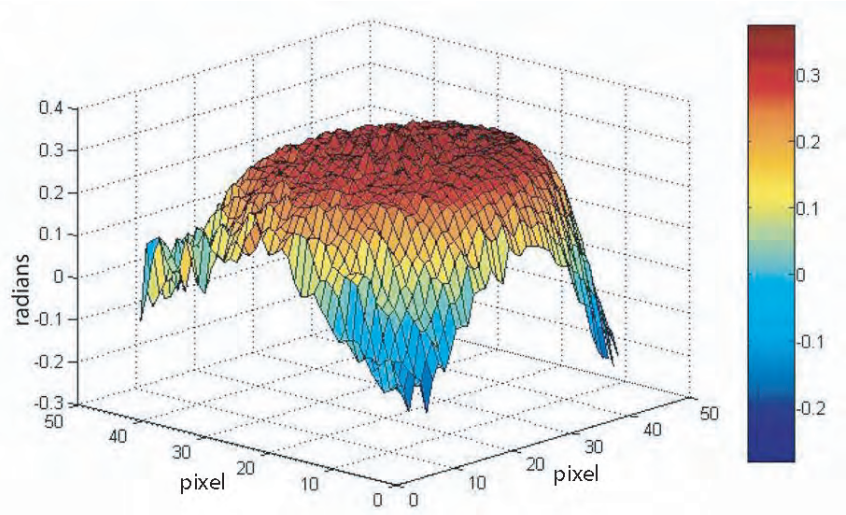

Figure 6.7: 3D plot of combined wavefront quality of FM14b and FM11b.

the InGaAs camera provides a square measurement area, shown on the left hand side of figure 6.6. The right hand side plot shows the phasefront difference between the two wavefronts (in radians). The phasefront variation across the centre of the beam is ~ 0.03 radian, which is equivalent to $\sim \lambda/200$. So the wavefront matching of the combined beams is very high. On the flanks of the plot, wavefront difference is in the range of $\lambda/20$. Figure 6.7 shows the plot in 3D. In the plots one pixel is equal to 30 microns.

Figure 6.8 shows the 3D plot of the combined relative wavefront quality of FM11a and FM16a. The quality is within $\lambda/10$ over the entire beam diameter with better than $\lambda/30$ in the centre of the beam. One pixel is equal to 30 microns. The peaks in the top right quarter are due to sensor noise and are not part of the beam measurement. After thermal cycling of the FIOS the relative wavefront measurement of both pairs were repeated and showed the same results, therefore no influence of thermal cycling was observed.

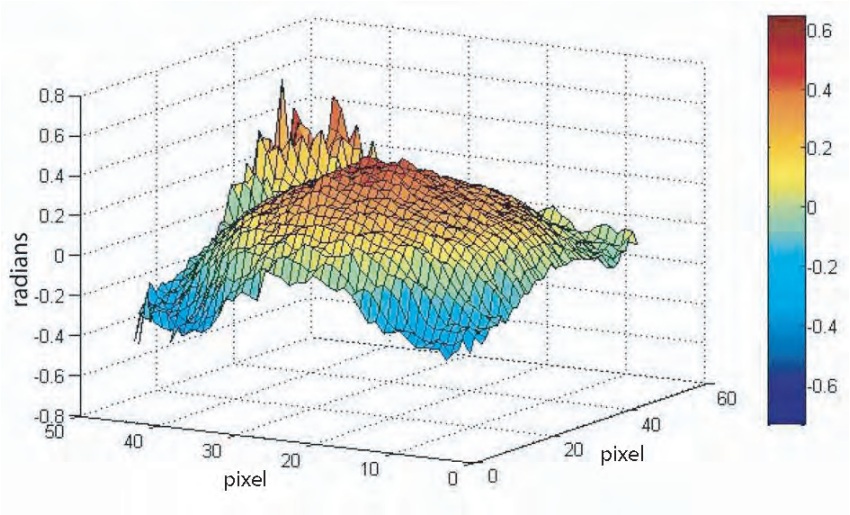

Figure 6.8: 3D plot of combined wavefront quality of FM11a and FM16a.

Both FIOS pairs fulfil the given requirements and the thermal cycle does not influence the performance of them. The relative wavefront quality show a very good beam match for both FIOS pairs. Further information can be obtained from the LTP document [54]. The placement of the fibre injectors onto the optical bench is in preparation. This will be performed as described in section 5.2.

Chapter 7

Summary and Outlook

This chapter presents a summary of the work presented in this thesis and gives a summary of outstanding work for the LTP project. In addition a discussion of forthcoming optical bench work relating to LISA is presented and certain parallels between these projects are made.

7.1 Summary

The interferometry for the LTP and LISA missions requires optics and materials that fulfil the requirements (see section 4.3). The optics have to be mountable in a stable way, and the optical properties have to remain stable over the lifetime of the mission. In the case of LTP and also LISA the philosophy is to attach the optical components directly onto an optical bench. In both cases the material for the bench is chosen to be Zerodur because of its low thermal expansion properties and because glass optics can be directly silicate bonded onto the bench. Silicate bonding has been proven to be a highly

stable way to mount the optics. Wherever it is possible, fused silica is used for the optics to which optical coatings are applied. Occasionally, other materials are required e.g. for lenses and half wave retardation plates for LISA. These materials must also be subject to tests like irradiation hardness tests. This thesis presented the successful irradiation test for the material ECO550 which is a common material for moulded lenses. Also the radiation hardness of the optical coatings of mirrors, 50:50 beamsplitter and anti-reflection coating for 1064 nm wavelength optics were successfully investigated. The procedure to qualify a material in terms of irradiation damage using Nd:YAG measurements and spectrophotometric measurements has also been presented and can be adapted for other materials.

The assembly of the FIOS QM on the prototype bench was an important first step for the LTP optical bench construction. The alignment of the FIOS on the bench is the most critical alignment stage. The prototype bench will be built a step ahead of the proto-flight and flight-spare optical bench, so that experience can be gained during construction and alignment tools and jigs tested. In particular the CMM programs for positioning templates and the CQP target device can be verified.

Furthermore, the qualification tests of the LTP FIOS design were successful. The LTP FIOS design fulfil the required vibration and shock levels and also the thermal cycling. Currently the proto-flight and flight-spare FIOS are assembled.

7.2 Outlook

Since LISA interferometry uses the same wavelength, the proven coatings can be directly applied in LISA. In addition to fibre injectors optical devices on the LISA optical bench – e.g. the focusing elements used with the detectors – contain lenses. It is recommended to use ECO550 or ideally lenses made from fused silica. The LISA FIOS design will be different to the LTP FIOS; the beam size from the FIOS on the LISA optical bench will be a factor ~two larger than on the LTP optical bench, therefore other lenses as part of the fibre injector have to be chosen.

Once the prototype bench is constructed it also provides a test bench for aligning the photodiodes. The positioning and gluing of the photodiodes on the optical bench will be carried out under the responsibility of the University of Birmingham in the LISA lab at Glasgow. Jigs and alignment tools have not yet been tested and using the prototype bench as a test bench for the assembly of the photodiode will be very useful. It is proposed that one or two LTP photodiodes are placed on the prototype bench for this purpose.
Finally, the prototype bench will be relocated to the Albert Einstein Institute (AEI), Hannover. The AEI will conduct final tests involving the flight hardware: optical bench, phasemeter, laser and modulation unit. It is planned that the prototype bench will be used for setting-up these tests. After the test agenda is finished, the prototype bench will provide an on-ground 1:1 model of the actual flight optical bench, allowing further investigations of LTP interferometry. Furthermore it provides an ultra-stable test bench for any other tests where high stability interferometry is required, e.g. reflective optics could be tested by placing them at the location of the test masses in the prototype bench design.

The current FIOS design is sufficient for LTP but in the case of LISA further modifications have to be made. The fibre injectors are a single point failure, and this is a concern for space missions. For LISA two fibre injectors will be present for each beam, with a fiber switching unit to select the active one. Also the design of the fibre injector will be optimised for a longer lifetime – LISA has an operational phase of ten years compared to six months in the case of LTP, and this results in a much higher risk of contamination of optical surfaces. In particular the fibre output face in the current LTP fibre injector would be at high risk, due to its small size of four microns radial optical output. The air gap between the fibre output and lens has to be avoided using a customised fused silica spacer in between so that the beam expands into a silicate bonded fibre output-lens design. For a FIOS design with beam expansion in silica further investigations of beam disturbance passing through a silicate bonded boundary have to be carried out. Investigations of the reflectivity of silicate bonded boundaries are currently being conducted by the LISA team Glasgow.

LISA consists of three satellites, each housing two optical benches. It can be assumed that including spares, at least ten LISA optical benches will be built. This number of benches, combined with their larger size, raises logistical issues. Currently silicate bonding is a highly skilled manual operation. Investigations of automatic bonding tools using precision alignment equipment are planned. Further ongoing research in the Institute for Gravitational Research includes investigations of using other materials for silicate bonding. Also, investigations of other applications are being carried out (see appendix B) – e.g. for the project Extra Large Telescopes (ELT).

Appendix A

How to clean a capillary

A previous design of the FIOS FMA included the use of capillaries. Therefore an investigation on how to clean a capillary for silicate bonding was done. In doing so the capillary was cleaned in an ultra-sonic bath containing a soapy solution. The remaining water and soap residue have to be removed from the outside as well as the inside of the capillary. This technique will be described in following section.

Water remains inside a capillary due to capillary action. This water has to be removed in such a way that no film is left over at the capillary walls. The inner diameter of the chosen capillary is 127±3 μm only, therefore shaking or knocking out the water is not possible, so the author used another technique shown in figure A.1. For the purpose of explanation it is assumed that the water is in the middle of a capillary. The capillary is held vertically in a petri dish containing methanol. The methanol will be sucked into the capillary by capillary action until the water reaches the top of the capillary. Between water and the methanol there will be an air gap of the size of the original air gap between water and bottom of the capillary. The height of the methanol will be limited by the air gap between the water and the top of the capillary. The

aim is to suck in so much methanol, that the methanol is sucked in above the original water level. Afterwards the bottom of the capillary is contacted to a clean cloth. The cloth sucks out the methanol from the capillary; due to capillary action the water follows the methanol down in a distance of the air gap, as soon as the water reaches the maximum level of the methanol, the water does not stay onto the walls of the capillary but continues to run down along the wall until it gets sucked out by the clean cloth. In such a way a capillary can be emptied. The author assumes that residua of the methanol remains on the wall and weakens the surface tension of the water such that it can run along the wall of the capillary disregarding the capillary action.

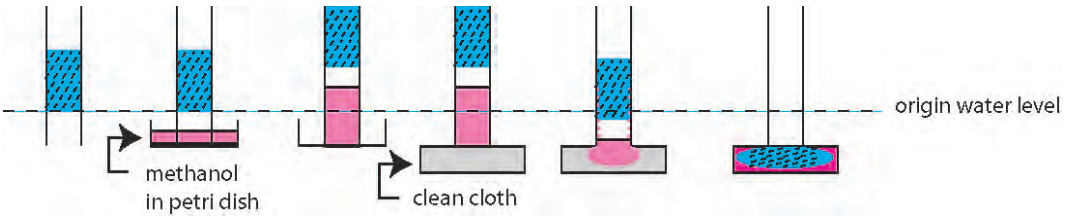

Figure A.1: Process to remove water inside a capillary.

Afterwards the empty capillary will be cleaned with methanol using the capillary action to suck it in and a clean cloth the suck it out. Experiments have shown that in such a way prepared capillaries are bondable to a close fit fibre core with a diameter of 125 μm.

Appendix B

Theory of silicate bonding

B.1 Chemistry of silicate bonding

This chapter describes the technique of silicate bonding. Silicate bonding is a room temperature technique which joins together extremely smooth and even surfaces, so that it forms a quasi-monolithic structure with the highest achievable mechanical and thermal stability compared to other bonding techniques. In doing so a so-called bonding solution is applied between both surfaces. The bonding solution is a water-based sodium silicate solution, containing 17 % SiO_2 and 14 % NaOH. Every material which can hydrate and dehydrate, can be theoretically be silicate bonded. Fused silica and Zerodur are common materials for silicate bonding for our applications. Therefore this chapter will explain the chemical effect of silicate bonding using fused silica as the material to be joined.

B.1.1 Introduction

Silicate bonding was developed by Jason Gwo at University of Stanford in the 1990's. Silicate bonding is patent pending (US-patent 6,284,085 B1). First application of silicate bonding was the space-mission Gravity Probe B. Also there are ground based applications such as the ground-based gravitational wave detectors GEO600 and LIGO. GEO 600 and LIGO are using optical systems suspended in a pendulum system. The lower optical mass is connected to the top mass by glass fibres, which are welded onto so-called ears. These ears are silicate bonded on the sides of the masses. Figure B.1 shows the beamsplitter in the GEO600 set-up. The ears can be seen on the side of the beamsplitter, they are made of fused silica like the beamsplitter substrate. Using the same material a monolithic pendulum suspension can be maintained with extremely low mechanical loss.

Silicate bonding is an on-going research field looking for new applications as well as investigations into other bondable materials.

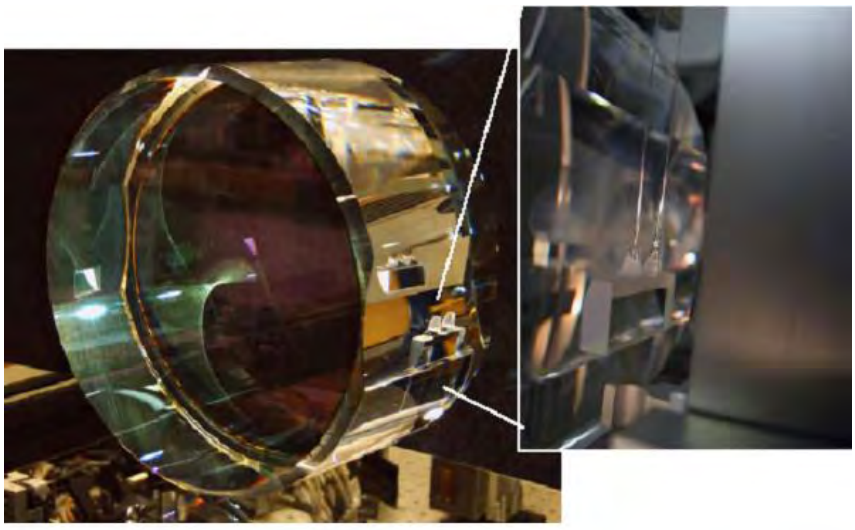

Figure B.1: Pendulum suspension for GEO600.

Silicon is an element of the fourth main group of the Periodic Table. It can therefore form four atomic bonds. The pure form of silicon forms a crystalline diamond-like tetrahedral lattice structure. Silicon easily forms bonds with oxygen in doing so it forms silicon dioxide (SiO_2). One silicon atom is surrounded by four oxygen atoms forming a tetrahedral lattice structure using single bonds. Silicon oxide can be found in nature in pure form as rock crystal. The material fused silica also consists of pure silicon oxide.

B.1.2 Optical contacting

Optical contacting can be seen as a first step before silicate bonding can take place. Silicate bonding has a stronger bond than optical contacting due to building strong chemical bonds in comparison with the weaker intermolecular forces in optical contacting.

The following description of optical contacting is obtained from [55]. In the case of two extremely smooth and clean polished surfaces of better than $\lambda/10$ ($\lambda = 633\,\mathrm{nm}$) global roughness, in direct contact optical contacting takes place. In doing so the interaction between both surfaces is caused by van der Waals forces. Van der Waals forces are weak intermolecular forces between atoms or molecules. Due to dipole properties in the lattice neighbouring atoms or molecules influence each other. In the case of an optical contact it happens that along the smooth and polished surfaces atomic connection points are formed over the contacted surface. Both surfaces are within atomic distance of each other so that the van der Waals force can interact between them. The contact potential of two extremely smooth surfaces facing each other is given by [55]

$$w(D) = -\frac{A}{12\pi D^2} \tag{B.1}$$

In equation B.1 above, A is the so-called Hamaker constant, $A = \pi^2\rho\rho' C$, where C is the interaction constant measured in $\mathrm{J\,m^6}$, and ρ und ρ' are the numbers of particles per unit volume on the surfaces. D is the distance of separation of the surfaces. In the case of the same material ($\rho = \rho'$) the interaction is simply given by $P(D) = \frac{\delta w(D)}{\delta D}$ (bonding strength in the form of pressure) from which we derive $P(D) = \frac{\pi\rho^2 C}{6\pi D^3}$. The Hamaker constant for most material is in the range of 10^{-19} J and in case of fused silica A $\approx 0.6 \times 10^{-19}$ J. Typical values for P are quoted in the range of $5 - 20 \times 10^5$ Pa. Interpreting such pressure as the results of van der Waals interactions, the range of D is 1.2 - 1.9 nm. [55].

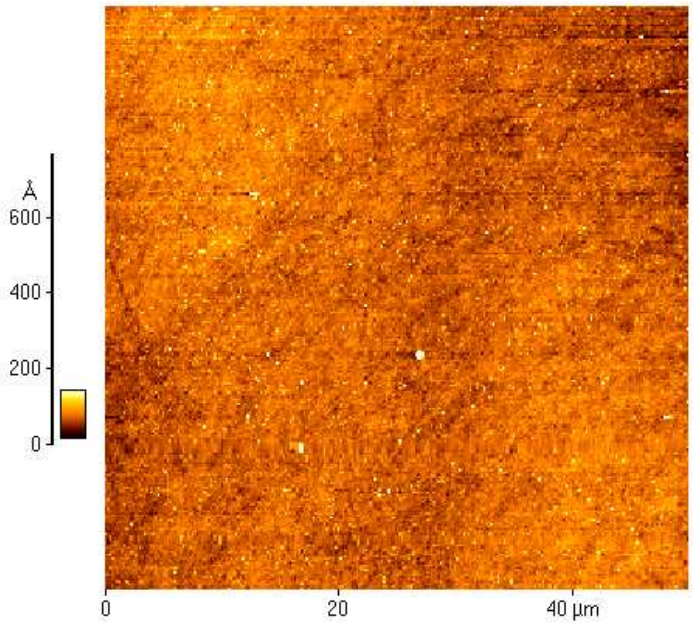

Figure B.2: Atomic force microscope scan of a $\frac{\lambda}{10}$ polished surface of a $50 \times 50\,\mu\mathrm{m}^2$ area with a peak to valley value of pv = 12 nm.

Figure B.2 shows a AFM scan of a polished surface. In the case of a surface polished to $\frac{\lambda}{10}$ measurements have shown that the roughness of the surface is in the range of few nm. Optical contacting will only apply at the contact points of both surfaces up to a distance of 1.2 - 1.9 nm, as shown before. In using the

silicate bonding technique this distance can be bridged.

B.1.3 Hydroxide catalysed dehydration

Silicon oxide is a material which hydrates and dehydrates, that means it is capable of bonding and releasing hydrogen atoms on its surface. This mechanism is catalysed through OH^- ions. Figure B.3 illustrates that.

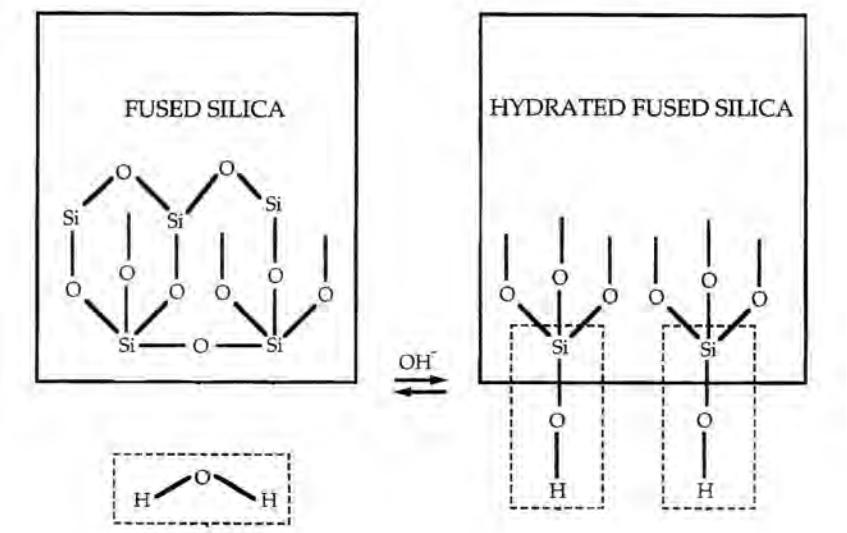

Figure B.3: Schematic drawing of hydration und dehydration of fused silica [5].

Silicon oxide hydrates, catalysed by the OH^-ions produced by dissociation of water molecules in the atmosphere. Si-O-Si chains react with these OH^-ions on their surface. The Si-O-Si chain splits into a Si-O and a Si so that it can form Si-O-H and Si-OH with the existing water molecule. The chemical equations of hydration and dehydration are:

$$H_2O \quad \Leftrightarrow \quad H^+ + (OH)^-$$

$$Si - O - Si + H_2O \quad \overset{OH^-}{\Leftrightarrow} \quad Si - OH + Si - OH$$

At the surface of fused silica there is a chemical equilibrium.

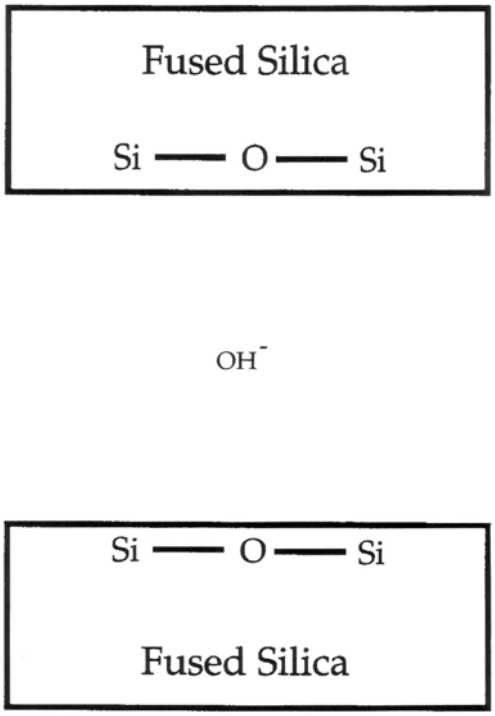

Figure B.4: Schematic drawing of the fused silica surfaces [5].

Two extremely smooth surfaces in direct contact at an atomic distance can contact with each other, shown in figure B.5 und B.6. Due to hydration and dehydration of the surfaces, they form Si-O-Si chains across the gap. Those chemical bonds are stronger than van der Waals forces.

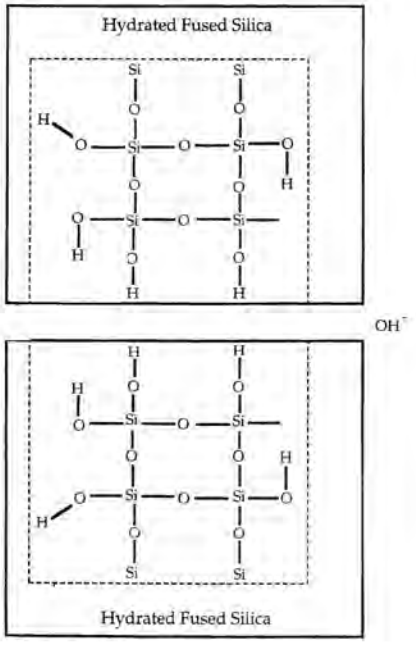

Figure B.5: Hydrated fused silica [5].

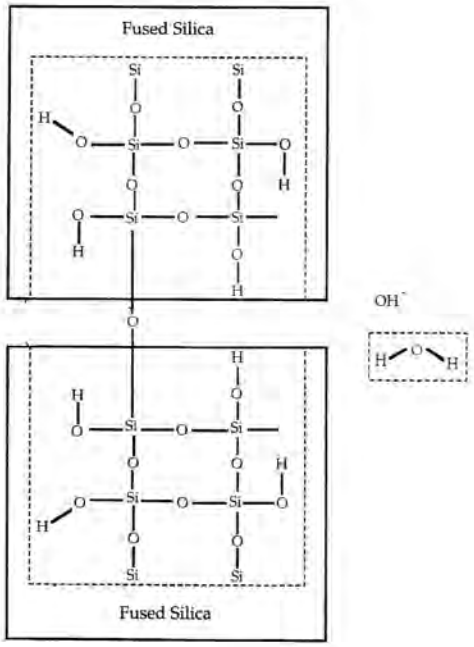

Figure B.6: Dehydrated fused silica [5].

In reality there is still a distance between both surfaces due their roughness as shown previously in the AFM scan. The atomic connections can not be developed over the total area. When an optical contact is first formed there are very few of the bonds shown in figure B9 and the bonding force is due almost entirely to van der Waals forces. But with the passage of time more Si - O - Si bonds form and the surfaces cannot be separated without damage.

A bonding solution is applied to fill up those gaps between both surfaces. The bonding solution contains dissolved silicon oxide and NaOH; that means that there are free OH^-ions in the solution, which act as a catalyser:

$$(NaOH \Leftrightarrow Na^+ + (OH)^-)$$

Figures B.7 and B.8 illustrate this action.

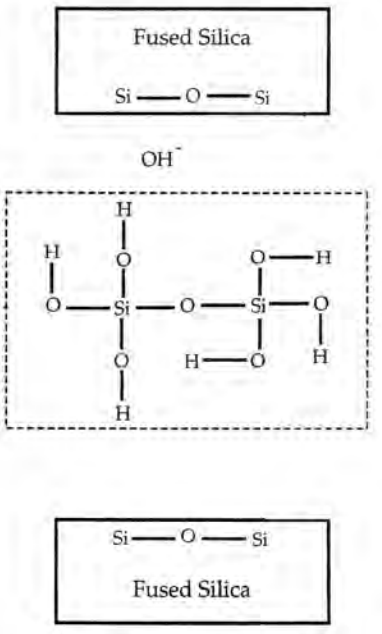

Figure B.7: Hydrated fused silica [5].

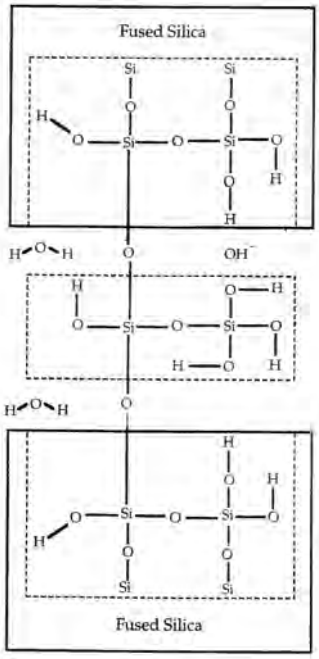

Figure B.8: Dehydrated fused silica [5].

Due to the process of hydration and dehydration Si - O - Si chains can form between the surfaces using the Si atoms of the bonding solution. The bonding solution acts like a bridge between the surfaces. At first the surface hydrates by catalysis of OH^-ions. With the splitting of water molecules the bond dehydrates and O - Si - O chains are left over. The bonding solution is a provider of Si for building chains between the surfaces and also produces OH ions for the catalysis process. After the bond is dried out there will be a bond of a approximate 100 nm thickness between the surfaces; in doing so it fills up the microscopic gaps between the surfaces.

The bonding process can be divided in two different steps; firstly the etching process in which OH^-ions etch the surface and hydration is taking place and secondly the bonding phase in which the bond dehydrates and forms O - Si - O chains between both surfaces. This chemistry is illustrated in the follow formula:

$$SiO_2 + OH^- + 2H_2O \Rightarrow Si(OH)_5{}^-$$

During the etching process $Si(OH_5)^-$ions are formed and release free OH^-ions. This causes the ph-value to fall below 11. Below pH 11 Silicate polymerises in the solution and the bonding process continues [26]:

$$Si(OH)_5{}^- \Rightarrow Si(OH)_4 + OH^-$$

Si-O-Si chains are formed, water evaporates and the bond sets.

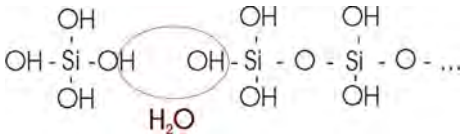

The time period for silicate bonding depends on the concentration of free OH^-ions. This time period during the bonding phase is called the setting time. The setting time is controlled by adjusting the pH value. A high pH will lead to a longer setting time because the pH has to fall below 11 before polymerisation occurs. During the etching phase it is possible to move both surfaces against each other, the time range for doing this is few minutes. Etching phase and bonding phase are not sharply defined therefore the possibility to move the surfaces towards each other decreases over the time of the bonding process. The setting time can also be influenced by temperature [56].

After the bond takes place, it takes a few weeks until the bond drys out completely. This time period can be speeded up by exposing the bond to a

temperature of about 40° C; one day at 40° C equals to one week curing at room temperature (20° C). Afterwards both surfaces form a quasi-monolithic structure with properties like a solid material. The strength of the bond can be measured by doing break tests. The quasi-monolithic structure will break at a weak place of the material, this will not necessarily be the bond. It can happen at any natural impurity in the material.

B.1.4 De-Bonding

During the bonding process it is still possible to separate both surfaces from each other. But the possibility of damaging the surfaces increases as the bonding process has time to set or even to dry out. The time limit of de-bonding also depends on the quality and size of the bond, but it can be said that a good bond cannot be removed without great damage after a few hours. The bonding process can be stopped by adding OH^-ions; this can be done by flooding the bond with water. Nevertheless if the bonding process has already taken place, the smooth bonding surface can be damaged and further bonds might not be possible or further bonds might be of poor quality. To disconnect bonded surfaces from each other the parts are placed in an ultra-sonic bath in a highly basic solution. The basic solution infiltrates between both surfaces and can disconnect the surfaces.

B.2 Silicate bonding of Silicon Carbide

Silicon Carbide (SiC) is a ceramic material with good mechanical and thermal properties, therefore it is very interesting for applications like future space missions. The chemical process of hydroxide catalysis bonding requires the

presence of a layer of oxide at the bonding surface. SiC does not include oxygen, unlike fused silica (SiO_2), hence it is important to create an oxide layer. For the oxidation process a furnace tube that generates temperatures up to 1000° C was used, shown in figure B.9. The high temperature forces the SiC to combine with the oxygen from the atmosphere and form a surface oxide layer. First oxidation experiments of SiC showed a very patchy appearing oxide layer, even when the unoxidised material showed a very smooth homogenous surface. For comparison SiC samples were also oxidised by colleagues in the department of mechanical engineering. However the oxide layer produced looks similar in all cases. Later oxidation runs have shown that the quality of the oxidation process depends on the homogeneity of the raw material. Results of bonding experiments of SiC can be found in reference [57].

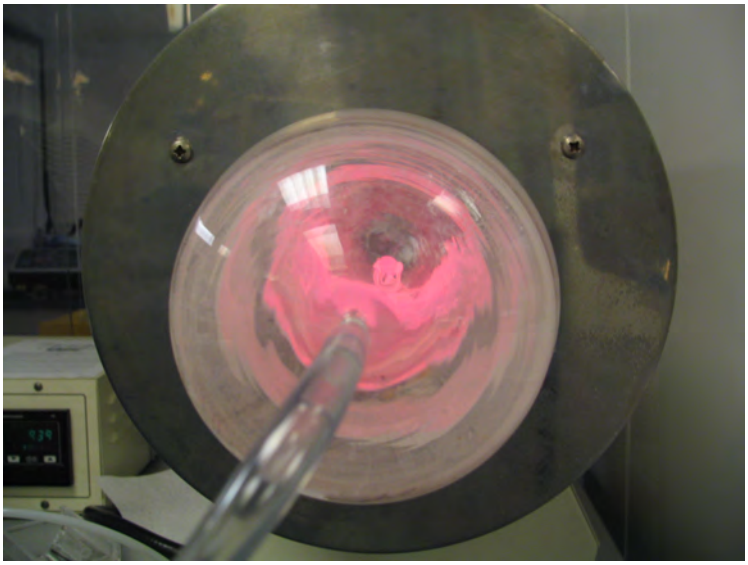

Figure B.9: Photograph taken during the oxidation process.

B.3 Silicate bonding beyond the norm

The Institute of Gravitational Research is interested in extending the hydroxide catalysis bonding technique to various other (possibly commercial) applications. The author therefore did further investigations of hydroxide catalysis bonding for several companies. The investigations covered fused silica material which is not as flat as the normal standard required for bonding. Also investigated were bonds of components of large area and of sub millimeter thickness, as well as very large components with a bonding area of over $100\,\mathrm{cm}^2$.

Fused silica pieces of different sizes have been bonded without the necessary surface flatness of $\lambda/10$ or better as required for silicate bonding. The flatness of the pieces were in the range of $\lambda/2$ to $\lambda/5$. We observed that the bond did not cover the entire surface. Dry spots were left at the edge of the bonding surface. The bond covered most of the area where the bond solution could form a bond between both surfaces. After three days no changes of this aspect were observable. Depending on the application, such a bond might be satisfactory compared to the costs of manufacturing a $\lambda/10$ surface. Furthermore this opens a new field for the use of certain kinds of glass materials which are very difficult to manufacture to a $\lambda/10$ surface finish.

Two very thin Zerodur plates with a bonding area of $100 \times 28\,\mathrm{mm}$ and a thickness of $0.8\,\mathrm{mm}$ were bonded. Due to the small thickness, a low stiffness was experienced which lets the substrate to flex. This allows the bonding solution to be squeezed by hand pressure with a wiping motion to remove air bubbles and spread the solution evenly. The bonding force is so large that both surfaces form a bond in which the plates conform. Figure B.10 shows a photograph after the bond is fully cured. In the right hand top corner a “dry” area is seen where the plates have separated. Beside the left hand bottom corner of the

labelling #01 a circular fringe pattern is seen. This fringe pattern indicates that a dust particle is trapped between the surfaces which prevents the surfaces from bonding. The possibility of a trapped dust particle increases with the surface area of the bond. It does not effect the bond in general and a good bond has been achieved over the central area.

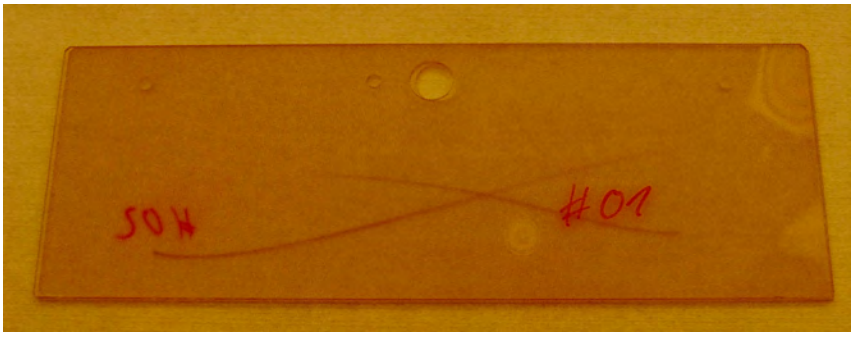

Figure B.10: Photograph of two $100 \times 28 \times 0.8$ mm bonded substrate.

In the case of a thin 0.5 mm sapphire plate bonded to a thick glass prism with a flatness of $\lambda/7$ (bonding area 20×15 mm), it was found more difficult to squeeze out trapped air bubbles. These are shown in figure B.11 on the left hand side. On the right, another sapphire plate shows deformation which can be observed as stress in the material indicated by the fringe patten.

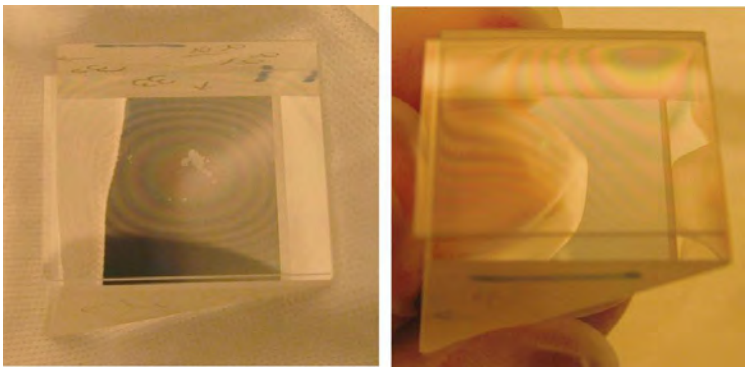

Figure B.11: Photograph of two bonds of thin sapphire substrate to a glass prism.

As well as large area thin substrates, very large and thick Zerodur discs have been bonded. The bonding area had a dimension of 118 cm^2 with a diameter of 12.3 cm and a thickness of 3 cm. A flatness of $\lambda/11$ for both bonding surfaces was measured. Figure B.12 shows the measurement of one of the samples (the measurement for the other sample is similar).
The bond covered ~ 95 % of the bonding area. At the edge of the bond dry spots were observed. This is linked to the way in which the substrate was polished; typically the flatness of large surfaces is only defined up to 5 mm to the edge of the surface. Such dry spots normally appear in this region. Figure B.13 shows the finished bond. A zoom-in of the dry spots is shown in figure B.14. The rainbow - coloured region indicates the dry spots along the disc edge. The company carried out tensile load tests and measured a bond strength of 2.5 MPa, which is in the range of previous measured values [26].

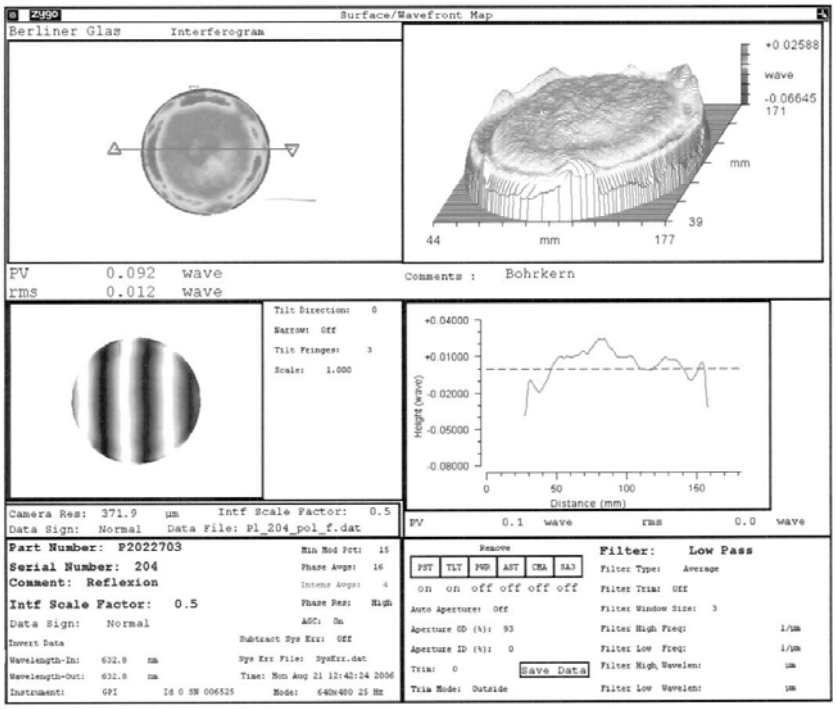

Figure B.12: Flatness measurement of a 12.3 cm diameter Zerodur disc.

B.4 Silicate bonding of fused silica cleaned in a "non – standard" way

This section summarises the experiment carried out to silicate bond samples that were UV – cleaned. The Extra Large Telescope (ELT) project requires bonds of material which are not suitable for the standard cleaning process for silicate bonding. The material geometry does not allow cleaning with a chemical substance. Residual contamination could remain within the material gaps. Therefore another method of cleaning surfaces was investigated. Fused silica test discs with a diameter of 25 mm were exposed to UV-light directly before bonding them. UV light is commonly used to sterilise surfaces by destroying long chains of molecules. This section will report on the cleaning procedure used and will present the results of shear break tests of the bonded samples.

Figure B.13: Photograph of two bonded 12.3 cm diameter Zerodur discs.

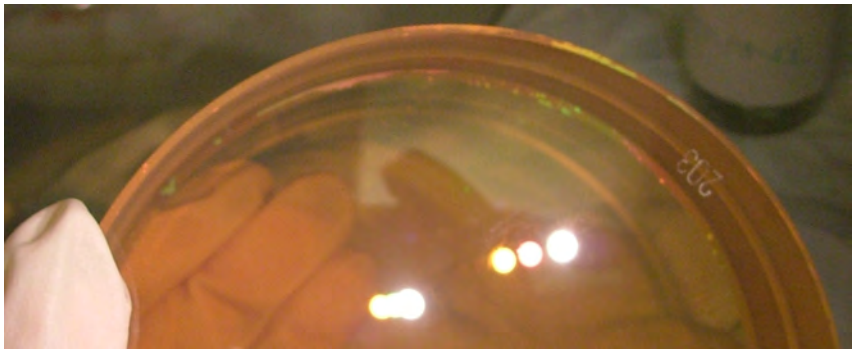

Figure B.14: Photograph of dry areas at the edge of the bond.

B.4.1 Preparation of tests samples

All fused silica test discs (22 in total) were used straight out of the package from the supplier. From these 18 discs where placed inside a UV – light exposer box. To maximise the UV light exposure aluminium foil was spread on the bottom of the box. The box houses two UV – C bulbs with a wavelength of

265 nm. Each of the bulbs has a power of 18 Watts. In total 18 discs were placed inside directly on top of the foil. Ten discs (two rows of five discs) were placed at equal distances from each other; in addition two sets of four discs were stacked on top of each other. In such a way covered surfaces were bonded. This was done to investigate a possible effect of contamination within the box. The discs were exposed to UV – light for six hours. After UV – light exposure the discs were wiped with isopropanol. Directly before bonding the bonding surface was dehydrated by wiping with clean methanol. The bonding solution was prepared using the standard procedure. The solution was applied using one drop of 2 μl on one of the discs. The other disc was then placed on top. The bonding solution spread equally between both surfaces. As usual both discs were movable for 30 – 60 seconds until the bond took part.
It was observed that air bubbles appeared between the surfaces (except in one sample). These air bubbles normally disappear during bond curing. However, this was not be observed this time. Figure B.15 shows two photograph of typical observed air bubbles. All discs are bonded well together, apart from sample 5. During the attempt to remove a bigger air bubble by sliding the top piece a bit over the edge - the top piece stuck at the edge and large force was needed to realign the top discs to the bottom one.
Besides bonding the samples after being exposed to UV – light two bonds of four non-cleaned discs were also performed. All bonds cured at room temperature for six days and a further seven days in an oven at 40 °C to speed up the curing process. In total eleven bonded samples were made.

B.4.2 Shear force measurement set – up

Shear force measurements were carried out using a commercial pulling machine that can pull up to twenty five tonnes. The bonded sample is clamped inside

Figure B.15: Photographs of two samples directly after bonding. The rainbow – coloured reflections are indicating air bubbles within the bonded surfaces.

a two-part jig. Each side of the jig is attached to a mount which is attached to the pulling machine. Figure B.16 (left hand side) shows the set-up attached to the pulling machine, on the right hand side the two-part jig with a sheared sample inside is shown. The jig is slightly larger than the samples; black electrical tape was applied around the sample to increase its size and also to even out high stresses as much as possible. A pull linkage was cut into the tape where the bond is located.

B.4.3 Results

The edge of sample 1 and sample 2 broke inside the clamp: a universal joint was attached to one side of the mount to allow easier excess to the set-up, but this led to an angular movement of one part of the jig, with the result that the sample was bent inside the jig and broke along its edge. The universal joint was removed leaving lateral movement possible. In this state the measurements of samples 3 to 11 were taken. The results are shown in figure B.17. The bond of sample 5 failed at very low force (not shown in figure B.17). This is due to the problems during bonding. It is assumed that the discs were not bonded over most of the surface. By realigning the discs force was applied.

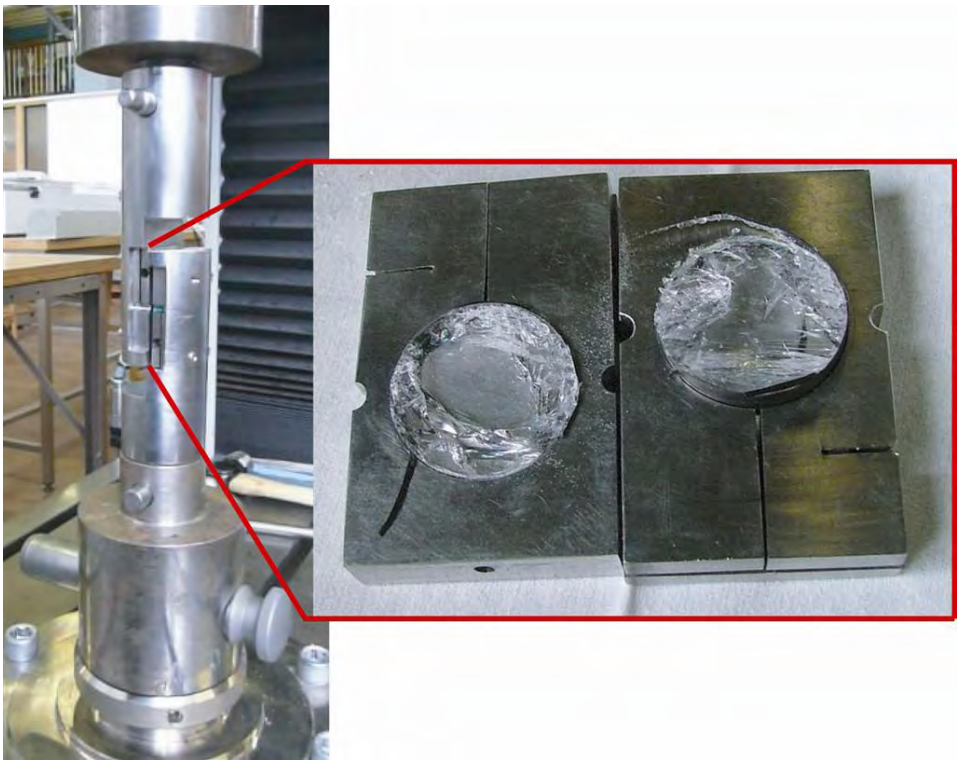

Figure B.16: Left: the shear mounting structure inside the pulling machine. Right: the bonded test sample after shear test inside the jig.

This indicates that either the bonding solution was contaminated or that there was not enough bonding solution left on the surface such that the discs could not move smoothly above each other. This may have happened, when the top discs was moved to far over the edge of the other discs.
At the bottom part of the curves, shown in figure B.17, some margin can be observed in the sample clamping and the jig. The upper part of each curve shows a similar gradient. No difference can be seen between UV – light cleaned samples and non UV-light cleaned samples (sample 10 and sample 11). Table B.4.3 summarises the results. An average bond force of 16.92 MPa was measured in shear tests.

Figure B.18 shows a photograph of one of the samples after testing. All suc-

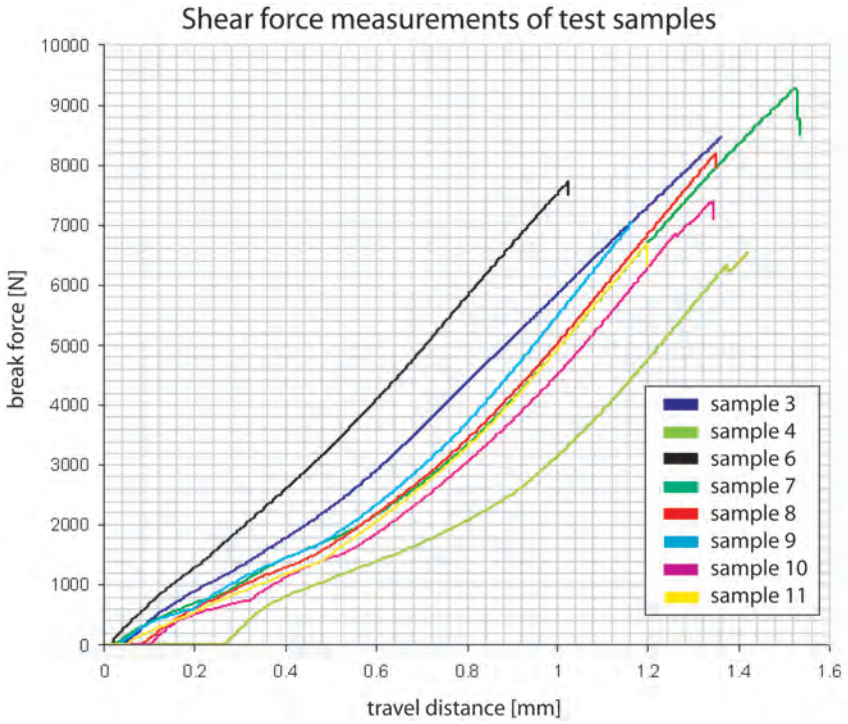

Figure B.17: Measurement curves of shear tests of silicate bonded samples.

cessfully tested samples were shattered over the entire surface – mostly only kept together by the surrounded tape. This indicates that the bond is not weaker than the raw disc material. Due to the fact that all samples are showing a similar break force within ~11 %, it can be assumed that during UV – light cleaning no contamination of the samples happens. Further bonding tests using samples of the material for the ELT project are necessary before a finial statement can be given concerning UV – light cleaning.

sample number	total measured break force [N] of 5 cm^2 bond	bond force in MPa	description
sample 1	1822	—	sample broke in the clamp, bond was not effected
sample 2	2400	—	sample broke in the clamp, bond was not effected
sample 3	8460	16.9	dark blue curve
sample 4	6546	13.1	light green curve
sample 5	39.5	—	bond failed
sample 6	7736	15.5	black curve
sample 7	9299	18.6	dark green curve
sample 8	8191	16.4	red curve
sample 9	7051	14.1	light blue curve
sample 10	7410	14.8	violet curve
sample 11	6692	13.4	yellow curve

Table B.1: Summary of the results.

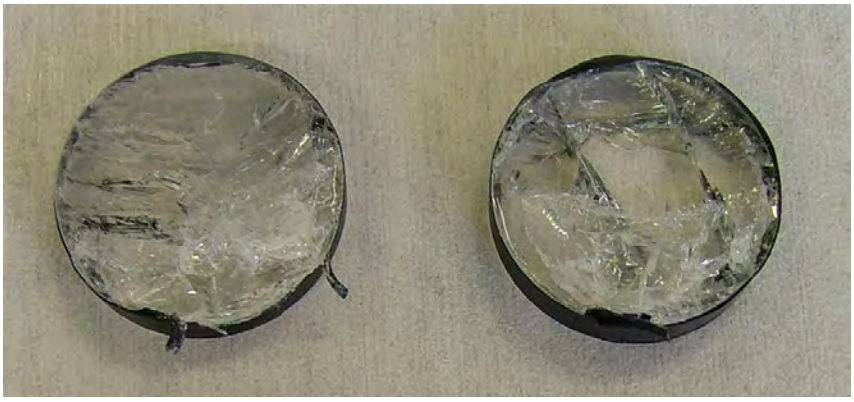

Figure B.18: Photograph of one of the bonded samples after testing.

Bibliography

[1] K. Danzmann and the LISA Study team. *LISA – Laser Interferometer Space Antenna: A Cornerstone Mission for the Observation of Gravitational Waves. ESA – SCI*, 11, 2000.

[2] LISA Studt Team. *Pre-Phase a report, second edition.* July 1998.

[3] M. Cerdonio *et al. Acoustic GW detectors in the 2010 timeframe. Class. Quantum Grav.*, 20:p23 – p29, 2003.

[4] LTP Project document:. S2-UGL-TP-3015 Fibre Injector Optical performance tests. January 2009.

[5] US Patent 6,284,085 B1. *Ultra precision and reliable bonding method.* 1997.

[6] Albert Einstein. *Prinzipielles zur allgemeinen Relativitätstheorie. Annalen der Physik*, 55:p125 – p138, 1918.

[7] R. A. Hulse and J. H. Taylor. *Discovery of a pulsar in a binary system. Astrophys. J.*, 195:p51 – p53, 1975.

[8] J. H. Taylor, R. A. Hulse, L. A. Fowler, G. E. Gullahorn, and J. M. Ranking. *Further observations of the binary pulsar PSR 1013 + 16,. Astrophys. J.*, Volume 206:p53 – p58, 2000.

[9] N. A. Robertson. *Laser interferometric gravitational wave detectors. Class. Quantum Grav.*, 17:p19 – p40, 1976.

[10] Masaki Ando and the TAMA collaboration. *Current status of TAMA. Class. Quantum Grav.*, 19:p1409 – p1419, 2002.

[11] B Willke for the LIGO Scientific Collaboration. *GEO600: status and plans. Class. Quantum Grav.*, 24:p389 – p397, 2007.

[12] F Acernese *et al. Status of Virgo. Class. Quantum Grav.*, 21:p385 – p394, 2004.

[13] Samuel J Waldman for the LIGO Science Collaboration. *Status of LIGO at the start of the fifth science run. Class. Quantum Grav.*, 23:p653 – p660, 2006.

[14] D. G. Blair. *The detection of gravitational waves. Cambridge University Press*, 1991.

[15] W.M. Folkner *et al. Disturbance reduction system: testing technology for precision formation control. Proceedings of SPIE*, 4860, 2003.

[16] G. Heinzel, C. Braxmaier, R. Schilling, A. Rüdiger, D. Robertson, M. te Plate, V. Wand, K. Arai, U. Johann, and K. Danzmann. *Interferometry for the LISA technology package (LTP) aboard SMART-2. Class. Quantum Grav.*, 20:p153 – p161, 2003.

[17] J. Weber. *Detection and Generation of Gravitational Waves. Phys. Rev.*, 117, January 1960.

[18] G. Frossati. *Ultralow-temperature resonant gravitational wave detectors, present state and future prospects. Elsevier Science Ltd.*, December 2003.

[19] M. Bonaldi *et al. Dual acoustic gravitational wave detector. TCN CAE 2005*, 2005.

[20] F. Viviana. *Resonant-mass detectors: status and perspectives. Class. Quantum Grav.*, 21:p377 – p383, 2004.

[21] Karsten Danzmann and Albrecht Rüdiger. *LISA technology - concept, status, prospects. Class. Quantum Grav.*

[22] LIGO-M060056 v1: Advanced LIGO Reference Design. https://dcc.ligo.org/cgi-bin/private/docdb/retrievefile?docid=1507, March 2009.

[23] B Willke *et al. The GEO-HF project. Class. Quantum Grav.*, 23:p207, 2006.

[24] http://www.rzg.mpg.de/~ros/optocad/.

[25] D. Robertson, C. Killow, H. Ward, J. Hough, G. Heinzel, A. Garcia, V. Wand, U. Johann, and C. Braxmaier. *LTP interferometernoise sources and performance. Class. Quantum Grav.*, 22:p155 – p163, 2005.

[26] E. J. Elliffe, J. Bogenstahl, A. Deshpande, J. Hough, C. Killow, S. Reid, D. Robertson, S. Rowan, H. Ward, and G. Cagnoli. *Hydroxide-catalysis bonding for stable optical systems for space. Class. Quantum Grav.*, 22:p257 – p267, 2005.

[27] G. Heinzel, C. Braxmaier, M. Caldwell, K. Danzmann, F. Draaisma, A. Garcia, J. Hough, O. Jennrich, U. Johann, C. Killow, K. Middleton, M. te Plate, D. Robertson, A. Rüdiger, R. Schilling, F. Steier, V. Wand, and H. Ward. *Successful testing of the LISA Technology Package (LTP) interferometer engineering model. Class. Quantum Grav.*, 22:p149 – p154, 2005.

[28] U. Roth, M. Tröbs, T. Graf J. E. Balmer, and H. P. Weber. *Proton and gamma radiation tests on nonlinear crystals. Applied Optics*, 41, 2002.

[29] C. S. Dyer and D. R. Hopkinson. *Space radiation effects for future technologies and missions Report Reference QINETIQ/KI/SPACE/TR010690/1.1. New York IEEE*, 1997.

[30] LTP Project document:. S2-UGL-RS-3001 OBI Requirements Specification. July 2008.

[31] LTP Project document:. S2-AEI-TN-3016 Draft Requirements on LTP optical windows. 2004.

[32] F. Guzman Cervantes, G. Heinzel, A. F. Garcia Marin, V. Wand, F. Steier, O. Jennrich, , and K. Danzmann. *Real-time phase-front detector for heterodyne interferometers. Applied Optics*, 46, 2007.

[33] F. Guzman Cervantes. *Real - timespatially resolving phasemeter for LISA Pathfinder. Master's thesis, Albert Enstien Institute Hannover and University of Oldenburg*, 2004.

[34] A. F. Garcia Marin, J. Bogenstahl, F. Guzman Cervantes, F. Steier, J. Reiche, S. Skorupka, V. Wand, M. Nofrarias, J. Sanjuan, O. Jennrich, G. Heinzel, and K. Danzmann. *Interferometric characterization of the optical window for LISA and LISA Pathfinder*, 2006.

[35] E.Morrison, B.Meers, D.Robertson, and H. Ward. *Experimental demonstration of an automatic alignment system for optical interferometers. Appl. Op*, 33:p5037 – 5040.

[36] LTP Project document:. S2-UGL-TN-3009 Alignment Precision. November 2008.

[37] R. S. Afzal *et al. The Geoscience Laser Altimeter System (GLAS) Laser Transmitter. IEEE JOURNAL OF SELECTED TOPICS IN QUANTUM ELECTRONICS*, 13, 2007.

[38] J. Bogenstahl, W. Cunningham, E. D. Fitzsimons, J. Hough, C. J. Killow, M. Perreur-Lloyd, D. Robertson, S. Rowan, and H. Ward. *LTP fibre injector qualification and status. 7th LISA Symposium conference proceedings*, 2009.

[39] LTP Project document:. S2-UGL-PL-3010 Fibre Injector Qualification Plan. January 2009.

[40] LTP Project document:. S2-UGL-RP-3014 Test report of wax tests and pre-tests for vibration and shock qualification tests. November 2008.

[41] LTP Project document:. S2-UGL-TP-3017 Thermal tests of FIOS qualification model. January 2009.

[42] LTP Project document:. S2-UGL-TP-3016 Vibration and shock tests of FIOS qualification model. January 2009.

[43] LTP Project document:. S2-UGL-PL-3010 Fibre Injector Qualification Plan. January 2009.

[44] LTP Project document:. S2-UGL-RP-3018 Summary of FIOS QM vibration and shock tests. May 2009.

[45] LTP Project document:. S2-UGL-TN-3026 FIOS QM Vibration and Shock tests fixture design. October 2008.

[46] LTP Project document:. S2-UGL-TP-3015 Fibre injector optical performance tests. January 2009.

[47] LTP Project document:. S2-UGL-TP-3016 Vibration and shock tests of FIOS qualification model. January 2009.

[48] LTP Project document:. S2-UGL-TP-3017 Thermal tests of FIOS qualification model. January 2009.

[49] LTP Project document:. S2-UGL-TP-3018 Thermal vacuum cycle FIOS QM tests. May 2009.

[50] LTP Project document:. S2-UGL-TR-3016 Test Report of vibration and shock tests, June 2009.

[51] LTP Project document:. S2-UGL-TR-3017 Test report of thermal tests of FIOS qualification model. May 2009.

[52] LTP Project document:. S2-UGL-TR-3018 FIOS QM Optical performance test report. June 2009.

[53] LTP Project document:. S2-UGL-PR-3007 Hydroxide-catalysis bonding procedure for the LTP OBI PFM.

[54] LTP Project document:. S2-UGL-RP-3020 FIOS Proto-flight models OPT. August 2009.

[55] V. Greco *et al. Optical contact and van der Waals interactions: the role of the surface topography in determining the bonding strength of the thick glass plates. Journal of Optics A: Pure and Applied Optics*, 3, 2001.

[56] S. Reid, G. Cagnoli, E. Elliffe, J. Faller, J. Hough, I. Martin, and S. Rowan. *Influence of temperature and hydroxide concentration on the settling time of hydroxy-catalysis bonds. Physics Letters A*, 363:p341–p345, 2007.

[57] A. A. van Veggel, D. van den Ende, J. Bogenstahl, S. Rowan, W. Cunningham, G. H. M. Gubbels, and H.Nijmeijer. *Hydroxide catalysis bonding of silicon carbide. Journal of the European ceramic society*, 2008.

This thesis refers to project documents, which are available within the LTP community. These documents are highlighted in blue. Where possible scientific papers are referenced.

Selected publication list

2005

Elliffe, E. J.; Bogenstahl, Johanna; Deshpande, A.; Hough, J.; Killow, Christian J.; Reid, S.; Robertson, D.; Rowan, S.; Ward, H.; Cagnoli, G.
Hydroxide-catalysis bonding for stable optical systems for space
Classical and Quantum Gravity, 22(2205)

2006

V. Wand, J. Bogenstahl, C. Braxmaier, K. Danzmann, A. Garca, F. Guzmn, G. Heinzel, J. Hough, O. Jennrich, C. Killow, D. Robertson, Z. Sodnik, F. Steier, H. Ward
Noise sources in the LTP heterodyne interferometer
Class. Quantum Grav. 23 (2006) S159 - S167

G. Heinzel, J. Bogenstahl, C. Braxmaier, K. Danzmann, A. Garca, F. Guzmn, J. Hough, D. Hoyland, O. Jennrich, C. Killow, D. Robertson, Z. Sodnik, F. Steier, H. Ward, V. Wand
Interferometry for the LISA technology package LTP: an update
J. Phys.: Conf. Ser. 32 (2006) 132 - 136

A.F. Garca Marn, V. Wand, F. Steier, F. Guzmn Cervantes, J. Bogenstahl, O. Jennrich, G. Heinzel, K. Danzmann
On-orbit alignment and diagnostics for the LISA Technology Package
Class. Quantum Grav. 23 (2006) S133 - S140

C. J. Killow, J. Bogenstahl, F. Guzmn Cervantes, M. Perreur-Lloyd, D. I. Robertson, F. Steier, H. Ward
Construction of the LTP Optical Bench Interferometer
AIP Conf. Proc. 873 (2006) 297 - 303

Garcia Marin, Antonio Francisco; Bogenstahl, Johanna; Guzman Cervantes, Felipe; Steier, Frank; Reiche, Jens; Skorupka, Sascha; Wand, Vinzenz; Nofrarias, Miquel; Sanjuan, Josep; Jennrich, Oliver; Heinzel, Gerhard; Danzmann, Karsten
Interferometric characterization of the optical window for LISA Pathfinder and LISA
AIP Conference Proceedings, Vol.873, (2006)

2008

---

van Veggel, AA; van den Ende, D; Bogenstahl, J; Rowan, S; Cunningham, W; Gubbels, GHM; Nijmeijer, H
Hydroxide catalysis bonding of silicon carbide
Journal of the European ceramic society
Jan, 2008

2009

J Bogenstahl, L Cunningham, E D Fitzsimons, J Hough, C J Killow, M Perreur-Lloyd, D Robertson, S Rowan and H Ward
2009 7th LISA Symposium conference proceedings
LTP Fibre injector qualification and status

Roland Fleddermann, Frank Steier, Michael Trbs, Johanna Bogenstahl, Christian Killow, Gerhard Heinzel and Karsten Danzmann
2009 7th LISA Symposium conference procedeeings
Measurement of the non-reciprocal phase noise of a polarization maintaining single-mode optical fiber

E D Fitzsimons, J Bogenstahl, J Hough, C Killow, M Perreur-Lloyd, D I Robertson, S Rowan and H Ward
2009 7th LISA Symposium conference procedeeings
Initial interferometric pre-investigations for LISA

F Steier, R Fleddermann, J Bogenstahl, C Diekmann, G Heinzel and K Danzmann
Construction of the LISA back-side fibre link interferometer prototype
Class. Quantum Grav. 26 (2009) Number 17

LTP Project Documents

Johanna Bogenstahl, Harry Ward
S2-UGL-PL-3011 FIOS Construction Plan
September 2008

Johanna Bogenstahl, David Robertson
S2-UGL-PR-3010 Reflection and transmission of optical components
March 2008

Johanna Bogenstahl, Michael Perreur-Lloyd, David Robertson
S2-UGL-RP-3014 Test report of wax tests and pre-tests for vibration and shock qualification tests
November 2008

Johanna Bogenstahl, David Robertson
S2-UGL-RP-3015 FM AR/BS coating measurement
February 2009

Johanna Bogenstahl, Christian Killow, David Robertson
S2-UGL-RP-3017 Deformation of U-groove
April 2009

Johanna Bogenstahl, Michael Perreur-Lloyd, David Robertson
S2-UGL-RP-3018 Summary of FIOS QM vibration and shock tests
May 2009

Johanna Bogenstahl, Christian Killow
S2-UGL-RP-3020 FIOS Proto-flight models Optical performance test
August 2009

Johanna Bogenstahl, David Robertson
S2-UGL-TN-3030 Flight model optical component spectrophotmeter tests
February 2009

Johanna Bogenstahl, David Robertson
S2-UGL-TN-3033 Optical performance tests experimental set-up
May 2009

Johanna Bogenstahl, Christian Killow, David Robertson
S2-UGL-TN-3035 Adjustment of polished fibre end to lens distance
June 2009

Johanna Bogenstahl, Michael Perreur-Lloyd, David Robertson
S2-UGL-TP-3015 Fibre injector optical performance tests
January 2009

Johanna Bogenstahl, Michael Perreur-Lloyd, David Robertson
S2-UGL-TP-3016 Vibration and shock tests of FIOS qualifiaction model
January 2009

Johanna Bogenstahl, Michael Perreur-Lloyd, David Robertson
S2-UGL-TP-3017 Thermal tests of FIOS qualification model
January 2009

Johanna Bogenstahl, David Robertson
S2-UGL-TP-3018 Thermal-vacuum cycle FIOS QM tests
May 2009

Johanna Bogenstahl, David Robertson
S2-UGL-TR-3009 Baseplate surface measurement results
October 2007

Johanna Bogenstahl, David Robertson
S2-UGL-TR-3010 Optical components test report
September 2008

Johanna Bogenstahl, David Robertson

S2-UGL-TR-3017 Test report of thermal tests of FIOS qualification model

May 2008

Johanna Bogenstahl, David Robertson

S2-UGL-TR-3018 FIOS QM Optical performance test report

June 2009